Control-Structure Interaction Mitigation for NASA's Gateway

by

Daniel Christopher Reynolds

B.S. Astronautical Engineering
United States Air Force Academy, 2017

Submitted to the Department of Aeronautics and Astronautics
in partial fulfillment of the requirements for the degree of

Master of Science in Aeronautics and Astronautics

at the

MASSACHUSETTS INSTITUTE OF TECHNOLOGY

June 2019

Author . . . .
Department of Aeronautics and Astronautics
June 7, 2019

Certified by . . . .
Kerri Cahoy
Associate Professor of Aeronautics and Astronautics
Thesis Supervisor

Certified by . . . .
Ravi Gondhalekar
The Charles Stark Draper Laboratory, Inc.
Technical Supervisor

Accepted by . . . .
Sertac Karaman
Associate Professor of Aeronautics and Astronautics
Chair, Graduate Program Committee

Control-Structure Interaction Mitigation for NASA's Gateway

by

Daniel Christopher Reynolds

Submitted to the Department of Aeronautics and Astronautics
on June 7, 2019, in partial fulfillment of the
requirements for the degree of
Master of Science in Aeronautics and Astronautics

Abstract

The Gateway is an advanced National Aeronautics and Space Administration (NASA) concept for a multi-module space station to be placed in a near rectilinear halo orbit around the Moon sometime in the next decade. The first module of the Gateway is known as the Power and Propulsion Element (PPE), and is set to launch in 2022. As the station's first module, the PPE will be responsible for providing the Gateway with "electrical power, communications, attitude control, orbit maintenance, and the ability to change orbits" [16]. Control of the Gateway represents a complicated and unique control problem due to the spacecraft's status as a large, multi-modular spacecraft; it will have multiple dominant structural modes from its comprising elements: modules, external payloads, solar arrays, a robotic arm, visiting spacecraft, etc [31]. Other spacecraft in this class include the Space Shuttle, the Mir space station, and the International Space Station (ISS). The field that pertains to the "coupling" of control inputs and the resultant structural dynamics is known as "Control-Structure Interaction (CSI)" [22], and developing CSI mitigation strategies from induced propulsive and non-propulsive actuation has become an important objective for control systems engineers working on large, flexible space structures today. The current standard for CSI management is evident in the recently retired Space Shuttle's flight control system: a phase-plane attitude control loop with notch filters on the feedback channel that enabled docked operations with the Mir space station and the ISS. However, when unconstrained by the Shuttle's architecture and freed to investigate more modernized and adaptable control methods, additional options arise as feasible candidates for Gateway CSI mitigation. For example, a Linear Quadratic Regulator (LQR) provides the basis for individual state vector cost weighting, so that steps can be taken to more directly target the vibrations resulting from multiple structural elements. A Frequency Weighted Linear Quadratic Regulator (FWLQR) extends the functionality of a LQR by enabling the direct penalization of specified frequencies in order to shape the system's dynamic responses. The Model Predictive Control (MPC) optimization-based approach supplements the frequency-weighted LQR by adding input and output constraint-handling capabilities. Out of all of the CSI mitigation strategies evaluated, MPC appears to be the optimum candidate for large, flexible space structure CSI mitigation for its adaptability, flexibility, and relative performance.

Kerri Cahoy
Associate Professor of Aeronautics and Astronautics
Thesis Supervisor

Ravi Gondhalekar
The Charles Stark Draper Laboratory, Inc.
Technical Supervisor

Acknowledgments

"Kahuna Nui Hale Kealohalani Makua"

It will forever be impossible to convey the immense gratitude and love that I feel for the countless family, friends, colleagues, mentors, and supporting organizations that have been so instrumental in allowing me to become the person that I am today, and consequently, to produce this thesis. What follows is a dedication to all those who made this possible. From the bottom of my heart, I thank you.

First and foremost, I want to provide my immeasurable thanks to the United States Air Force, the Massachusetts Institute of Technology, the Charles Stark Draper Laboratory, the United States Air Force Academy, and the Draper Fellow Program for many of the most profound opportunities in my life thus far. Thank you for investing so much time and energy into making me into a better person. You took a chance on me when you didn't have to, and for that I am extraordinarily thankful. Through you, I have learned valuable lessons, developed incredible relationships, and have grown immensely.

Next, I wanted to thank all of the mentors at Draper that provided me with their support over the past two years. To the Draper Fellow program managers Dr. Sheila Hemami and Mrs. Martha Porter, thank you so much for accepting me into this incredible program and organization, and for being so supportive throughout my two year-long tenure. To my division leader Dr. Diane Mills and my group leader Dr. Louis Breger, thank you for taking me into the Guidance and Control Group, and for allowing me to work and grow side-by-side with some of the most dedicated people that I have ever met. To Mr. Michael Martin, Mr. Sagar Bhatt, Dr. Phil Hattis, Dr. Neil Appleby, Dr. Leena Singh and Dr. Jiann-Woei Jang: thank you for the crucial feedback that you offered me in the early stages of my research; it most certainly helped to shape the direction that I ultimately took. Finally, to Mrs. Michelle Pelersi, Dr. Seamus Tuohy, and other members of the Draper education office who supported this project at a high-level: thank you for giving me the freedom to be creative and for the opportunity to pursue a research topic that I was truly passionate about.

To my advisor Dr. Kerri Cahoy, thank you so much for your consistent support over the past few years. I will always remember you for your limitless enthusiasm and for your altruistic desire to help your students achieve success. You inspire me with your work ethic and your passion for teaching. And of course, to Dr. Ravi Gondhalekar, my technical supervisor at Draper: from evening philosophical discussions to inspiring stories about flight, thank you so much for being approachable, supportive, and encouraging throughout my entire tenure at Draper. Your technical insight and your kind, patient nature has enabled a strong backbone for this thesis. It is needless to say that you have greatly enabled my success at MIT.

To my family: mom and dad, you both are and have been two of my best friends. It's so difficult to convey my love and appreciation for you both in a few short sentences, but I want to thank you so much for always being there for me, no matter what. Benedikt, it's been a blessing having you so close by. Thank you for some of the most enlightening conversations that I've ever had, and for our transformation from siblings to true friends. You inspire me to continue to explore my creative side! Johnny, you've always been one of my biggest role models. Thanks for always being a voice of reason, and for the constant reminders to always learn, grow, and focus on those beautiful traits of love for one another and for yourself. To my sister Rachel: I'm so grateful for the strong bond that we share. Thank you for being someone that I could talk to for just about anything and everything, and for your dual role as a loving sister and a strong mentor.

Ultimately, this thesis is dedicated to all individuals: past, present, and future, who have, continue to, and will in times to come give their hearts, minds, and spirits to the exploration of space. Thank you for your sacrifice, love, passion, and relentless pursuit of the globally unifying dream to extend our human hands outwards into the universe. You are my inspiration.

Daniel C. Reynolds, 2d Lt, USAF

Contents

Acronyms

BAA	Broad Agency Announcement
CSA	Canadian Space Agency
CMG	Control Moment Gyro
CONOPS	Concept of Operations
CR3BP	Circular Restricted Three Body Problem
CSI	Control-Structure Interaction
CSM	Command and Service Module
DAP	Digital Autopilot
DFT	Discrete Fourier Transform
DRO	Distant Retrograde Orbit
ESA	European Space Agency
EVA	Extravehicular Activity
FCS	Flight Control System
FWLQR	Frequency Weighted Linear Quadratic Regulator
GNC	Guidance, Navigation, and Control
IMU	Inertial Measurement Unit

ISS	International Space Station
IUS	Inertial Upper Stage
JAXA	Japan Aerospace Exploration Agency
JPL	Jet Propulsion Laboratory
LLO	Low Lunar Orbit
LM	Lunar Module
LQG	Linear-Quadratic-Gaussian
LQR	Linear Quadratic Regulator
LTI	Linear Time-Invariant
MIMO	Multiple Input Multiple Output
MIT	Massachusetts Institute of Technology
MPC	Model Predictive Control
MPCV	Multi-Purpose Crew Vehicle
NASA	National Aeronautics and Space Administration
NRHO	Near Rectilinear Halo Orbit
OMS	Orbital Maneuvering System
PDP	Plasma Diagnostic Package
PID	Proportional-Integral-Derivative
PPE	Power and Propulsion Element
PRCS	Primary Reaction Control System
RCS	Reaction Control System

RFI	Request for Information
RMS	Remote Manipulator System
ROSA	Roll-Up Solar Array
RS	Russian Segment
RTLS	Return to Launch Site
RW	Reaction Wheel
SEP	Solar Electric Propulsion
SISO	Single Input Single Output
SLS	Space Launch System
SMA	Safety and Mission Assurance
TDRS-1	Tracking and Data Relay Satellite-1
TLI	Trans-Lunar Injection
VRCS	Vernier Reaction Control System

Nomenclature

$\dot{\theta}_P$	The PPE's angular velocity relative to its point of origin in degrees/second
$\dot{\theta}_R$	The solar array's angular velocity relative to its point of origin in degrees/second
$\dot{x}_P$	The PPE's velocity relative to its point of origin in m/s
$\dot{x}_R$	The solar array's velocity relative to its point of origin in m/s
γ	Interval in which the finite difference is calculated over for u_D
κ	The value of the spring coefficient in N/m
ν	The value of the viscous damping coefficient in N /(m/s)
ω^B_{error}	Error rate as represented on the phase plane
τ	The torque matrix in $\mathrm{N} \cdot \mathrm{m}$
θ^B_{error}	Error as represented on the phase plane
θ_P	The angular displacement of the PPE from its point of origin in degrees
θ_R	The angular displacement of the solar array from its point of origin in degrees
A	The *state transition matrix*
B	The *input distribution matrix*
b	The extended length of the rectangular solar array wing flush with the y-axis of rotation in m

C	The *output matrix* of the specific model
D	The *feedforward matrix*
$e(k)$	Error between commanded output and current input
f	Frequency in Hz
f^+	Reaction Control System (RCS) jet “on” notation on the phase plane
f^-	RCS jet “off” notation on the phase plane
I_x	The mass moment of inertia about the x-axis, in $\mathrm{kg \cdot m^2}$
I_z	The mass moment of inertia about the z-axis, in $\mathrm{kg \cdot m^2}$
J	Cost function for LQR, FWLQR, and MPC control methodologies
J_P	The mass moment of inertia of the PPE in $\mathrm{kg \cdot m^2}$
J_R	The mass moment of inertia of the solar array in $\mathrm{kg \cdot m^2}$
K_D	Scalar controller gain for PID derivative control action
K_{FWLQR}	FWLQR gain matrix
K_I	Scalar controller gain for PID integral control action
K_{LQR}	LQR gain matrix
K_P	Scalar controller gain for PID proportional control action
m	The number of outputs in the output vector
m_P	The mass of the PPE in kg
m_R	The mass of the solar array in kg
N	Prediction horizon
n	The number of states in the state vector

P	Solution of the algebraic Riccati equation
p	The number of inputs in the input vector
Q	State vector cost function weighting variable for LQR, FWLQR, and MPC control methodologies
Q_{Output}	Output vector cost function weighting variable for LQR, FWLQR, and MPC control methodologies
R	Input vector cost function weighting variable for LQR, FWLQR, and MPC control methodologies
S	Weighting vector on output constraints
T	The thrust matrix in N
$u(k)$	The discrete-time *input vector*
$u(t)$	The continuous-time *input vector*
u_D	Derivative control action element for the PID controller
u_I	Integral control action element for the PID controller
u_P	Proportional control action element for the PID controller
V	Terminal cost; weighting variable unique to finite-horizon MPC
$x(k)$	The discrete-time *state vector*
$x(t)$	The continuous-time *state vector*
x_P	The displacement of the PPE from its point of origin in m
x_R	The displacement of the solar array from its point of origin in m
$y(k)$	The discrete-time *output vector*
$y(t)$	The continuous-time *output vector*

z_k	Difference between minimum and maximum output constraints of the controller output as a function of time

List of Figures

Chapter 1

Introduction

1.1 Motivation

On 23 June 2011, a Russian Progress cargo vehicle (NASA identifier: 43P) was on approach to dock with the ISS [32]. To prepare for the docking, the ISS was conducting a 180° slewing maneuver using thrusters onboard its Zvesda service module and an already docked Progress cargo vehicle. During the slewing maneuver, the control system of the ISS's Russian Segment (RS) falsely detected that two of the thrusters charged with yaw actuation onboard the Zvesda service module (Manifold 2 thrusters #12 and #13 visualized in Figure 3 of [32]) had failed. The control system of the ISS's RS then reverted to alternate thrusters (Manifold 1 thrusters #18 and #19 visualized in Figure 3 of [32]) in an effort to complete the slewing maneuver.

The failure of the control logic resulted in unintentional thruster firings that yielded a 10-minute-long period of high acceleration. This event was considered by NASA and the Russian space agency to be one of the "most severe" high acceleration events in the ISS's operational history [32]. Significantly high loads were noticed in multiple ISS structural elements that were, at times, 25% higher than those experienced during pre-flight analyses.

Although no structural damage was incurred, the event prompted an extraordinarily valuable expansion of risk awareness for the ISS program [32]. Both NASA and Russian space officials "realized that the ISS had been flying at risk of catastrophic structural loads caused by thruster firings, and those loads had the potential to be much higher than those experienced" [32] during the 23 June 2011 event. One of the concluding statements in the paper describing the event was the realization that the ISS had experienced a severe "control-structure interaction" problem [32].

1.2 Defining "Control-Structure Interaction" (CSI)

The discipline of CSI is defined by NASA as the "detrimental closed-loop coupling between structural modes and a feedback control system" [65]. Simply defined, CSI is the coupling between the resultant dynamic structural responses of a physical system to control inputs. The field of CSI emerges from an intersection of control systems engineering and structural engineering. From ground-based systems such as automobiles [61] to underwater vehicle-manipulator systems [20], managing the dynamic responses of physical systems as a result of control inputs is an important discipline that a control systems engineer must consider to ensure system performance and survivability.

In the realm of human spaceflight, the 23 June 2011 event is considered to be one of the most severe CSI issues pertaining to excessive structural loads generated by unintentional thruster firings. To the author, this event highlights the complexities of CSI management and mitigation for large space structures like the ISS. The ISS is unique when compared to other spacecraft (both current and historical) for its sheer size and mass. The ISS is comprised of many structural elements, including: 16 modules, eight solar arrays covering an area of approximately 2,500 m^2, truss segments, pressurized mating adapters, and more [1] [13] [4] [13]. The image available at [13] depicts an exploded view of the ISS to help the reader in visualizing the structural complexity of the 357 foot (end-to-end) space station [12].

Large and flexible space structures are sensitive to excitation, due to the existence of various bending modes and resonant frequencies that are inherent to the spacecraft's structural elements. The resultant motion stemming from control actions can excite these modes of vibration, which can lead to instabilities and can induce loads, which is what occurred in the 23 June 2011 event. The same report that described the ISS event [32] included a snapshot of some of the ISS's sensitive frequencies from 0 Hz to 0.033 Hz, and some of the sources of these frequency spikes [32]. This snapshot is provided in [32] as Figure #26.

To avoid exciting the various resonant frequencies associated with the structural elements of spacecraft, control systems engineers need to develop methods and logic within control systems to avoid excitations and significant structural stresses. During NASA's Gemini space flight program of the 1960s, engineers used a notch filter to remove troublesome portions of the spectrum on the sensor feedback channels, thereby preventing the controller from acting upon those frequencies, and thus mitigating load-inducing activity during docked operations between the Gemini spacecraft and the uncrewed Agena target vehicle [65]. The first bending mode of the docked spacecraft was at 5 Hz, so a notch filter was used to sustain a gain margin of 6 dB at that frequency [65], thus mitigating potentially destabilizing spectral content at that frequency. During the Apollo-era, similar methods were used when the Apollo Command and Service Module (CSM) was docked with the Lunar Module (LM) to avoid the excitation of certain frequencies [69]. The Space Shuttle also employed a notch filter-based approach to remove the pathological frequencies from the feedback signal that could cause the control system to excite frequencies of concern (e.g., the frequencies of the dominant structural modes) during docked operations with the Mir space station, in addition to assembly and docked operations with the ISS. More details on the Space Shuttle's CSI mitigation strategy are presented in Section 4.1 of this thesis.

CSI, simply defined, is the coupling between the resultant dynamic structural responses of a physical system to control inputs. For spacecraft, this can include both intended inputs such as the various means of propulsion and attitude control, and external inputs such as solar radiation pressure, outgassing, and forces/torques incurred through docking with other spacecraft. As the 23 June 2011 incident emphasized, significant care must be placed towards the development of an effective CSI mitigation strategy that can not only manage the intended and external inputs to a system, but one that can also withstand worst-case scenarios. This is especially important for large, flexible spacecraft with multiple modes of vibration like the ISS. Developing a CSI mitigation strategy that can mitigate potentially destabilizing vibrations is crucial for the mission success of any future spacecraft. NASA's Gateway is one such spacecraft.

In Chapter 1 of this thesis, the Gateway is introduced from both a programmatic (Section 1.3) and a technical (Sections 1.3.1 and 1.3.2) point of view. The programmatic review recaps the state of the Gateway project at the time of the writing of this thesis. A technical review is also presented, which consists of two primary components; the first component is a review of the high-level requirements published by NASA in the summer of 2018 in regards to the Gateway's first module, the PPE. The second component is a review of the operational orbit that the PPE will presumably be deployed into, and the family of orbits that it will potentially operate in (while simultaneously growing in size to represent the full Gateway stack) (Section 1.3.2). A primary objective of Chapter 1, beyond introducing the Gateway as a program, is to establish its nominal operating parameters. By presenting the PPE's requirements and information about its insertion orbit, the reader can gain an insight into various ΔV, energy, and maneuvering requirements that the Gateway will be expected or required to subscribe to. Additionally, by understanding the nominal operating parameters of the PPE, two case studies representative of the Gateway's planned orbital maneuvers can be crafted to test a pre-selected array of candidate CSI mitigation strategies. The cases of orbital translations and attitude control maneuvers (i.e., orbital station-keeping and transitions between various orbits) can be crafted to test a pre-selected array of candidate CSI mitigation strategies, which is the subject of Chapter 2.

Chapter 2 applies the programmatic and technical data presented in Chapter 1 to develop the specific case studies that detail the maneuvers to be performed by each CSI mitigation strategy. First, various assumptions are made in regards to the simulation duration of each of the case studies (Section 2.1), with a follow-on discussion on the actuation limitations per CSI mitigation strategy (Section 2.2). An introduction is given to the "Turn-to-Burn" strategy that will characterize the majority of the Gateway's maneuvers throughout its lifetime in Section 2.3. The "Turn-to-Burn" strategy is divided into three distinct maneuvers: an initial rotation to the burn attitude, the burn itself, and a follow-on rotation to either the original or a new spacecraft attitude. Case Study #1 is crafted to evaluate the PPE's dynamics, with an extended solar array, under a 1.5-meter translational burn in one axis (Section 2.4), and Case Study #2 is crafted to model an 180° rotation about one axis (Section 2.5). The case studies establish the maneuvers that each CSI mitigation strategy will be evaluated against, and make up one part of the simulation space. The second part refers to the linear LTI models that will define the structural dynamics of the PPE and its solar array for both the translational and rotational models, and is presented in 3.

Chapter 3 introduces the translational (Section 3.1.1) and rotational (Section 3.1.2) models that will define the Gateway model used in the simulation space. The translational and rotational models are representative of the PPE with one extended, large, flexible solar array. Section 3.2 provides a discussion characterizing the maximum and minimum thrust and torque values that will be used as control inputs in the translational and rotational models.

Chapter 4 introduces each of the five CSI mitigation strategies that are tested in the simulation environment against each of the three case studies. These strategies, along with a brief description, are provided in the following enumerated list:

1. **Phase Plane**; **Section 4.1**: Phase plane controllers operate with respect to a two-dimensional Cartesian coordinate grid, with error presented on the horizontal axis and error rate presented on the vertical axis. The error and error rates are calculated from differences between commanded attitudes and actual attitudes. Control engineers design switching lines on this grid which, when error vs. error rate boundary lines are exceeded, trigger the "on" condition of binary "on-off," or "bang-bang" thrusters to drive the error and error rate back to within acceptable margins. This method was used for the Space Shuttle's on-orbit Digital Autopilot (DAP).

2. **PID Control**; **Section 4.2**: PID is a classical control method that is cited as being the most common control method used for control applications today [75]. The control action is composed of three control components: a proportional component that considers control action based upon the current error (i.e., the difference between the commanded attitude and the current attitude), an integral component that considers previous error, and a derivative component that considers future error [74].

3. **LQR**; **Section 4.3**: The LQR is an optimal controller that, given a set of user-specified weighted parameters that balance weights on system states and inputs, incorporates a cost function to ultimately compute a state-feedback gain for computing a control input that minimizes said cost function [30] [45].

4. **FWLQR**; **Section 4.4**: The FWLQR control method builds off of the foundations provided in LQR theory, by supplementing the base capabilities of LQR with the ability to penalize frequencies of interest.

5. **MPC**; **Section 4.5**: MPC is an effective strategy for constrained control problems. One can accommodate known constraints on control inputs. Furthermore, one can impose desired constraints on the system's states and/or outputs.

Chapter 5 implements these control methodologies as representative translation and attitude controllers. Section 5.1 evaluates the performance of each CSI mitigation strategy for Case Study #1, and Section 5.2 evaluates their performance for Case Study #2. Each CSI mitigation strategy is evaluated for its ability to accomplish the primary control objective of completing the translation or attitude change maneuver, and the secondary control objective of mitigating potentially destabilizing oscillations.

Chapter 6 concludes with a brief recap of the thesis's contribution in Section 6.1. Section 6.2 provides a discussion of the simulation results procured in 5, and provides the author's recommendation on the highest-performing control strategy in the context of the simulations performed. Section 6.3 concludes the thesis with a few topic areas that can be further developed.

1.3 Introduction to NASA’s Gateway

The Gateway is an advanced NASA concept for a multi-module space station to be placed in lunar orbit in the early 2020s [42]. As humanity’s first long-term crewed/uncrewed presence in lunar orbit, the Gateway draws its appeal from being able to serve as a multipurpose lunar outpost in cislunar space: its planned positioning in lunar orbit is expected to enable routine deployments to a lunar research station, and serves as a crucial element in NASA’s plan to expand humanity’s presence to Mars [42].

The concept for a lunar space station has existed for some time, but the 2019 NASA fiscal year budget request was the first to specifically allocate funding for the Gateway project, recommending \$504.2 million [9]. The final budget approved by Congress in February 2019 was the first to allocate funding specifically for the Gateway, but had decreased this value to \$450 million [24] [26]. In comments following the release of the budget request, then acting NASA administrator Robert Lightfoot cited the relationship of the requested Gateway funding with that of the current political administration’s efforts to expand humanity’s presence to the Moon, Mars, and to other destinations beyond Earth [56]. These efforts, as made evident in a White House memorandum issued a few months prior, amended the previous National Space Policy of the United States to putting the United States in a position to “lead the return of humans to the Moon for long-term exploration and utilization, followed by human missions to Mars and other destinations” [40].

In response to this directive, NASA released a Request for Information (RFI) specific to the first Gateway module, the PPE in July 2017 [5] [7]. The purpose of the PPE is to provide a variety of fundamental capabilities to the rest of the multi-module Gateway stack. The following bulleted list was taken verbatim from [11], and describes these capabilities:

- “Obtain data to understand the health and performance of the system” [11]
- “Obtain data to support future operations and sustaining engineering including anomaly troubleshooting data” [11]

- “Provide power to the Gateway” [11]
- “Provide transportation for the Gateway between cislunar orbits and perform any needed orbital maintenance” [11]
- “Provide attitude control for the Gateway in multiple configurations with and without visiting vehicles such as Orion” [11]
- “Provide Gateway communications with Earth, visiting vehicles, and the lunar surface, and act as a relay with Earth for visiting vehicles, in support of extravehicular activity (EVA) and lunar surface operations.” [11]
- “Support utilization experiments and technology demonstrations provided by NASA, international, or commercial partners” [11]

The July 2017 RFI’s purpose was therefore to explore “the possibility of a cost effective development effort” for the PPE, by inviting companies to provide descriptions of ability, conceptual schedules, and summaries of technical development approaches specific to the construction of the PPE [5]. Within the RFI, 16 fundamental technical capabilities were listed to guide these companies in their attempts to secure NASA’s support to conduct concept studies that would lead to various PPE concepts [5]. These fundamental design reference capabilities would come to form the foundation of an initial rendition of the PPE’s higher level requirements, which were released in a draft Broad Agency Announcement (BAA) nearly one year later (June 2018) [53]. In November 2017, NASA announced that the Boeing Company, Lockheed Martin, Orbital ATK Incorporated, the Sierra Nevada Corporation, and Space Systems/Loral were selected to conduct studies into a PPE concept design [37].

The PPE BAA can best be defined as “a full and open competition soliciting proposals from United States Industry that could lead to potentially one or more technology demonstration contract awards for an industry/NASA partnership for the development and spaceflight demonstration of a PPE” [11]. As previously mentioned, the contents of the BAA include high level requirements that industry could use to begin their concept design process, but it also includes additional elements such as a notional summary schedule (with a predicted PPE launch in 2022), government furnished equipment information, and additional reference materials that potential industrial partners could use [15].

In September 2018, NASA released an updated version of the BAA as a formal solicitation for research and development contracts that would help in enabling the development of a PPE, with a proposal due date of November 2018 [11]. NASA released the formal BAA in September 2018, and is currently in the process of evaluating PPE industry proposals. In February 2019, NASA released a memorandum stating that the procurement process was still ongoing [58]. NASA, in its September 2018 BAA, stated that "offeror[s] shall propose a schedule with a launch date [of] no later than September 2022 with a demonstration to last no longer than one year in duration to be completed no later than September 2023" [11], although in its February 2019 update the no-later-than launch date had slipped to 31 December 2022. [58]

In September 2018, NASA released a layout of what the Gateway could look like when fully assembled [31]. The presentation in which this layout was provided also includes descriptions of each of the elements briefed by NASA in the September 2018 presentation [31]. These descriptions and their corresponding elements are presented in the following enumerated list, and were taken verbatim from [31].

1. **Power and Propulsion Element (PPE):** "Power, communications, attitude control, and orbit control and transfer capabilities for the Gateway" [31].
2. **ESPIRIT:** "Science airlock, additional propellant storage with refueling, and advanced lunar telecommunications capabilities" [31].
3. **U.S. Utilization Module:** "Small pressurized volume for additional habitation capability" [31].
4. **Robotic Arm:** "Mechanical arm to berth and inspect vehicles, install science payloads" [31].
5. **Habitation Module:** "Pressurized volumes with environmental control and life support, fire detection and suppression, water storage and distribution" [31].

6. **Logistics and Utilization:** “Cargo deliveries of consumables and equipment. Modules may double as additional utilization volume” [31].
7. **Roll-Up Solar Arrays (ROSAs):** 300 kW class solar arrays.
8. **Sample Return Vehicle:** “A robotic vehicle capable of delivering small samples or payloads from the lunar surface to the Gateway” [31].
9. **Airlock:** “Enables spacewalks, potential to accommodate docking elements” [31].
10. **Orion Multi-Purpose Crew Vehicle (MPCV):** “U.S. crew module with ESA service module that will take humans farther into deep space than ever before” [31].

On 5 March 2019, NASA published a press release which included an illustration highlighting the international collaboration that will go behind the development of the Gateway [67]. It broke down the international stakeholders that will participate in the Gateway’s development per module [67]. According to this information, NASA, the European Space Agency (ESA), the Japan Aerospace Exploration Agency (JAXA), the Canadian Space Agency (CSA), and the Russian State Corporation for Space Activities (ROSCOSMOS) will be stakeholders in the design of the Gateway stack [67].

1.3.1 PPE Requirements

A list of high level requirements accompanied the BAA in June 2018 that were specific to the PPE [53]. These requirements were published to provide potential industry partners with a high-level understanding of both the purpose and capabilities of the PPE, as desired by NASA. Concurrently, these requirements and the rest of the BAA serve as one of the best public resources on extrapolating information necessary for PPE model and simulation development. Additionally, other elements of publicly releasable information, such as the orbit of the Gateway, allow for the generation of additional assumptions that will help in shaping the simulation environment. The following list is a summary of the most applicable PPE requirements with respect to the development of a CSI mitigation strategy, and includes some verbatim information taken from the requirements document [53]. Listed alongside these requirements are the official identifiers of requirements that influenced the requirement synopses:

1. Guidance, Navigation, and Control (GNC)
    (a) Three-Axis Attitude Control & Translational Maneuver Authority [53] - **NU-PPE-1415**; **NU-PPE-1591**; **NU-PPE-1780**; **NU-PPE-1506**
        i. The PPE shall have two onboard propulsive mechanisms available in which to perform three-axis attitude control and to perform translational maneuvers: a RCS monomethylhydrazine-based capability and a 300 kW-class xenon-based Solar Electric Propulsion (SEP) capability. Additionally, the PPE will have a non-propulsive three-axis attitude control capability in the form of Control Moment Gyros (CMGs) and/or Reaction Wheels (RWs).
    (b) Free Drift: Zero Forces, Torques [53] - **NU-PPE-1843**; **NU-PPE-1482**
        i. The PPE shall be capable of flying in a static free drift mode. This is relevant for docking procedures, as the Gateway will be the target vehicle for all visiting vehicles and incoming modules. These requirements also highlight the necessity of the flight control system to bring the Gateway to a static and stable state after conducting translational or rotational maneuvers.
    (c) PPE Autonomous Operations Demonstration [53] - **NU-PPE-1796**; **NU-PPE-1893**
        i. The PPE shall be able to operate autonomously, including with SEP system burns during cislunar orbital transfers, for at least three weeks. Autonomous operations, as defined by NASA in the context of the PPE, includes having a system capable of completing "all PPE functions... needed to support the Gateway Mission... without ground controllers in the loop" [53]. This three-week requirement is also embedded in the fact that the Gateway is to be uncrewed for extended

periods of time, and may require remote and/or autonomous operations.

   (d) Maintenance of Near Rectilinear Halo Orbit (NRHO) [53] - **NU-PPE-1910**; **NU-PPE-1911**; **NU-PPE-1923**

      i. The PPE shall be able to perform orbital maintenance maneuvers with both the SEP and the RCS systems. Orbital maintenance maneuvers are burns required to keep the Gateway in a designated orbit. The Gateway is predicted to require a ΔV of less than 10 m/s per year in regard to orbital maintenance in its NRHO deployment.

   (e) Orbital Transfers [53] - **NU-PPE-1898**; **NU-PPE-1914**; **NU-PPE-2237**; **NU-PPE-1897**

      i. The Gateway shall be capable of performing cislunar orbital transfers with the SEP system. This includes the insertion into a NRHO at the beginning of the PPE/Gateway's mission with the SEP system.

2. Crew

   (a) Crew Vibration Exposure Limits [53] - **NU-PPE-1497**

      i. NASA maintains standards on human factors, habitability, and environmental health in a document known as NASA-STD-3001 Volume 2 [3]. This document provides insight into a variety of vibration limitations on crew members during multiple stages of flight (e.g., preflight, sleep periods, maximum exposure guidelines in a 10 minutes time span, etc.) that can be used to influence the development of a CSI mitigation strategy. For example, it is noted that the "maximum frequency-weighted acceleration" that the crew may experience between "0.5 and 80 Hz" in a one-minute-long period is "5.9 m/s^2 RMS (0.6 g RMS)" [3]. Having a capability to manage vibrations related to the physiological requirements of the crew is important.

3. Mechanical

   (a) Flight System Mass [53] - **NU-PPE-1702**

      i. The "PPE... shall not exceed a wet mass of 8000 kg after completion of the spaceflight demonstration" [53].

   (b) Exclusion Zones [53] - **NU-PPE-1710**

      i. The Gateway shall be able to actively avoid various "keep-out zones" during operations within its lifetime. A "keep-out zone" is defined as an area that the Gateway will not be able to perform either three-axis attitude control or translational burns in. This includes exclusion areas during crewed Extravehicular Activities (EVAs), operations from a Remote Manipulator System (RMS), visiting vehicles, etc.

   (c) In-Space Structural Monitoring - **NU-PPE-1873**

      i. The PPE "shall provide telemetry to monitor and characterize [the] structural dynamic response of the PPE to in-space load events," such as docking operations, control inputs, and crew activities [53]. Additionally, the requirements state that "it will be important to measure the overall dynamic response to these events for the lifetime of the PPE in order to validate Gateway dynamic models, assess structural health and adjust operations if needed" [53]. Having the ability to measure the overall dynamic response of a system to load-inducing events and to compensate for them is a crucial component that the Gateway's control system must have.

4. Safety and Mission Assurance (SMA)

   (a) Autonomous Hazard Control [53] - **NU-PPE-2241**

      i. "The PPE... shall provide autonomous control of catastrophic hazards" [53].

   (b) Respond to Loss of Function - Autonomous Safing [53] - **NU-PPE-2268**

      i. The PPE shall be capable of autonomously entering into a safe mode and remaining there for three weeks, in regards to preventing any catastrophic events to the Gateway or the crew within.

The requirement categories, as summarized above, contain a summary of those requirements that are directly relevant to the design of a CSI mitigation strategy. The control architecture onboard the Gateway should not only be able to accommodate three-axis attitude control and to have translational maneuver authority, but it should also be able to perform in an autonomous capacity, and should be well-equipped to manage a variety of hazards. Additionally, the control architecture of the Gateway should be developed in consideration to a variety of "exclusion zones," as described in requirement summary 3.b. above [53]. As the Gateway grows and expands, it's control architecture should be able to consider constraints on controller outputs (e.g., stack displacement from origin, stack rotation, relative displacement of the primary stack with respect to the station's solar arrays, etc.). Finally, the specific mentioning of the management of vibrations that the crew would be exposed to during flight provides an additional motivation for an effective CSI mitigation strategy. These considerations and takeaways are important, as they contribute to the formulation of various case studies in which to test potential CSI mitigation strategies against in the simulation environment. Ultimately, understanding the programmatic and technical details of the Gateway and the PPE are important, as they are a primary driver behind the motivation, design and choice of a control methodology for CSI mitigation.

1.3.2 Gateway Deployment and Operational Orbit

It is important to understand the orbit that the PPE will be deployed into, and concurrently, the family of the orbits that the Gateway will operate in. Orbits carry with them certain energy requirements associated with initial orbit insertion, station-keeping, and transitions to other orbits. Understanding the orbit of the Gateway is an important step in the creation of the two nominal case studies that the CSI mitigation strategies will be evaluated against.

The PPE will be deployed into a NRHO about the Moon [53]. The NRHO orbit family can be conceptually defined as a family of orbits "with large amplitudes over either the north or south pole with shorter periods that pass closely to the opposite pole" [68]. The NRHO family of orbits exists because of the L1 and L2 Lagrange points; equilibrium points in space that are solutions to the Circular Restricted Three Body Problem (CR3BP) [29] [34] [25]. The CR3BP dynamical model considers the motion of a massless point (the spacecraft), "under the gravitational influence of the Earth and the Moon" [29]. Solving the CR3BP yields five points of equilibrium: three of which (the unstable three) are located along the Earth-Moon "line" (two of which are the L1 and L2 points, which are visualized in Figure 1 of [29]).

Numerous studies have been made into both the characteristics and advantages of the NRHO family as operational orbits for lunar space stations [68] [71] [29] [25] [51]. One pertinent consideration to the selection of the NRHO family is the ability for crews to access it from Earth given time and fuel constraints. At the time of this thesis' composition, the most reasonable candidate for crew delivery to a space station in a NRHO is the Orion MPCV, which, after being launched from Earth and inserted into a Trans-Lunar Injection (TLI) orbit, will have enough remaining fuel to achieve a total ΔV of 1250 m/s [68]. The Orion MPCV will be able to support 4 crew members for 21 days at a time [68]. Although ΔV requirements will vary slightly depending on launch dates and mission durations (e.g., if the Orion MPCV could be equipped for longer duration missions), a NRHO was found to be suitable and well within the ΔV and transit time requirements [68]. For a 21-day mission, for example, a crew launching in February 2021 would require the ability to produce a total of 840 m/s of ΔV to ensure a "stay time" of 10.9 days in a NRHO (where "stay time" refers to the amount of time that the crew could remain in a NRHO given the 21-day mission length) [68].

An important mission objective for the Gateway is to enable lunar surface access, so the selected orbit should facilitate this objective. For uncrewed missions from the Gateway, a lander would only require the fuel necessary to produce a ΔV on the order of tens of meters per second to enter into a Low Lunar Orbit (LLO). This value only includes the necessary ΔV to get from the NRHO to the LLO, and does not include the ΔV required to transit from the LLO to the lunar surface. The transfer to the

LLO from the NRHO would, however, require a transfer time of several months [31]. The Gateway could possibly host at least one uncrewed sample return vehicle, which could make use of this minimal fuel benefit [31]. Additionally, there are a variety of other uncrewed spacecraft that could deploy from the Gateway and take advantage of this low ΔV requirement. For crewed spacecraft, the NRHO is the second most preferred orbit to enter into a polar LLO from prior to beginning a powered descent, relative to five other candidate orbits analyzed in [68]. For landings at a polar-based location on the lunar surface, a ΔV of approximately 730 m/s with a total transfer time of 0.5 days will be needed to descend into a polar LLO around the Moon [68]. Approximately the same ΔV and time constraints apply for ascents back into a NRHO as well [68]. If a lunar lander would like to land on the equator, a descent into an equatorial LLO would require approximately 900 m/s of ΔV, which also holds true for the ascent back into the NRHO [68]. Figure 5 from [68] shows approximate ΔV costs for descents from a NRHO into a LLO summed with the corresponding ascents back into NRHO as a function of LLO orbital location.

Additional advantages to positioning the Gateway in a NRHO include a relatively low cost of station-keeping, or ΔV required to maintain the Gateway's positioning in that particular orbit. For NRHOs about the L2 point specifically, an average of approximately 4.8 cm/s of ΔV would be required per lunar orbit (an orbital period of approximately 7 days is expected for the Gateway's initial orbit) [68] [51]. In regards to communications advantages with the Earth, spacecraft in a NRHO continuously maintain a line of sight with Earth, thus potentially enabling consistent communications [68]. For lunar surface communication capabilities, NRHOs also provide some of the best coverage of the lunar surface, relative to the other candidate orbits evaluated in [68], due to their inclination "with respect to the ecliptic" [68]. Figure 7 of [68] presents the percentage of communications coverage that a spacecraft in an "L2 south family halo" NRHO would have of the lunar surface, as a function of lunar surface location [68].

Finally, it is important to note that spacecraft in a NRHO would be able to appropriately manage the heat incurred from orbital exposure to the Sun, given current spacecraft radiator technology [68].

Table 6 of [68] provides a summary of the benefits associated with placing the Gateway in a NRHO, relative to the other candidate orbits analyzed by the NASA-published paper [68].

1.4 Chapter Conclusion

Understanding why the NRHO family was selected to host the Gateway is important not only because it allows the reader to understand more about the Gateway's Concept of Operations (CONOPS), but because it also highlights some of the PPE's/Gateway's nominal operating parameters that could influence the design of a CSI mitigation strategy. Understanding the technical requirements of both the PPE and the related astrodynamics will play a crucial role in the preparation of the simulation environment.

Chapter 2

Case Studies

In Chapter 1, the Gateway was introduced from both a programmatic and a technical standpoint. This included an overview of the PPE's high-level requirements, propulsion capabilities, and the astrodynamics relevant to its insertion and operations within the NRHO family of orbits. Knowledge of the Gateway mission and specifics regarding its first module, the PPE, is important to know for the development of a CSI mitigation strategy for the Gateway. Chapter 2 focuses on the application of knowledge presented in Chapter 1 to understand more of the maneuvers that the PPE will be expected to perform throughout its lifetime. In lunar orbit, the Gateway will have to perform periodic station-keeping burns, transitions into and within the NRHO family, and changes in attitude to accommodate a variety of operations (e.g., docking with visiting vehicles, adhering to regulations surrounding various keep-out zones, thermal regulation maneuvers, scientific observations and experiments, etc.).

The value of examining these details is rooted in the necessity of creating a simulation environment that is able to accurately test each of the CSI mitigation strategies that are introduced in Section 1.2 and elaborated upon in Chapter 4. The goal of Chapter 2 is to develop case studies that will provide simulation environments representative of maneuvers that the Gateway will be expected to routinely perform in its mission orbit.

Creating the simulation environment can be broken down into two components: creating the PPE structural simulation model (Chapter 3) and designing the simulation case studies that the structural model will be tested in (Chapter 2) under the various CSI mitigation strategies. Case Study 1 is a translational burn and Case Study 2 is an attitude change maneuver.

2.1 Simulation Time Space

The Gateway's orbital period will be approximately one week [68] [51], indicating long time periods in which the spacecraft would be able to accomplish orbital station-keeping tasks at apolune [51]. Additionally, studies conducted on orbital transfer maneuvers done by the PPE show SEP burn times on the order of several weeks [51]. For example, a sample transition from an NRHO to a Distant Retrograde Orbit (DRO) provided in [51] lists a total transit time of 155.7 days [51]. The total amount of time that the SEP system will be thrusting during this transit time is computed to be 37.8 days with a total ΔV of 85 m/s [51]. This is because the PPE's onboard SEP system is capable of low-thrust, extended duration burns. The point behind highlighting these examples is to show that if time were not a constraining factor, CSI mitigation would not be a significant concern, as lower force- or torque-inducing maneuvers could avoid the excitation of normal modes of vibration and stresses caused by significant loads at various dominant structural modes of vibration. Therefore, the presented case studies present maneuvers intended for completion on the order of minutes from the maneuver start time. This will ensure that each CSI mitigation strategy is tested for their effectiveness, so that each control methodology plays a valuable and necessary role in reducing excitations and mitigating induced loads.

2.2 CSI Mitigation Strategy Actuation Capabilities

As it was introduced in Chapter 1, the Gateway has two propulsive sources of actuation (i.e., the SEP and the RCS) and at least one source of non-propulsive actuation (i.e., CMGs and/or RWs) that can be used to conduct both three-axis attitude control and/or translational maneuvering. However, not every CSI mitigation strategy can provide a control input that considers each actuation source aboard the Gateway. Some CSI mitigation strategies are conceptually incapable of providing the proper control input. The list below details the specific variable type produced by each actuation type available on the PPE:

1. **Propulsive Sources of Actuation**:
   (a) *SEP*: The SEP system is capable of producing a semi-continuous thruster output. This means that the SEP thruster, as defined in the PPE high-level requirements document, will output thrusts and torques between a non-zero minimum and maximum [53], including an "off" condition in which the total thrust or torque output is zero. The minimum and maximum SEP thruster force and torque input values are calculated in Section 3.2.1.
   (b) *RCS*: The RCS is capable of producing a binary thruster output. This means that the RCS is capable of being in an "on" or an "off" state, yielding a maximum thruster output or a thruster output of 0. A discussion on the value of the "on" thruster output value used in the simulation space is provided in Section 3.2.2.

2. **Non-Propulsive Sources of Actuation**:
   (a) *CMG/RW*: The CMG/RW system is capable of producing a continuously variable thruster output. This means that all values from 0 Nm to a defined maximum value are valid. A discussion on the maximum CMG/RW torque employed in the simulation space is presented in Section 3.2.3. As it was mentioned in Section 1.3.1, the CMG/RW actuation source is only relevant to the PPE's rotational state-space model.

Each of the five CSI mitigation strategies and their specific controller inputs to a simulation model are detailed below:

1. **Phase Plane**: Phase plane controllers, as introduced in Chapter 1, provide binary control inputs and are unable to provide continuously variable or semi-continuous control inputs. This means the phase plane CSI mitigation strategy

can only provide control action made possible by the binary RCS system in the Gateway simulation environment.

2. **PID**: PID controllers provide a continuous control input. This excludes them from being able to provide RCS control inputs, but allows them to provide actuation support readable by the continuous modes of actuation aboard the Gateway (i.e., the SEP or the CMG/RW). The PID controller evaluated in this thesis is Single Input Single Output (SISO), meaning that it can only provide a controller input for one control actuation source at a time.

3. **LQR**: Similar to PID controllers, LQR controllers provide continuous control inputs. This constrains them to considering the SEP system for the translational model or the CMG/RW system(s) for the rotational model.

4. **FWLQR**: FWLQR controllers also provide continuous control inputs readable by either the Gateway's SEP actuation system or the CMG/RW non-propulsive system.

5. **MPC**: MPC is the only candidate control methodology evaluated in this thesis that can consider binary-, semi-continuous-, and continuous-input actuation sources separately or in combination for a simulation. MPC employs constrained optimization, which allows flexible input constraints to accommodate the realities of the various types of actuators available on the PPE.

Due to the varying capabilities of the methodologies presented above, one CSI mitigation strategy (MPC) can accommodate multiple simulation runs of varying actuation sources, while the others are only able to use one actuation source to generate control input data. The MPC methodology is capable of considering RCS, SEP, and/or CMG/RW actuators separately or in any of the six possible combinations. On the contrary, the phase plane control methodology is, in its presented state, incapable of generating firing sequences for continuously-variable control inputs (i.e., the SEP system or the CMG /RW system). An experiment is presented during the MPC simulation results (Section 5.1.5) in which the RCS actuation type is converted into a continuously-variable control input. This method is capable of being extended to the PID, LQR, and FWLQR CSI mitigation strategies, and is also presented as a potential area of future work in Section 6.3.

For Case Study 1 (the translational case study), the only two possible sources of actuation are the RCS and the SEP. None of these actuator systems consider continuously variable inputs, which will make the PID, LQR, and FWLQR incapable of being tested in the translational Case Study. An assumption made during the execution of these CSI mitigation strategies in Case Study 1 is that the continuous-time control inputs can be converted into a semi-continuous input force with the use of a limiting function. This limiting function considers the continuous control input computed by each controller in Case Study 1 simulations, and limits it to the semi-continuous bounds presented in Section 3.2.1. Although this is eventually linked to degraded performance in Chapter 5's simulation outputs, this assumption is grounded in the realities of actual control systems. In many real-world examples, even if the control law is not intrinsically capable of taking into account certain constraints or idiosyncrasies, enforcing these after the control law sometimes leads to usable control action. An analogous example is the use of linear control law design techniques to implement a controller for nonlinear systems, which all real systems are.

2.3 Orbital Maneuvers: Turn-to-Burn

The maneuvers that the Gateway will execute on orbit can be classified into two primary groups: transitions into and out of various lunar-centric orbits, and station-keeping (i.e., orbital maintenance) within the currently deployed orbit. Orbital transitions for the Gateway are characterized by extended burns to other orbits both within and beyond the NRHO family. These are expected, as the Gateway will be required to insert into its initial NRHO deployment orbit [68], is expected to transition to additional lunar-centric orbits [68] [51], and is expected to transit to a disposal orbit at the conclusion of its mission, in adherence to NASA's procedural requirements for orbital debris mitigation [6] [53]. Initial simulations for the Gateway's orbital transitions have timescales on the order of multiple weeks [53]. Additional simulations show that some orbital transitions may require amounts of ΔV on the order of tens of m/s [51]. Orbital maintenance, or station-keeping, is best described as a ΔV requirement by a spacecraft to maintain its stability in a particular orbit. The PPE requirements document mentioned the need for the station to support 10 m/s of ΔV per year of the Gateway's operation [53]. With an orbital period of approximately one week [68] [51], the Gateway will need to provide approximately 10 m/s divided by 52 weeks yields 19.23 cm/s of ΔV per orbit, on average.

The PPE will be responsible for both slewing the Gateway to its designated maneuver attitude prior to each burn, and then providing the necessary station-keeping thrust to meet ΔV requirements [53]. Based off of the language provided in the PPE requirements document [53] and NASA-released concept art of the Gateway [31], we assume that the Gateway's slew to its targeted burn attitude can be considered a separate maneuver to the burn itself, in that an attitude control maneuver and a simultaneous ΔV burn are unlikely to occur simultaneously. This is hypothesized to be true for both transitions to other orbits and station-keeping maneuvers. This assumption was made primarily out of respect from the available concept art [31] assuming the presence of one SEP system at one end of the PPE.

In the PPE requirements document, it was stated that orbital maintenance should be accomplished individually or in unison by both the RCS and the SEP propulsive systems [53]. Additionally, the requirements document also introduced the use of non-propulsive attitude control actuation sources (e.g., CMGs or RWs) for attitude control [53]. Consideration of these facts has developed the author's assumption of the "Turn-to-Burn" maneuver. For all orbital maintenance and orbital transition maneuvers, the following three-stage control sequence will be assumed:

1. Perform an attitude adjustment maneuver using a combination of the non-propulsive (CMGs or RWs) or propulsive (SEP system and RCS) actuation sources.
2. Perform the orbital maintenance burn using the SEP system, the RCS, or both.
3. Perform an attitude adjustment maneuver using non-propulsive or propulsive

actuation back to the original attitude, or a newly intended attitude.

Figure 2-1 provides the reader with a visualization of the "Turn-to-Burn" maneuver.

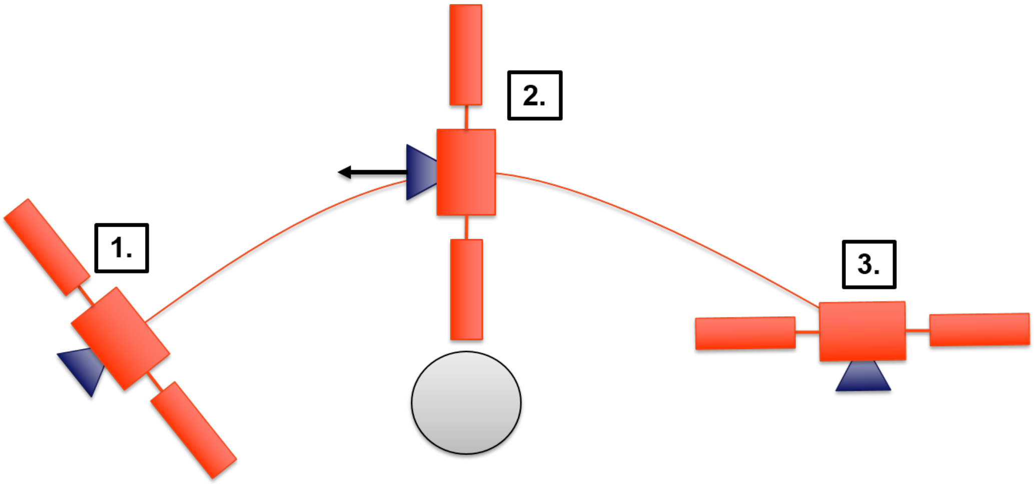

Figure 2-1: "Turn-to-Burn" Maneuver Visualization

2.4 Case Study 1: Translation

The PPE has a well-defined need to perform translation maneuvers following and preceding the attitude adjustment maneuvers provided in the "Turn-to-Burn" control sequence. In Case Study 1, the PPE is commanded to translate forward in its one-dimensional simulation space by 1.5 meters. This simulation is done using the translational LTI simulation model developed in Chapter 3. The following list details the number of simulation runs that each CSI mitigation strategy will be subjected to, with a note presented on the specific actuators that accompany each of the runs:

1. **Phase Plane**: The phase plane CSI mitigation strategy has two simulation runs allocated using the binary "on-off" RCS propulsive jets: one with the notch filters and one without them on the feedback channels. This will allow the reader to see the value of the notch filter approach in removing potentially load-inducing or destabilizing frequencies on the feedback channel of the control architecture which became an important addition to the Space Shuttle's On-Orbit DAP in the 1990s (expanded upon in Section 4.1).

2. **PID**: The PID CSI mitigation strategy has one simulation run allocated using the semi-continuous SEP propulsive system. This will require the continuous to semi-continuous limiting function developed for Case Study #1, as discussed in Section 2.2.

3. **LQR**: The LQR CSI mitigation strategy has three allocated simulation runs using the semi-continuous SEP propulsive system. This will require the continuous to semi-continuous limiting function developed for Case Study #1, as discussed in Section 2.2. The first simulation run will introduce the reader to the fundamental capabilities of the LQR by manipulating the cost weighting matrices present in the cost function. The second simulation run is dedicated to evaluating the PPE's performance in an LQR cost function configuration emphasizing the primary 1.5-meter translation control objective. The third simulation run demonstrates the performance limitations of the semi-continuous limiting function by allowing the continuously-variable LQR control input to feed directly into the plant model.

4. **FWLQR**: The FWLQR CSI mitigation strategy has two allocated simulation runs using the semi-continuous SEP propulsive system. The first simulation run will provide an example of a simulation result without frequency weighting, and the second simulation run will use the same cost weighting matrix setup with the frequency penalization option "on."

5. **MPC**: The MPC CSI mitigation strategy has six allocated simulation runs using a combination of one or both the SEP system and/or the RCS. The first, third, and fourth simulation runs consider both the semi-continuous SEP system and the binary RCS system, while the second, fifth, and sixth renditions consider the experimental continuous RCS ΔV input variable. Together, these six simulation runs demonstrate the MPC controller's ability to consider multiple actuation inputs of varying data types with constraints, frequency weighting, and the ability to enforce output constraints.

The number of simulation runs allocated to each CSI mitigation strategy for Case Study #1, in combination with the type of actuator(s) used, is included in Table 2.1.

CSI Mitigation Strategy	**Simulation Run Number**	**Actuator(s) Used**
Phase Plane	1	RCS
	2	RCS
PID	1	SEP
LQR	1	SEP
	2	SEP
	3	SEP
FWLQR	1	SEP
	2	SEP
MPC	1	SEP, RCS
	2	ΔV RCS
	3	SEP, RCS
	4	SEP, RCS
	5	ΔV RCS
	6	ΔV RCS

Table 2.1: Case Study #1 Simulation Breakdown

2.5 Case Study 2: Attitude Control

In addition to the well-defined need to conduct translation maneuvers, the PPE will be expected to perform routine attitude change maneuvers. In Case Study 2, the PPE is commanded to rotate by 180° in one-dimensional space. This simulation is done using the rotational LTI simulation model developed in Chapter 3. The following list details the number of simulation runs that each CSI mitigation strategy will be subjected to, with a note presented on the specific actuators that accompany each of the runs.

1. **Phase Plane**: The phase plane CSI mitigation strategy for the rotational model, exactly like the one for the translational model, has two simulation runs allocated using the binary “on-off” RCS propulsive jets: one with the notch filters and one without them on the feedback channel. This will allow the reader to see the value of the notch filter approach in removing potentially load-inducing or destabilizing frequencies.

2. **PID**: The PID CSI mitigation strategy has one simulation run allocated using the continuous CMG/RW non-propulsive actuation system.

3. **LQR**: The LQR CSI mitigation strategy has one allocated simulation run using the continuous CMG/RW non-propulsive actuation system.

4. **FWLQR**: The FWLQR CSI mitigation strategy has two allocated simulation runs using the CMG/RW non-propulsive actuation system. The first simulation will demonstrate a case without frequency weighting, and the second simulation will demonstrate a case with the penalization of an indicated frequency.

5. **MPC**: The MPC CSI mitigation strategy has one allocated simulation run. Case Study 1 provided a comprehensive review of the control methodology's capabilities, with the exception of providing simulation results for a continuously variable actuator input data type that provides a torque. The CMG/RW non-propulsive actuation system will the sole source of actuation tested in Case Study #2 for MPC.

The number of simulation runs allocated to each CSI mitigation strategy for Case Study #2, in combination with the type of actuator(s) used, is included in Table 2.2.

CSI Mitigation Strategy	**Simulation Run Number**	**Actuator(s) Used**
Phase Plane	1	RCS
	2	RCS
PID	1	CMG/RW
LQR	1	CMG/RW
FWLQR	1	CMG/RW
	2	CMG/RW
MPC	1	CMG/RW

Table 2.2: Case Study #2 Simulation Breakdown

2.6 Chapter Conclusion

The goal of Case Studies #1 and #2 is to develop case studies that will provide simulation environments representative of maneuvers that the Gateway will be expected to routinely perform in its mission orbit. With each case study now framed, the next step in preparing the simulation environment will be to model the subject of each maneuver, the PPE and solar array combination. Following the development of a PPE + solar array state-space model for both translational (Section 3.1.1) and rotational (Section 3.1.2) maneuvers, the propulsive (the SEP and RCS systems) and non-propulsive (CMGs or RWs) will also be characterized further to allow for adaptation within the simulation environment (Section 3.2).

Chapter 3

Simulation Environment

There is a strong heritage relating the use of simple, LTI state-space systems to the synthesis of control laws. In [70], the authors use simple mass-spring-damper systems to describe a control method capable of the "suppression of deflection during... slew and [the] elimination of residual oscillations." Similarly, in [66], optimal controllers are designed for use in the frequency domain for the purpose of simulating the dynamic responses of large, flexible space structures as a result of control inputs. This approach was also taken by Space Shuttle GNC engineers during the operational phase of the Inertial Upper Stage (IUS) [63]. The author of [63] writes, in regards to rotational model control design, that "often one could assume one dominant flex mode in the pitch plane associated with the rotation mechanism, essentially a spring at a hinge" [63]. The author of [63] goes on to state that "many beam-like payloads could be similarly simplified with one dominant mode in the pitch plane and one in the roll plane, each independent of the other... the simplified models usually sufficed until the later Shuttle-Mir and Shuttle-Space Station dockings."

Similar to the publications presented above, the purpose of this thesis is to design control strategies that can be applied towards large, flexible space structures. Although more advanced models (e.g., friction coefficients, frequency dependent stiffnesses, time-varying coefficients, state-dependent dynamics, more structural elements, etc.) are required to effectively test control strategies, there is a clear precedent supporting the use of simplistic structural simulation models to design various control methods. In the spirit of this heritage, a simple translational and rotational LTI system is considered to be the foundational simulation environment in which to test the CSI mitigation strategies established in Chapter 1 that can, in the future, be applied to more advanced simulation models.

3.1 LTI State-Space Systems

In controls engineering, LTI systems are frequently represented as state-space models. LTI state-space systems can be "described by linear differential equations with constant coefficients," reducing state-space models into "a set of n coupled first-order linear differential equations with constant coefficients" [62]. This greatly reduces the complexity of state-space system dynamics, which allows for a focus on control law synthesis for a representative model.

The continuous-time LTI state-space systems for both the translational and rotational PPE simulation models take on the following form:

$$\begin{gathered}\dot{x}(t) = A_C x(t) + B_C u(t)\\ y(t) = C_C x(t) + D_C u(t)\\ \text{where time } t \in \mathbb{R}.\end{gathered}$$

The discrete-time LTI state-space system for both models takes on the following format:

$$\begin{gathered}x(k+1) = A_D x(k) + B_D u(k)\\ y(k) = C_D x(k) + D_D u(k)\\ \text{where step index } k \in \mathbb{Z}.\end{gathered}$$

The implementation of each CSI mitigation strategy will be done in discrete-time. The following enumerated list provides a description of each of the terms presented in the state-space models above.

1. $x(t)$: The *state vector* written as a function of continuous time. $x(t) \in \mathbb{R}^n$, where n is the number of states.

2. $x(k)$: The *state vector* written as a function of discrete time. $x(k) \in \mathbb{R}^n$.
3. $y(t)$: The *output vector* written as a function of continuous time. $y(t) \in \mathbb{R}^m$, where m is the number of outputs.
4. $y(k)$: The *output vector* written as a function of discrete time. $y(k) \in \mathbb{R}^m$.
5. $u(t)$: The *input vector* written as a function of continuous time. $u(t) \in \mathbb{R}^p$, where p is the number of inputs.
6. $u(k)$: The *input vector* written as a function of discrete time. $u(k) \in \mathbb{R}^p$.
7. A_C: The *state transition matrix* of the continuous-time model, which has the dimensions $n \times n$.
8. A_D: The *state transition matrix* of the discrete-time model, which has the same dimensions as its continuous-time counterpart A_C.
9. B_C: The *input distribution matrix* of the continuous-time model, which has the dimensions $n \times p$.
10. B_D: The *input distribution matrix* of the discrete-time model, which has the same dimensions as its continuous-time counterpart B_C.
11. C_C: The *output matrix* of the continuous-time model, which has the dimensions $m \times n$.
12. C_D: The *output matrix* of the discrete-time model, which has the same dimensions as its continuous-time counterpart C_C.
13. D_C: The *feedforward matrix* of the continuous-time model, which has the dimensions $m \times p$.
14. D_D: The *feedforward matrix* of the discrete-time model, which has the same dimensions as its continuous-time counterpart D_C.

3.1.1 Translational LTI System

In accordance with the precedent to develop control methodologies for large, flexible space structures on simple, mass-spring-damper LTI systems along one dimension, a simple model was created for the Gateway's linear dynamics (Figure 3-1).

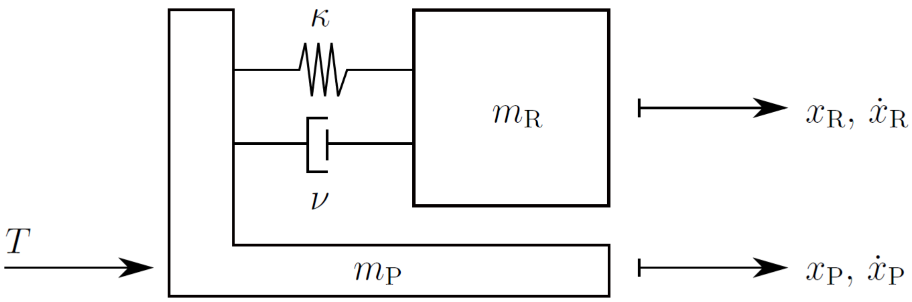

Figure 3-1: Linear LTI System: Control-relevant Dynamics Model

The following list defines each of the variables used within the translation model depicted in Figure 3-1:

1. m_R: This variable denotes the mass of the solar array, which was assumed to be 250 kg. This value was based off of the mass of the ISS's ROSA solar array, which is estimated to be less than 500 kg [8]. The ROSA, developed by the Air Force Research Laboratory and Deployable Space Systems, Inc. [8], is a concept candidate [28] for providing the 300 kW of power needed for supporting the PPE [53]. Seeing as the Gateway is planned to be smaller than the ISS, and considering the advances in solar array technology since the ISS's era [59] [60] [14], the solar array mass for all simulations was assumed to be 250 kg.

2. m_P: This variable denotes the mass of the PPE, which was provided in [53] to be 8000 kg.

3. ν: This variable denotes the value of the viscous damping coefficient, which was assumed to be 0.01 N /(m/s) based off of existing precedent [43]. The focus of this thesis is to evaluate CSI mitigation strategies that can potentially dampen

the effects of a thrust- or torque-inducing input without the added value of a passive damping capability. Keeping the effects of a passive damper low allows for a greater focus on the CSI mitigation strategy in the attempts to accomplish the vibration management control objective.

4. κ: This variable denotes the value of the spring coefficient, which was calculated to be 99 N/m from the following equation describing the simple and harmonic motion of a mass (in this case, the mass of the solar array m_R) [54]:

   $$2\pi f = \sqrt{\tfrac{\kappa}{m_R}}\ \kappa = (2\pi f)^2 m_R$$

   where f represents the natural frequency in Hz. The natural frequency of the solar array was chosen to be 0.1 Hz, based upon sources suggesting solar array natural frequencies to be at around this magnitude [36] [57] [52]. With the mass of the solar array already assumed, the value of κ can be calculated from the equations above:

   $$\kappa = (2\pi(0.1\,\mathrm{Hz}))^2(250\,\mathrm{kg}) = 98.696\,\mathrm{Nm}^{-1} \simeq 99\,\mathrm{Nm}^{-1}$$

5. $x_R, \dot{x}_R$: The variable x_R represents the displacement that the solar array has from its point of origin as a function of time, while its derivative $\dot{x}_R$ represents the solar array's velocity at a particular point in time.

6. $x_P, \dot{x}_P$: The variable x_P represents the displacement that the PPE has from its point of origin as a function of time, while its derivative $\dot{x}_P$ represents the PPE's velocity at a particular point in time.

Figure 3-1 presents a model that is linear and one-dimensional, with all quantities being positive to the right. The next step is to provide the continuous-time state-space dynamics for the translational LTI model, in accordance with the format provided in Section 3.1:

$$
\begin{aligned}
x(t) &= \begin{bmatrix} x_P \\ \dot{x}_P \\ x_R \\ \dot{x}_R \end{bmatrix} \in \mathbb{R}^n \\
u(t) &= \begin{bmatrix} T \end{bmatrix} \in \mathbb{R}^p \\
A_C &= \begin{bmatrix} 0 & 1 & 0 & 0 \\ -\frac{\kappa}{m_P} & -\frac{\nu}{m_P} & \frac{\kappa}{m_P} & \frac{\nu}{m_P} \\ 0 & 0 & 0 & 1 \\ \frac{\kappa}{m_R} & \frac{\nu}{m_R} & -\frac{\kappa}{m_R} & -\frac{\nu}{m_R} \end{bmatrix} \in \mathbb{R}^{n\times n} \\
B_C &= \begin{bmatrix} 0 \\ \frac{1}{m_P} \\ 0 \\ 0 \end{bmatrix} \in \mathbb{R}^{n\times p} \\
D &= \begin{bmatrix} 0 \end{bmatrix} \in \mathbb{R}^{m\times p} \\
n &= 4
\end{aligned}
$$

The variables m and p, which represent the number of outputs and inputs respectively, vary based off of each individual case study and CSI mitigation strategy. T represents the thrust matrix; its size (given by p) will vary depending on the actuators selected for the simulation. A discussion of these various types is included in Section 3.2. Additionally, the output matrix C will vary depending on each CSI mitigation strategy. For example, the PID controller implemented in this thesis is only capable of SISO control, and will have a $1 \times n$ matrix dimension. The output matrix is defined individually in the presentation of each control methodology in Chapter 4.

3.1.2 Rotational LTI System

To test the rotational dynamics of the Gateway, a separate LTI system was developed. Similar to the translational LTI systems, rotational systems have a heritage of simplicity in the area of spacecraft control design [70] [63]. In accordance with precedent, the following LTI model was developed to provide simulation results for the Gateway's rotational dynamics (Figure 3-2).

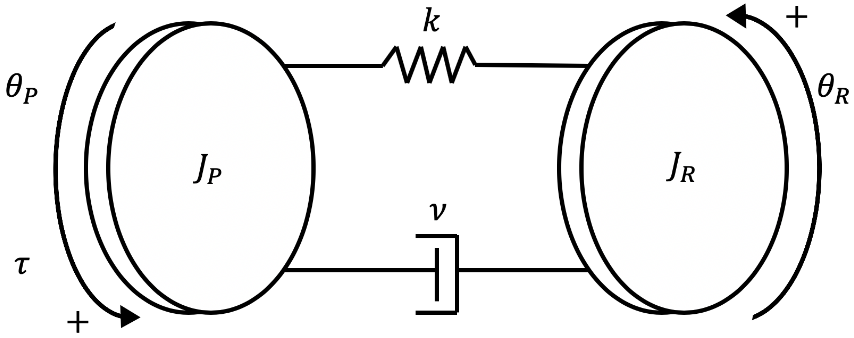

Figure 3-2: Rotational LTI System: Control-relevant Dynamics Model

The following list defines each of the variables used within the rotational model depicted in Figure 3-2, and comments on their specific value.

1. J_P: This variable denotes the mass moment of inertia of the PPE. In order to complete this calculation, the PPE was assumed to be a cylinder, as depicted in Figure 3-3.

   The z-axis, as depicted in Figure 3-3, is the intended axis of rotation for the PPE. It is assumed that the circular faces of the cylindrical PPE will host the SEP system on one end and a docking port to an additional module on the other [31], while the solar array will be connected to the outer cylindrical face of the PPE, defined in height by h in Figure 3-3. The mass moment of inertia equation for a cylinder about the z axis of rotation is as follows [27]:

$$I_z = \tfrac{1}{2}mr^2.$$

   Not much is publicly available in regards to the structural dimensions of the PPE, which is understandable as the module is still in its conceptual stages of

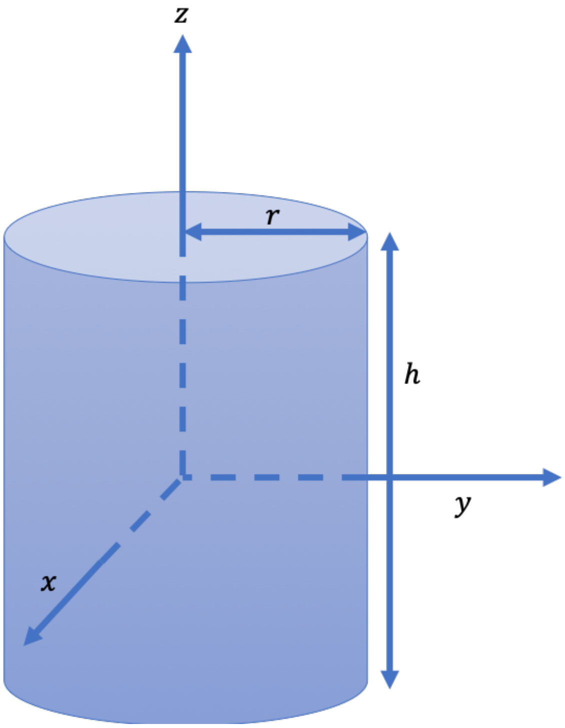

Figure 3-3: Cylinder with 3-D Axes of Rotation

development at the time of this thesis' composition. Therefore, the radius r of the PPE was assumed to be that of the ISS's Zarya module in order to complete this calculation. The Zarya's radius is approximately 2.06 m [10], and the mass of the PPE was provided in [53] to be 8000 kg. Therefore:

$$I_z = \tfrac{1}{2}(8000\,\mathrm{kg})(2.06\,\mathrm{m})^2 = 16974.4\,\mathrm{kg}\cdot\mathrm{m}^2\,.$$

The PPE's mass moment of inertia was therefore assumed to be $16974.4\,\mathrm{kg}\cdot\mathrm{m}^2$.

2. J_R: This variable denotes the mass moment of inertia of the solar array. In order to complete this calculation, the solar array was assumed to be a rectangular plate (as demonstrated in Figure 3-4); i.e., a flat rectangle with a negligible height in the z-axis.

   It is assumed that the solar array will be connected to the PPE parallel to the x-axis of rotation. This means that, in accordance with the nomenclature of Figure 3-4, the hinge connecting the solar array to the PPE will be flush

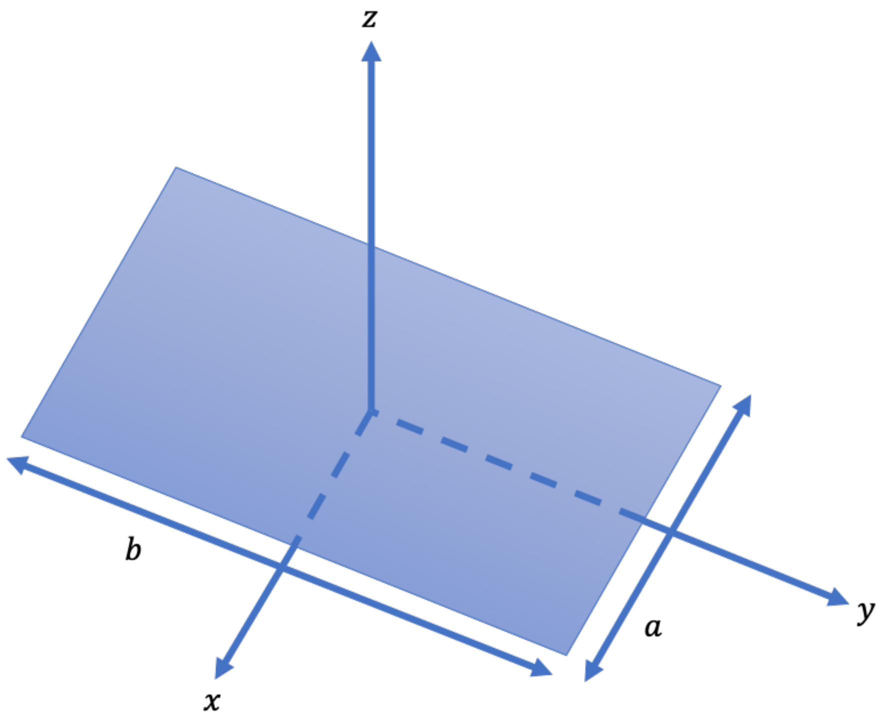

Figure 3-4: Rectangle with 3-D Axes of Rotation

with the side whose length is defined by the variable a. Figure 3-5 includes a visualization of this connection.

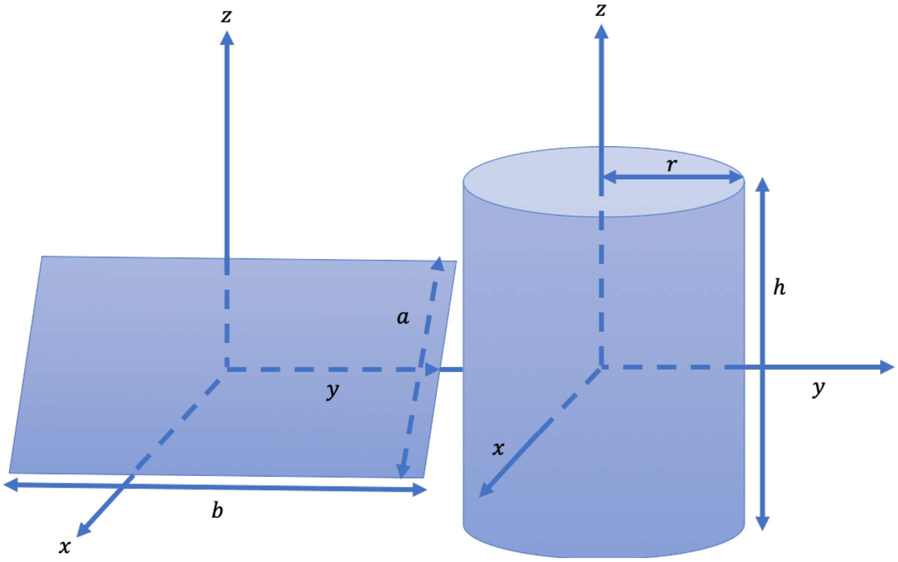

Figure 3-5: Cylinder and Rectangle with 3-D Axes of Rotation

Considering this connection and the defined axes of rotation in Figures 3-3, 3-4, and 3-5, the axis of rotation that the PPE will rotate about is the same as that of the solar array. The mass moment of inertia equation for rectangular plates about the x-axis is as follows [17]:

$$I_x = \tfrac{1}{2} m_R b^2.$$

The variable b denotes the extended length of the rectangular solar array wing. With the PPE concept still under development and the solar array information not yet available, a solar array wing size had to be assumed. The ISS was once again referenced for this matter. Each ISS solar array wing has a length of 32.9 meters [59], but considering a variety of advances in solar array technology, the assumed length of the PPE's solar array was decreased to 25 meters [14]. The mass of the solar array, as discussed in Section 3.1.1, was approximated to be 250 kg, based off of the estimated mass of each solar array wing [8]. Therefore:

$$I_x = \tfrac{1}{2}(250\,\mathrm{kg})(25\,\mathrm{m})^2 = 78125\,\mathrm{kg}\cdot\mathrm{m}^2\,.$$

The mass moment of inertia of the solar array wing is therefore assumed to be $78125\,\mathrm{kg}\cdot\mathrm{m}^2$.

3. ν: This variable denotes the value of the viscous damping coefficient, which was assumed to be 0.01 $\mathrm{N}/(\mathrm{m/s})$ based off of existing precedent [43]. The focus of this thesis is to evaluate CSI mitigation strategies that can potentially dampen the effects of a thrust- or torque-inducing input without the added value of a passive damping capability. Keeping the effects of a passive damper low allows for a greater focus on the CSI mitigation strategy in the attempts to accomplish the vibration management control objective. This value remains unchanged from the translational LTI state-space model.

4. κ: This variable denotes the value of the spring coefficient, which was calculated to be 6701 N/m. This spring coefficient was calculated from the following equation that defines simple harmonic motion for a torsional spring attached to an inertial mass [64].

$$\omega = \sqrt{\frac{\kappa}{J_P}} \; \kappa = (\omega)^2 J_R$$

where ω represents the natural angular frequency in Hz, which is computed by multiplying 2π by the desired resonant frequency. The natural frequency of the solar array was chosen to be 0.1 Hz, based upon sources suggesting solar array natural frequencies to be at around this magnitude [36] [57] [52]. With the mass of the solar array already assumed, the value of κ can be calculated from the equations above:

$$\kappa = (2\pi(0.1\,\mathrm{Hz}))^2(16974.4\,\mathrm{kg}\cdot\mathrm{m}^2) = 6701.22\,\mathrm{Nm}^{-1} \simeq 6701\,\mathrm{Nm}^{-1}$$

The spring constant of the torsional spring that connects the PPE and the solar array on the rotational model is therefore assumed to be $6701\,\mathrm{Nm}^{-1}$.

5. $\theta_R, \dot{\theta}_R$: The variable θ_R represents the angular displacement that the solar array has from its point of origin as a function of time, while its derivative $\dot{\theta}_R$ represents the solar array's angular velocity as a function of time.

6. $\theta_P, \dot{\theta}_P$: The variable θ_P represents the angular displacement that the PPE has from its point of origin as a function of time, while its derivative $\dot{\theta}_P$ represents the PPE's angular velocity as a function of time.

Figure 3-2 presents a model that is linear and one-dimensional, with all quantities being positive in the counterclockwise direction when viewing the rotational control-relevant dynamics model from the right. The next step is to provide the continuous-time state-space dynamics for the rotational LTI model, in accordance with the format provided in Section 3.1:

$$\begin{aligned}
x(t) &= \begin{bmatrix} \theta_P \\ \dot{\theta}_P \\ \theta_R \\ \dot{\theta}_R \end{bmatrix} \in \mathbb{R}^n \\
u(t) &:= \begin{bmatrix} \tau \end{bmatrix} \in \mathbb{R}^p \\
A_C &= \begin{bmatrix} 0 & 1 & 0 & 0 \\ -\frac{K}{J_P} & -\frac{B}{J_P} & \frac{K}{J_P} & \frac{B}{J_P} \\ 0 & 0 & 0 & 1 \\ \frac{K}{J_R} & \frac{B}{J_R} & -\frac{K}{J_R} & -\frac{B}{J_R} \end{bmatrix} \in \mathbb{R}^{n \times n} \\
B_C &= \begin{bmatrix} 0 \\ \frac{1}{J_P} \\ 0 \\ 0 \end{bmatrix} \in \mathbb{R}^{n \times p} \\
D_C &= \begin{bmatrix} 0 \end{bmatrix} \in \mathbb{R}^{m \times p} \\
n &= 4
\end{aligned}$$

The variables m and p, which represent the number of outputs and inputs respectively, vary based off of each individual case study and CSI mitigation strategy. τ represents the induced torque matrices of various actuator inputs; it is a function of the number of outputs p. A discussion of these various types is included in Section 3.2. As with the translational LTI system, the output matrix C will vary depending on each CSI mitigation strategy. The output matrix is defined individually in the presentation of each control methodology in Chapter 4.

3.2 Actuator Input Values

The force (T) and torque (τ) matrices introduced in the translational and rotational LTI models are unlike the constants contained in the state (A) and input (B) matrices. This is because the value of these matrices will differ from simulation to simulation, as discussed in chapter two, per the type of actuator(s) used. This section will provide a review of the values of T and τ for each of the PPE's available actuators.

In chapter one, the requirements of the PPE introduced two propulsive (the SEP system and the RCS) and one non-propulsive source of actuation (a CMG or RW system) [53]. The propulsive sources of actuation are the only force-inducing sources of actuation aboard the PPE, and are both applicable to the translational LTI model. For the rotational model, the SEP system, the RCS, and the CMG or RW non-propulsive actuation source are capable of inducing torques.

The next three subsections are dedicated to the calculation of the thrusts and torques that each of the aforementioned actuation sources are capable of producing in the simulation space.

3.2.1 Solar Electric Propulsion (SEP) Actuation

The following requirements are taken verbatim from [53], and relate to the thruster output capabilities of the PPE's onboard SEP system:

1. **NU-PPE-1898**: "The PPE Flight System shall utilize an electric propulsion string that throttles with variable inputs powers from 7 kW to at least 10 kW" [53].

2. **NU-PPE-1900**: "The PPE Flight System shall utilize an electric propulsion system with the capability to operate over a thrust-to-power ratio range of at least 43 - 52 mN/kW." [53].

These two requirements provide the basis for assuming the SEP's capable thrust range. Requirement NU-PPE-1898 refers to the SEP system as being throttleable with a minimum and a maximum input power and thrust-to-power ratio. This suggests that the PPE's thrust can be modeled as a semi-continuous variable, meaning that it can achieve any thrust output within a minimum and maximum range greater than 0. If the thrust output does not fall within this range, it is 0.

With the thrust-to-power ratio range and the variable input power values, the SEP's thrust output range can be computed:

$$\begin{gathered}\textit{Minimum Thrust}\text{:}\\ (7\,\mathrm{kW})(43\,\mathrm{mN}\,/\,\mathrm{kW}) = 301\,\mathrm{mN} = 0.301\,\mathrm{N}\\ \textit{Maximum Thrust}\text{:}\\ (10\,\mathrm{kW})(52\,\mathrm{mN}\,/\,\mathrm{kW}) = 520\,\mathrm{mN} = 0.520\,\mathrm{N}\,.\end{gathered}$$

It is assumed that the SEP will be capable of producing 0.301 Nm - 0.520 Nm of torque for the rotational LTI model.

3.2.2 Reaction Control System (RCS) Actuation

The PPE requirements document did not mention specific RCS thrust values. Therefore, a reference thruster value will be used. The ISS's RCS systems hosts clusters of 200 N thrusters to perform orbital reboosts [19]. The Space Shuttle's Vernier RCS jets are capable of exerting 106 N of thrust. The Vernier thrusters were primarily responsible for providing attitude control for the Shuttle [63]. Due in part to the ISS being larger in size than the Gateway is predicted to be, the RCS jet thruster outputs that were used on the Space Shuttle will provide the reference force values for the PPE's RCS.

3.2.3 Non-Propulsive Actuation

The Space Shuttle did not have CMGs or RWs. The ISS, however, had CMG's capable of providing up to 258 Nm of torque. These values will be used for the non-propulsive actuation option in the simulation space [55].

Chapter 4

Summary of Control Methodologies

Chapter 3 saw the introduction of the linear LTI state-space models that define the translational (Section 3.1.1) and rotational (Section 3.1.2) dynamics for the PPE with one deployed solar array. This specific configuration of the Gateway will be evaluated in the simulation space by a series of candidate control methodologies for their ability to allow the PPE to accomplish the primary control objective dictated by the specific case study in consideration (Case Study #1 presented in Section 2.4 and Case Study #2 presented in Section 2.5). In addition to completing the primary control objective of performing a translational burn (Case Study #1) or an attitude change (Case Study #2), the control methodologies presented in this chapter are evaluated for their ability to manage the oscillations of the solar array relative to the PPE that result from the control actuation inputs stemming from the PPE's efforts to accomplish the primary maneuver.

Chapter 4 presents the theory behind each CSI mitigation strategy evaluated in this thesis. All control strategies are presented in discrete-time.

4.1 Phase Plane Controller

The Space Shuttle had a total of three operations phases for nominal flight, with each operations phase having a set of major modes [72]. To help in guiding the Shuttle's flight during these various operations phases and major modes, various suites of flight control software existed in the form of three different DAPs [72]. The Space Shuttle's on-orbit DAP made use of a phase plane control system to perform 3-axis attitude control [72]. The phase plane, in the context of how the Space Shuttle applied it to its on-orbit DAP, can be visualized using a Cartesian coordinate system, i.e., a two-dimensional coordinate plane with error (θ^B_{error}) being represented on the horizontal axis and error rate (ω^B_{error}) being represented on the vertical axis [63]. The error and error rate calculations used to implement the phase plane logic were taken from calculated differences between the commanded attitude and the attitude reported by the DAP's Inertial Measurement Unit (IMU) [63]. Figure 2 on page 64 of [63] illustrates the control feedback loop of the Space Shuttle's on-orbit DAP.

The Space Shuttle's onboard propulsion system consisted of two Orbital Maneuvering System (OMS) jet systems that could "each produce 6000 lbf of thrust, ... six Vernier Reaction Control System (VRCS) jets of about 24 lbf thrust each, and 38 Primary Reaction Control System (PRCS) jets of about 870 lbf thrust each" [63]. The Shuttle's RCS was comprised of both the VRCS and PRCS systems. Figure 1 on page 64 of [63] describes the location of each of these RCS thrusters.

Sackett points out that "both the VRCS and the PRCS use[d] a phase plane controller with switch curves corresponding to an attitude deadband and a rate deadband (often called the rate limit)" [63]. The author of [63] goes on to mention that "within the deadbands another switch curve depends on the disturbance acceleration estimate. Other switch curves define a drift channel outside the attitude deadbands" [63]. Figure 3.3 from [72] depicts a phase plane Cartesian firing grid, in which certain jets were commanded to be "on" in one direction (f^+) or "on" in the opposite direction (f^-) based off of the Shuttle's attitude error and error rate exceeding programmed limitations imposed by engineers on the Shuttle DAP [72]. The worst case rate errors for the Shuttle DAP operating independently (i.e., not docked to the ISS) are typically on the order of 0.01° - 0.02° per second [47], which portray examples of upper limit error vs. error rate limitations used within the Shuttle's on-orbit DAP. A snapshot of the phase plane during one hour of on-orbit operations with IMU error vs. error rate information is available from the mission report of STS-71 in Figure 9, which shows a range of attitude error from approximately -5 degrees to +5 degrees [73]. The error rate oscillates between approximately -0.035 and 0.03 degrees per second [73].

The shaded areas (preference regions) in between the imposed boundaries corresponded to the area in which the relevant thrusters would not be active. Designing these boundaries were based off of decisions partially related to stability. The trade-off associated with widening or shortening the boundaries, or switching lines, associated with the phase plane diagram is, in part, one of performance versus accuracy. Of course, the decisions (and ensuing results) about where switching lines were placed differed based upon the varying structural configurations of each Shuttle mission. Wider preference areas are associated with larger acceptable differences between the commanded attitude/attitude rate and the actual attitude/attitude rate. Reducing the distance between switching lines could potentially lead to a deterioration in performance. This is because the controller, which conducts "on-off" control with binary thrusters, may cause excessive oscillations between the switching lines, which could lead to excessive stresses and loads in a short amount of time [63].

Phase plane control mechanisms were inherent to the Space Shuttle DAP design, and served the orbiter well throughout the entirety of its lifetime. An example of a phase plane plot overlain with actual flight error vs. error rate measurements was previously referenced as Figure 9 of [73], a mission report for STS-71. STS-71 was a 1995 mission, which was consisted of the first docking between the Space Shuttle and the Russian space station Mir [73].

Early in the Space Shuttle's operational flying career, concerns began to arise in regards to how the Shuttle on-orbit DAP, and the phase plane infrastructure that was foundational to its execution, would respond to various payload interactions and deployments using devices like the RMS (the Shuttle's robotic arm), or the IUS [63]. The IUS was a Boeing-developed "upper-stage booster rocket" that, upon being deployed from the Shuttle's payload bay, would propel payloads into higher Earth-based orbits, or onto transfer trajectories to other planets [23].

The cause for concern in regards to RMS and IUS usage was that "low frequency payload motion associated with certain directly attached payloads or with a payload on the RMS would have flex frequencies lower than state estimator cut-offs" [63]. This would result in potentially destabilizing frequencies that could pass through the phase plane control logic, which would risk an excitation of a specific frequency that would potentially degrade "performance or even... [lead] to a control instability" [63]. An example of this incident can be seen in the preparation for STS-6. STS-6's mission was to deploy the Tracking and Data Relay Satellite-1 (TDRS-1), and used the IUS to do so [2] [63]. The IUS + TDRS-1 package had a weight of approximately 30,000 lbs [63]. Upon being rotated to a deploy angle of 58°, the IUS + TDRS-1 + Shuttle stack had a fundamental frequency that was close to 0.1 Hz, which, upon being excited, could have lead to "poor DAP performance or even an instability" [63].

A crucial element in the remedy for these problems was the development of a high-fidelity simulation environment, which was used to model various Shuttle + payload configurations. Through simulations and careful design of the phase plane and jet pulse firing sequences, Draper was able to support NASA and the Shuttle program by preventing the excitement of dominant modes of vibration within the on-orbit DAP control loop. However, in the mid-late 1980s, more and more thought began to be put into the assembly of a space station in orbit, which inherently included large modules and other structural components. Structural elements of the size envisioned would "likely have multiple low frequency modes" that would complicate current on-orbit DAP design methods employed by Draper and NASA [63]. By 1987, an initiative was created within Draper to "try to identify and test alternative approaches to dealing with the dynamic interaction issue other than the usual operational restrictions and deadband changes" [63]. Born out of this initiative was an idea proposed in [18] involving the use of notch filters on the feedback loop of the Shuttle's on-orbit DAP (depicted on the feedback channel of Figure 2 in [63]). The fundamental idea was to filter out components of the feedback signal associated with unwanted "low-frequency bending modes" that may cause instabilities and undesired excitations when used in concert with the phase plane control system [18]. Figure 1 from [73] depicts an example of the notch filter applied to STS-71's mated operations to the Mir space station, and was taken from the aforementioned Draper-published STS-71 mission report.

Notch filters became an integral part of the Shuttle's on-orbit DAP for the Shuttle/Mir docking missions throughout the 1990s in addition to the ISS assembly & docking missions in the 2000s. The design of the notch filter, tailored to mission specifics, was a crucial part of the preparations performed by Draper for Space Shuttle flights involved with mated Mir/ISS missions. However, the notch filter approach was not without tradeoffs. Draper's process for notch filter design required a certain amount of "trial and error" [63], as "more than one notch for one flex mode may... [have provided] better performance than a single notch" [63]. Additionally, there was a tradeoff between stability and performance, as "the notches ensure[d] feedback stability,... [but they also tended] to degrade rigid body performance" [63].

During the ISS assembly and docked missions, concern existed over how the station's structural elements would respond if the PRCS thrusters, which produce 870 lbs of force [63], were implemented for control purposes. Although the VRCS jets were "naturally preferable for loads," they were "not redundant and the failure of any single VRCS jet [meant] that the VRCS [was] no longer an option for control of the stack." [48]. The challenge that existed for Shuttle control engineers was spacing the thruster firings so as not to excite dominant modes of vibration, which were becoming more and more dense with the ISS's growth (see Figure 26 in [32]). The eventual solution was the incorporation of the "variable delay" concept [48]. This concept consisted of varying the intervals between RCS firings, where "an array of 10 values [could] be loaded into the flight software that [could] scale the base interval, thus supplying a sequence of 10 non-equal intervals between firings." [48]. Finding the most appropriate sequence of intervals relied upon a brute-forcing search method (although considerable steps were taken to minimize the total number of permutations with various optimization algorithms [48]) done on the ground, which considered a multitude of possible firing sequences [48] [46]. Given modern day computational capabilities, an optimal solution considering a high-fidelity model could be found with "one computer in an afternoon" [46]. However, in the days of the Shuttle, these optimal pulse train firing sequences would require multiple processors and days of run time (done on the ground) to yield a solution [46].

In conclusion, the excitement of the dominant modes of physical objects could lead to instabilities and excessive loads for spacecraft. For large, flexible spacecraft that inherently have multiple dominant modes of vibration, the attenuation of these frequencies is a paramount objective to ensuring mission success. The Space Shuttle utilized a notch filter that, when placed on the feedback of the on-orbit DAP control loop, attenuated various frequencies that would have caused instabilities and undesired loads on associated structural elements. However, this approach was constrained to the existing Shuttle control loop architecture. In the realm of human spaceflight within the United States, the ability to evaluate additional control methodologies for their effectiveness and potential benefit over the notch filter-based approach in the Shuttle program was not applicable because of this constraint. In combination with the pulse train optimization process developed to assist in ISS CSI mitigation, the Shuttle's CSI mitigation strategy had gaps in performance and adaptability that could potentially be outperformed by other control methodologies in the context of an unconstrained architecture for new space systems. The opportunity to evaluate other strategies was not as available to the Shuttle as it is for the Gateway, which is currently in the early stages of development. Developing a controller unconstrained by the architecture of the Space Shuttle that could best optimize against potentially destabilizing interfering modes of vibration is important for the future development of large space structures.

4.2 PID Controller

PID controllers have been in existence since the early 1900s [21], and are considered to be "the most commonly used controller," as "about 90-95% of all control problems are solved by this controller" [75]. Its widespread application and relatively simple design was the primary motivation behind its inclusion in the repertoire of potential CSI mitigation strategies.

The resultant control action generated by PID controllers is comprised of three different terms: a proportional control action u_P, an integral control action u_I, and a derivative control action u_D [75]:

$$u(k) = u_P(k) + u_I(k) + u_D(k).$$

The following excerpt from [74] provides insight into what each independent control action contributes to the larger action as a whole: “The proportional part acts on the present value of the error, the integral represent and average of past errors and the derivative can be interpreted as a prediction of future errors based on linear extrapolation” [74].

4.2.1 Proportional Control Action

The proportional control action u_P is found via the following simple feedback mechanism [75]:

$$u_P(k) = K_P e(k),$$

where K_P is a scalar controller gain for the SISO system evaluated in this thesis, and $e(k)$ is the error, where:

$$e(k) = y_{SP}(k) - y(k) \text{ [75].}$$

The error is the difference between the commanded output $y_{SP}(k)$, and the current output $y(k)$ [75]. The scalar controller gain for the proportional control action is a design parameter, and can be found via automatic tuning methods. However, this thesis considers the manual selection of this scalar control gain.

4.2.2 Integral Control Action

The integral control action u_I has the following “form”:

$$u_I(k) = K_I \textstyle\sum_{i=0}^{k} e(i). \text{ [75]}$$

In the equation above, the variable i resembles a counting variable for the summation. Integral control action contributions to the PID controller ensure that “control action is taken even if the error is very small provided that the average of the error has the same sign over a long period" [75]. The K_I term is a design parameter, and the $\sum_{i=0}^{k} e(i)$ term considers the error accrued during the operation of the PID controller [75].

4.2.3 Derivative Control Action

The derivative control action u_D contributes anticipatory control action:

$$u_D(k) = K_D \frac{e(k+1)-e(k)}{\gamma} \text{ [75].}$$

In the equation above, the variable γ denotes the interval in which the finite difference is considered and calculated over. It is important to note that the control action for the derivative control action "is based on linear extrapolation of the error" over a future time interval [75]. The fundamental concept is that the derivative term considers the rate of change of the current error in an effort to "provide anticipatory action" [75].

4.3 Linear Quadratic Regulator (LQR)

The control objective of the LQR is to minimize the value of the following cost-function:

$$J = \sum_{k=0}^{\infty} [x(k)^T Q x(k) + u(k)^T R u(k)]$$

This thesis considers the design and implementation of the discrete infinite-horizon LQR. The variables Q (of dimension $n \times n$) and R (of dimension $p \times p$) are user-specified weighting variables, where Q provides a weight on the state vector and R provides a weight on the input vector (both defined in the state-space model) [45]. Although methods and good rules of thumb (such as Bryson's Rule) exist to assist in selecting values of Q and R [41], values are selected manually in this thesis' simulations (Chapter 5). As Q and R are both weighting variables, their values relative to each other are what dictate the resultant control action [44] [50] [30] [45]. A higher relative weighting on the state cost Q makes tolerating an error more expensive than implementing control inputs. This leads to more liberal control inputs in the LQR's attempt to accomplish the control objectives. If a higher weighting is placed on the input cost R, it becomes more expensive to implement control inputs. This leads to a more conservative application of control inputs as the LQR attempts to generate the control actions needed to complete the control objectives.

The controller gain K_{LQR} for the optimal LQR can be found via the optimal full state feedback control law [44] [50]:

$$u(k) = -K_{LQR}x(k)$$
$$\text{where } K_{LQR} = (B_D^T P B_D + R)^{-1}(B_D^T P A_D).$$

In the equation above, A_D and B_D refer to the state matrix and the input matrix, respectively, of the LTI state-space model, and P refers to the solution to the algebraic Riccati equation. The discrete-time Riccati equation is presented below [50]:

$$0 = A_D^T P A_D - P - (A_D^T P B_D)(B_D^T P B_D + R)^{-1}(B_D^T P A_D) + Q.$$

4.4 Frequency Weighted Linear Quadratic Regulator (FWLQR)

The FWLQR control strategy was inspired by an approach proposed in [35]. In this approach, the author of [35] endows the LQR concept with the ability "to include frequency-shaped weighting matrices in the quadratic cost functional" [35].

The primary motivation behind the introduction of notch filters in the Space Shuttle on-orbit DAP, and thus a more advanced CSI mitigation strategy, was to manage resultant loads and instabilities caused by the excitation of various frequencies created by dominant structural modes along the control loop feedback. The notch filter removes the pathological frequencies from the feedback signal, but does not actually change the system's response. The frequency weighting supplement to the LQR control methodology aims to actually modify the system's response in such a way that the pathological frequency components do not come into existence in the first place. The FWLQR control strategy supplements the LQR control strategy by adding the option to target specific frequencies, and to penalize controller outputs of that specific frequency. The FWLQR was chosen as a potential CSI mitigation strategy for its ability to explicitly optimize around targeted frequencies of concern.

Prior to the computation of the FWLQR optimal gain matrix K_{FWLQR}, a filter must be designed to isolate the frequencies of interest. Frequencies of interest are those that the designer would like the controller to penalize output activity in. This is similar in concept, but mathematically opposite to the notch filter approach. The notch filter for STS-71 (Figure 1 from [73]) penalized a range of frequencies, but targeted six frequencies specifically in which spectral activity would be attenuated. These frequencies can be found through the identification of the six identifiable notch filter peaks in Figure 1 of [73] [73]. To penalize spectral content at an identifiable frequency for FWLQR design, a band-pass filter (and not a notch filter) identifies the frequencies (or the frequency range(s)) that the controller should penalize activity in. The filter is modeled as a discretized LTI state-space system:

$$\hat{x}_{k+1} = A_f \hat{x}_k + B_f y_k$$
$$\hat{y} = C_f g_k + D_f y_k$$

The input to the filter's state space system is the output of the discretized state-space model of the translational (Case Study #1) or rotational (Case Study #2) PPE + solar array model (y_k). g_k represents the output that will have its spectral content penalized. In order to incorporate the filter's identification of frequencies for which which the spectral content is penalized, the LTI system for the plant model must be redefined:

$$\tilde{x}(k+1) = \begin{bmatrix} x(k+1) \\ \hat{x}(k+1) \end{bmatrix} = \tilde{A}_D \begin{bmatrix} x(k) \\ \hat{x}(k) \end{bmatrix} + \tilde{B}_D y_k$$

$$\hat{y}(k) = \tilde{C}_D \begin{bmatrix} x(k) \\ \hat{x}(k) \end{bmatrix} + \tilde{D}_D y_k$$

where

$$\tilde{A}_D = \begin{bmatrix} A_d & 0 \\ B_f C_d & A_f \end{bmatrix}$$
$$\tilde{B}_D = \begin{bmatrix} B_d \\ B_f D_d \end{bmatrix}$$
$$\tilde{C}_D = \begin{bmatrix} D_f C_d & C_f \end{bmatrix}$$
$$\tilde{D}_D = \begin{bmatrix} D_f D_d \end{bmatrix}$$

The re-definition of the LTI system above includes the creation of additional "states" that the user must specify weightings for in the Q and R weighting matrices. The Q matrix will be supplemented with an additional dimension that will allow the designer to choose how much the identified spectral content will be penalized, thus forming the $\tilde{Q}$ matrix. The R matrix for the FWLQR control methodology will be represented by $\tilde{R}$. The cost function for the FWLQR controller, modified to accommodate the augmented state-space system, is as follows:

$$J = \textstyle\sum_{k=0}^{\infty}[\tilde{x}(k)^T \tilde{Q} \tilde{x}(k) + u(k)^T \tilde{R} u(k)]$$

Similar to the LQR design process, the algebraic Riccati equation must be solved for to calculate the Riccati matrix, $\tilde{P}$. Then, the optimal gain matrix K_{FWLQR} can be found. This does not differ from the LQR design process introduced in Section 4.3, as the FWLQR abides by the same optimal full state feedback control law [44] [50]:

$$u(k) = -K_{FWLQR}\tilde{x}(k)$$
$$\text{where } K = (\tilde{B}^T \tilde{P} \tilde{B} + \tilde{R})^{-1}(\tilde{B}^T \tilde{P} \tilde{A}).$$

In the equation above, $\tilde{A}$ and $\tilde{B}$ refer to the state matrix and the input matrix of the newly defined LTI state-space system. The discrete-time Riccati equation, in which the value of P is calculated, is presented below [50]:

$$0 = \tilde{A}^T \tilde{P} \tilde{A} - \tilde{P} - (\tilde{A}^T \tilde{P} \tilde{B})(\tilde{B}^T \tilde{P} \tilde{B} + \tilde{R})^{-1} (\tilde{B}^T \tilde{P} \tilde{A}) + \tilde{Q}$$

The FWLQR control methodology builds off of the foundation provided by the LQR method. It offers a more direct way of attenuating various frequencies of interest in a structural dynamics simulation, which explicitly addresses the control objective in which this thesis is framed.

4.5 Model Predictive Control (MPC)

The following three resources were the primary papers that portrayed the theory and guided the adaptation of MPC into the application evaluated in this thesis: [38] [39] [33].

The fundamental capability that MPC offers beyond those of the phase plane, PID, LQR, and FWLQR control methodologies is the ability to optimize control inputs with respect to input and output constraints. Additionally, MPC is the only control methodology in the series presented within this thesis that can consider and optimize for semi-continuous variable inputs (as described in Section 2.2). MPC is also able to consider actuator inputs of a continuous (CMG/RW) or a binary (RCS) nature.

For the binary input variable case, as with the phase plane controller, the MPC methodology can prescribe the force/torque of the thruster in the "on" configuration. For semi-continuous variable inputs, the MPC methodology can set the minimum and maximum thrust/torque values, therefore setting the range of continuously-variable inputs that the controller can generate (otherwise, the control input is 0). Finally, for continuous variable inputs, the MPC methodology can set the maximum thrust/torque values at which the actuator can apply an input up to from a 0 minimum value. Input constraints are different than output constraints, in that they are "hard" constraints. The MPC methodology does not violate input constraints, which is desirable as thrust/torque ranges cannot often be exceeded due to performance limitations on the specific actuator types. Although it would be desirable to enforce "hard" output constraints for the MPC methodology, it is impossible to guarantee their satisfaction. MPC has the ability to apply "soft" constraints, whereby an excursion beyond the constraint is tolerated, but discouraged by means of a penalty, or cost, on the excursion $z(k)$.

In MPC, similar to the LQR and the FWLQR design methodologies, the control objective is formulated as an optimization problem in which to minimize the value of a cost-function. The cost function is similar to that of the FWLQR methodology, but accommodates the influence of output constraints on the generated control action ($z(k)$ and S). Additionally, the cost function, as it is presented here, does not consider the tilde variations (i.e., considering frequency-weighting) of the variables used in the FWLQR methodology. However, MPC is capable of employing the frequency-weighting capabilities introduced in Section 4.4. For simplicity of presentation, the notation used within the LQR theory development in Section 4.3 is used as a launching point for the MPC theory development:

$$J = \textstyle\sum_{k=0}^{n-1}[x(k)^T Q x(k) + u(k)^T R u(k) + z(k)^T S z(k)]$$

The variable $z(k)$ represents the difference between the user-specified minimum and maximum output constraints of the controller output as a function of time. Exceeding a specified minimum and maximum will result in certain repercussions on the cost function, so as to generate control action sufficient to counteract the constrained outputs. The magnitude of the cost function's penalization when exceeding the output constraints depends on the weighting matrix S. Like Q and R for the LQR methodology, the relative weight of S over the other weighting variables will cause the controller to penalize deviations from the minimum and maximum output parameters more or less.

This qualitative overview of $z(k)$ is mathematically represented in the following set of statements:

$$z_i(k) = \begin{cases} y_i(k) - \hat{y} \text{ if } y_i(k) > \hat{y} \\ -y_i(k) + \hat{y} \text{ if } y_i(k) < \hat{y} \\ 0 \text{ if otherwise} \end{cases}$$

As discussed, $x(k)$ and $u(k)$ remain primarily untouched from the LQR cost function. However, with MPC's inherent ability to consider additional variable types beyond the continuous cases (semi-continuous and binary), comes a slight re-definition of $u(k)$.

The cost function presented earlier was that of an infinite-horizon optimal control problem. However, the MPC control methodology implemented in the simulation space is a finite-horizon optimal control problem, because solving accommodating constraints over an infinite time-horizon is generally computationally intractable. In order to present the finite-horizon version of the MPC cost function, an understanding of the "prediction horizon" (N) is necessary. The prediction horizon is unique to finite-horizon optimal control problems, and represents "the number of future control intervals [that] the MPC controller must evaluate by prediction when optimizing at each control interval k" [49].

$$\hat{J} = \textstyle\sum_{k=0}^{N-1} [x(k)^T Q x(k) + u(k)^T R u(k) + z(k)^T S z(k)] + x(N)^T V x(N).$$

The terminal cost V is introduced as a weighting variable unique to the finite-horizon problem. It, like Q, R, and S is a design parameter, and penalizes the variable $x(N)$. It is the state at the end of the prediction horizon, also known as the terminal state. Prediction horizons are unique to the MPC methodology, relative to the other candidate CSI mitigation strategies. They allow the controller to make preemptive control decisions taking into consideration information about the future that is either known or predicted (e.g., planned setpoint changes, or predicted fluctuations in parameters).

Chapter 5

Simulation Results

The following chapter is dedicated to the presentation and evaluation of simulations in which the PPE conducts a 1.5 meter translation (Case Study 1) and a 180 degree rotation (Case Study 2). Each CSI mitigation strategy is evaluated in separate simulations of the PPE conducting its translational or rotational maneuver. The overall objective is to compare and contrast each CSI mitigation strategy against the other, in regards to its ability to accomplish the following two objectives (as introduced in Chapter 2):

1. **Primary Objective**: Enable the PPE's completion of the 1.5 meter translation in one dimension (Case Study 1) or the 180 degree rotation about one axis (Case Study 2).

2. **Secondary Objective**: Minimize the amplitude and the spectral content of the displacement of the solar array relative to the PPE.

5.1 Case Study 1: Translation

As reviewed in Chapter 2, the PPE has two actuation sources that are capable of producing propulsive inputs: the RCS system and the SEP system. These are the only two actuation sources that are capable of being employed in Case Study #1.

5.1.1 Phase Plane Controller

The phase plane controller was chosen as a candidate CSI mitigation strategy for its use in the Space Shuttle era. A more in-depth review of this control system and its heritage is provided in Section 4.1. This controller made use of the Shuttle's RCS binary "on-off" jets to perform attitude control, and included a notch filter on the feedback channel (see Figure 2 on page 64 of [63]). A one-dimensional replica of this controller was recreated, and made use of the PPE's RCS jets to conduct a translational maneuver 1.5 meters forward in one-dimensional space. Figure 5-1 includes the displacement of the PPE, the displacement of the solar array relative to the PPE, and the firing sequence of two RCS jets as the controller accomplishes the primary control objective.

The output of a phase plane controller was visualized through a phase plane portrait during the Shuttle era, and was presented as such in Section 4.1. Examples of a phase plane portrait were provided in Figure 9 of [73] and Figure 3.3 of [72]. Using this visualization tool as a template, a phase plane portrait of the PPE's error and error rate from the simulation presented in Figure 5-1 is included in Figure 5-2.

Immediately upon receiving the 1.5-meter translation command, the phase plane controller recognizes an error, and begins firing the +106 N RCS thruster in the positive direction. This continues until the error decreases to approximately 1.1 meters, and the error rate is approximately -1 m/s. At this time, the PPE's error versus error rate combination crosses the diagonal switching line, and the +106 N thruster is turned off and replaced with the -106 N force from a thruster facing in the opposite direction. Rapid firings ensue between the -106 N and the +106 N thruster as the error and error rate are slowly decreased. The parallelogram formed by the intersection of the four switching lines is the deadband; a space where no thrusters are fired. The spacecraft's error and error rate relative to its commanded trajectory is maintained in this zone. When any of the switching lines are crossed, the appropriate thruster fires, thus bringing the PPE back into a drift.

The translation and stabilization of the PPE under phase plane control is only

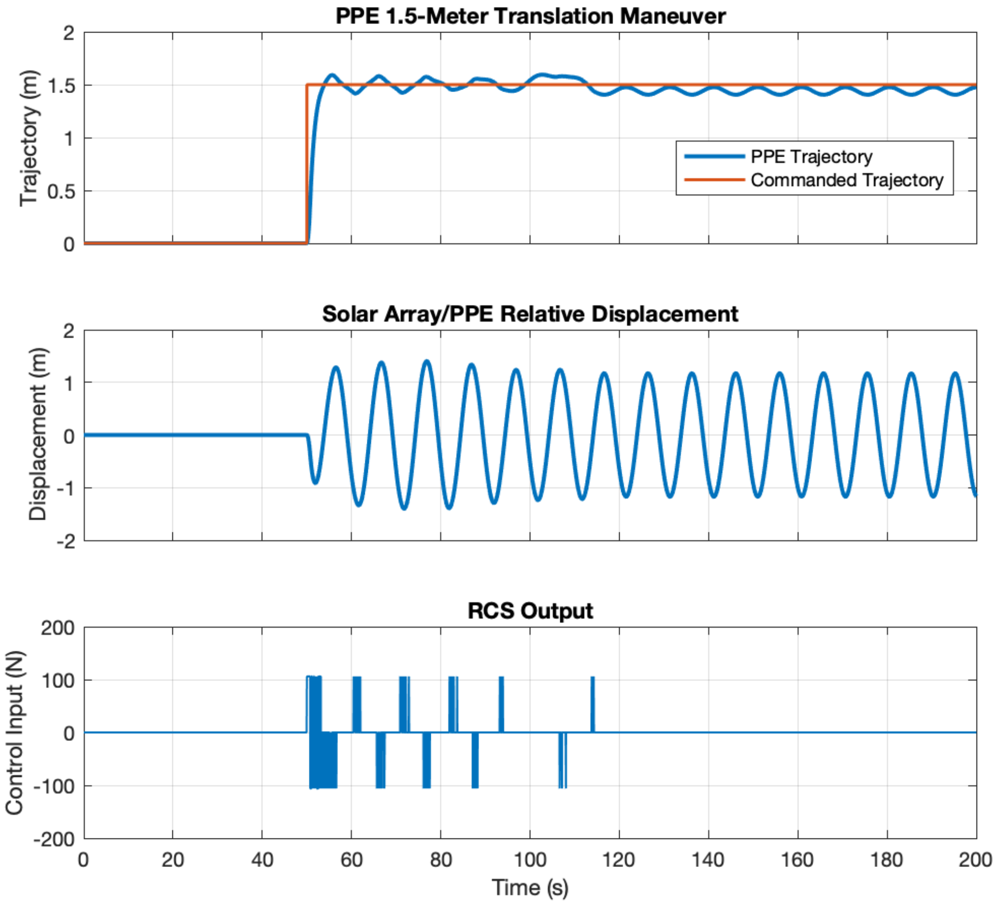

Figure 5-1: Case Study 1 (Phase Plane): PPE Trajectory, Solar Array/PPE Relative Displacement, and RCS Control Input Plots

made possible through the application of the notch filters on the feedback channel. Without notch filters, the system is unstable, and upon receiving the 1.5-meter translation command, oscillates out of control. Figure 5-3 illustrates this destabilization.

The natural frequency of the solar array for Case Study #1 is approximately 0.1 Hz (as chosen in Section 3.1.1), and excessive activity at this frequency within the error of the feedback is causing the instabilities seen in Figure 5-3. Figure 5-4 demonstrates how a reduction in the spectral content at this very active frequency stabilizes the system (as seen in Figure 5-1).

The PPE, under a phase plane control system, accomplished the primary control objective of translating the PPE forward in space by 1.5 meters. Additionally,

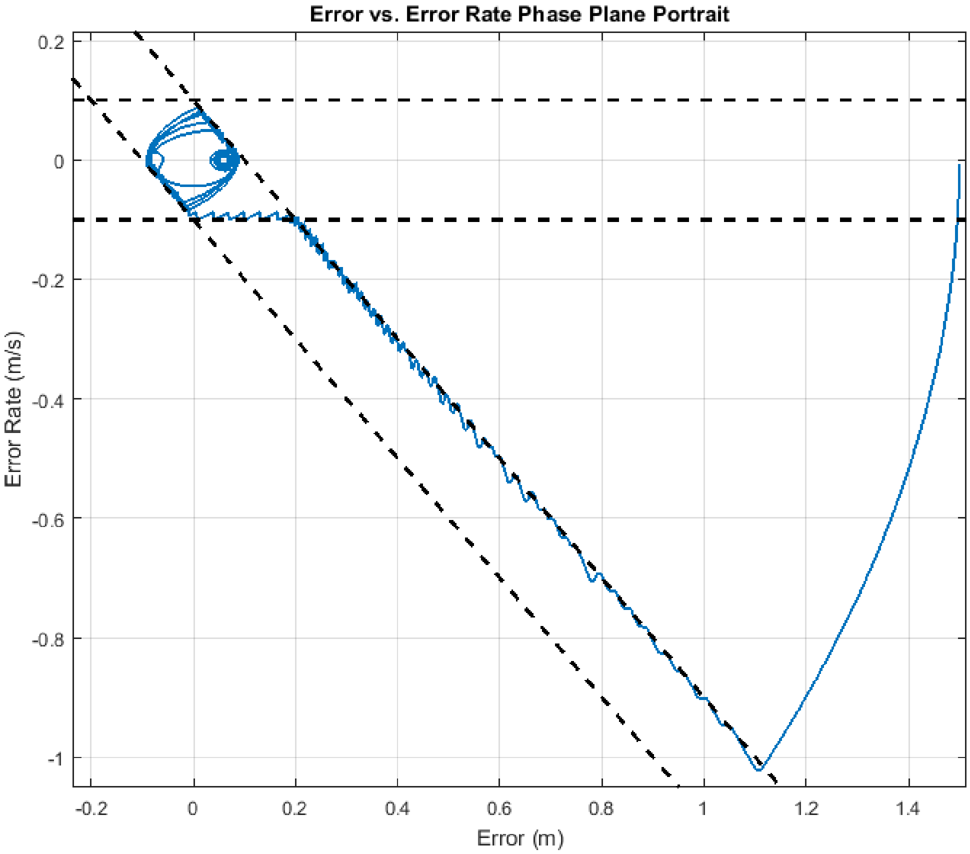

Figure 5-2: Case Study 1 (Phase Plane) Portrait

the value of the notch filter, as employed by Space Shuttle GNC engineers for the Shuttle's on-orbit DAP, was demonstrated in stabilizing what would have been an unstable system. The notch filter dramatically reduced the solar array/PPE relative displacement, as depicted in Figure 5-4. As seen in Figure 5-1, the amplitude of the relative displacement decreases over time as the notch filter mitigates activity at the solar array's natural frequency. The phase plane controller accomplished the primary objective, and also demonstrated its ability to accomplish the second objective: it reduced the amplitude of the displacement of the solar array relative to the PPE. There is also room for improvement. The notch filters that are responsible for mitigating this activity can be more effectively tuned in to the targeted frequency and can provide an even sharper reduction in spectral activity, thus introducing the possibility of greater reductions in relative displacement oscillations for the phase plane control

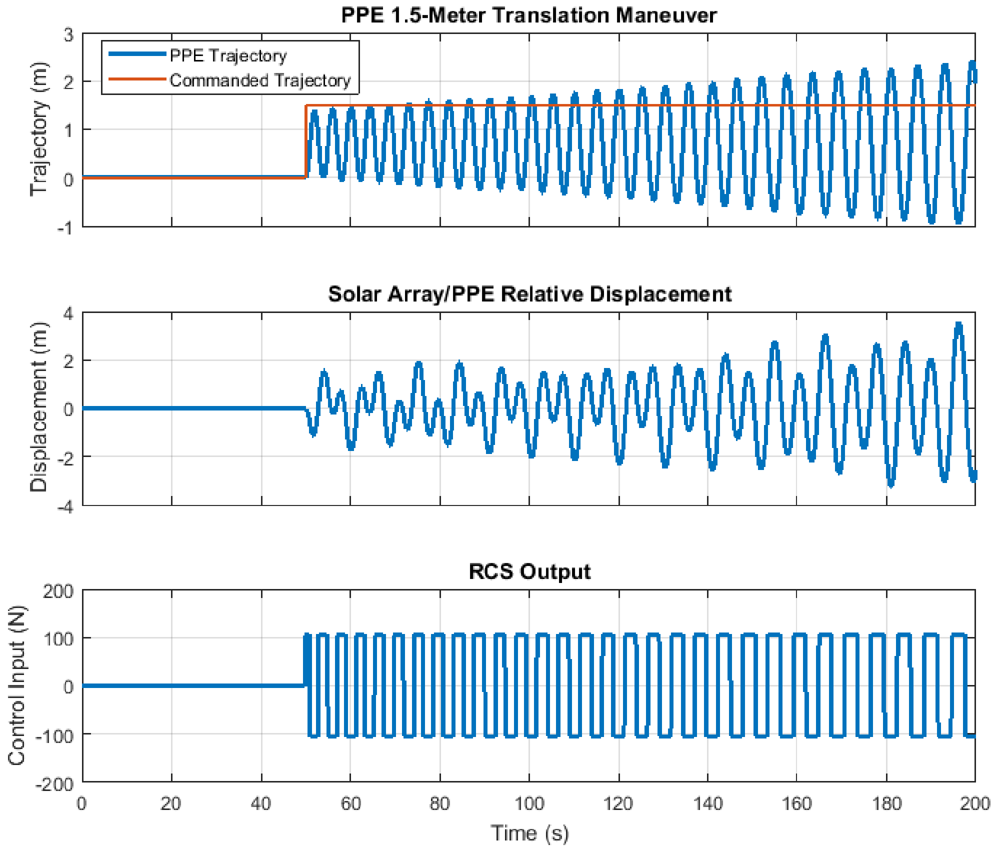

Figure 5-3: Case Study 1 (Phase Plane): PPE Trajectory, Solar Array/PPE Relative Displacement, and Control Input Plots without Notch Filters

methodology.

One potential issue with the phase plane controller is the rapidity at which it demands the RCS jets to fire. Although the rate at which the jets fire can be decreased with more precise notch filtering, this may be a cause for concern in regards to implementation on a real-world system. Excessive toggling may overburden the mechanical infrastructure in place for managing and implementing the RCS. Another issue is the magnitude at which the solar arrays oscillate relative to the PPE. Although fine-tuning the notch filter could yield better results in this field, the oscillations still tend to have amplitudes on the order of meters. Solar arrays displacing back and forth on this order of distance from their fixed hinges on the PPE may cause critical structural stresses. It is notable to say that the phase plane controller does not fire after 200

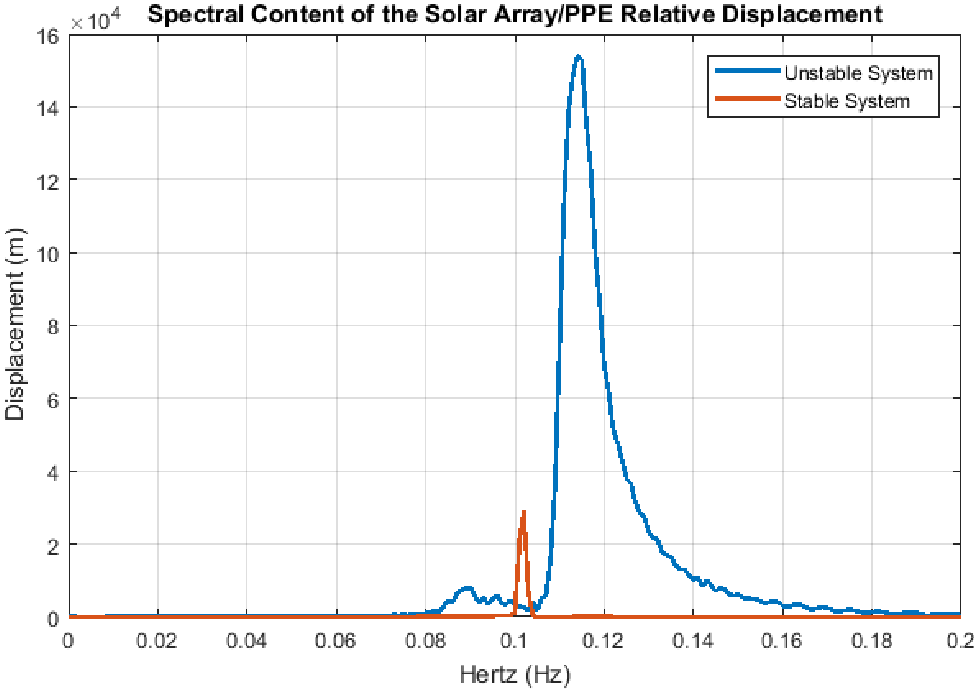

Figure 5-4: Case Study 1 (Phase Plane): Spectral DFT Content of the Solar Array/PPE Relative Displacement

seconds, as the PPE is in the appropriate drift zone from 200 seconds on, and remains there for the remainder of the simulation. Despite the "on-off" high toggling rate in the initial 200 seconds, the phase plane controller is noticeable for its lack of fuel consumption after 200 seconds.

5.1.2 PID

The PID was chosen as a candidate CSI mitigation strategy for its widespread use in engineering systems. A more in-depth review of this control method is available in Section 4.2. As a SISO-configured controller in the context of this thesis, the state-space output matrix is provided as: $C = \begin{bmatrix} 1 & 0 & 0 & 0 \end{bmatrix}$. This resembles the fact that the primary control objective relates to the position of the PPE module. Section 3.1.1 elaborates upon the breakdown of the state vector, $x(k)$. The PID control system's resultant control action is comprised of three different terms: a proportional control action u_P, an integral control action u_I, and a derivative control action u_D [75]. The resultant control action is a continuous signal: at each time-step, the control action can take on the form of any real number. This differs from the phase plane's control input binary variable type.

There are a variety of tuning methods available when it comes to deciding upon the individual proportional, integral, and derivative control action gains for each PID controller. Unlike the LQR, FWLQR, and MPC methodologies, PID controllers do not optimize the control gain directly through the solution of the Riccati equation and the various weighting matrices. When done by hand, PID controllers require deliberate tuning of each control action's gain, which is not inherent to the controller design as it is for the aforementioned optimal control methods. No such tuning process was used in the simulation and testing of the PID controller. A trial-and-error approach was used by the author in finding a set of control gains that would provide a stable and well-performing (in the context of the primary and secondary control objectives) result.

PID controllers produce continuous controller outputs, which does not meet the specific actuator variable type for the binary RCS or the semi-continuous SEP system. Therefore, in an effort to provide the PID with a template to be tested in, additional logic will be incorporated into the PID control loop. Controller commands generated by the controller will be limited if they go beyond the SEP upper and lower thrust limits of 0.520 N and 0.301 N, respectively. It is important to note that this will inhibit the performance of the PID control system. The controller will still recognize the error and generate a control action under the assumption that said control action could be any real number (which may exceed the imposed SEP thruster bounds). At every time step, however, this control action is run through an additional limiting function, thus forcing the PID control method to not be used as originally intended.

A PID controller was created to maneuver and stabilize the PPE 1.5 meters from its point of origin. Individual control action gains were decided upon through extensive experimentation. It was difficult for the author to find a set of individual control action gains that would lead to stable, let alone a well-performing output, given the semi-continuous limiting function that was placed in the PID control loop. Once a stable solution was found, the author did not make many additional efforts to fine-tune performance because of the performance degradations caused by the semi-continuous limiting function. Although the author recognizes that no optimal solution can be claimed because of the lack of any specific tuning method, the gains that were decided upon led to a stable system that accomplished the primary control objective: $k_P = 10$, $k_I = 0.1$, and $k_D = 2000$.

Figure 5-5 includes the displacement of the PPE, the displacement of the solar array relative to the PPE, and the firing sequence of two RCS jets as the controller accomplishes the primary control objective under the PID controller.

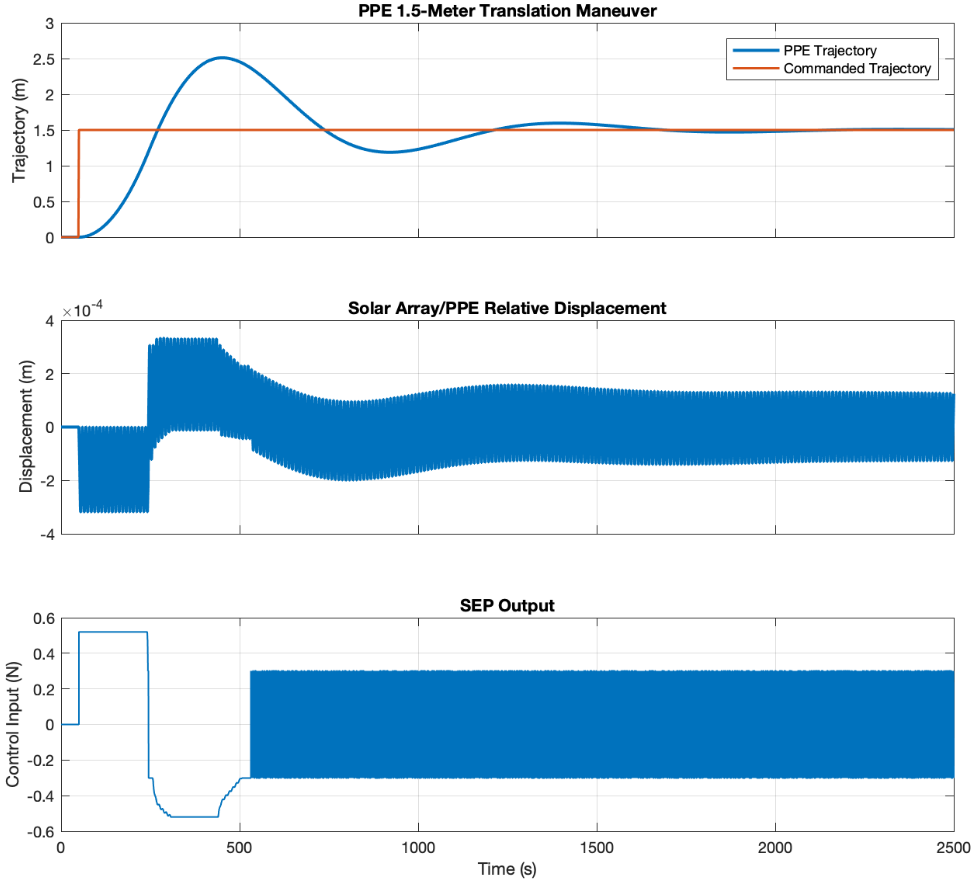

Figure 5-5: Case Study 1 (PID): Control Objective and Control Input Simulation Output

Approximately 500 seconds into the simulation, the SEP engine begins to rapidly fire between +/- 0.302 N for the remainder of the simulation in an attempt to settle the

PPE at its target displacement. Compared to the results of the phase plane controller, the PPE has a much larger settling time and a much larger percent overshoot, but has a much smaller solar array/PPE relative displacement (four orders of magnitude less than that of the phase plane simulations; see Figure 5-1). This is most likely associated with the longer settling time and percent overshoot that the PID controller enables for the PPE module's trajectory. Under this specific control design, the PPE does not adequately settle at its target until approximately 1500 seconds after the simulation begins. This is significantly larger than the approximate 10-20 second settling time enabled by the phase plane controller.

The solar array is oscillating at 0.1 Hz for the majority of the simulation timeframe, as demonstrated in Figure 5-6.

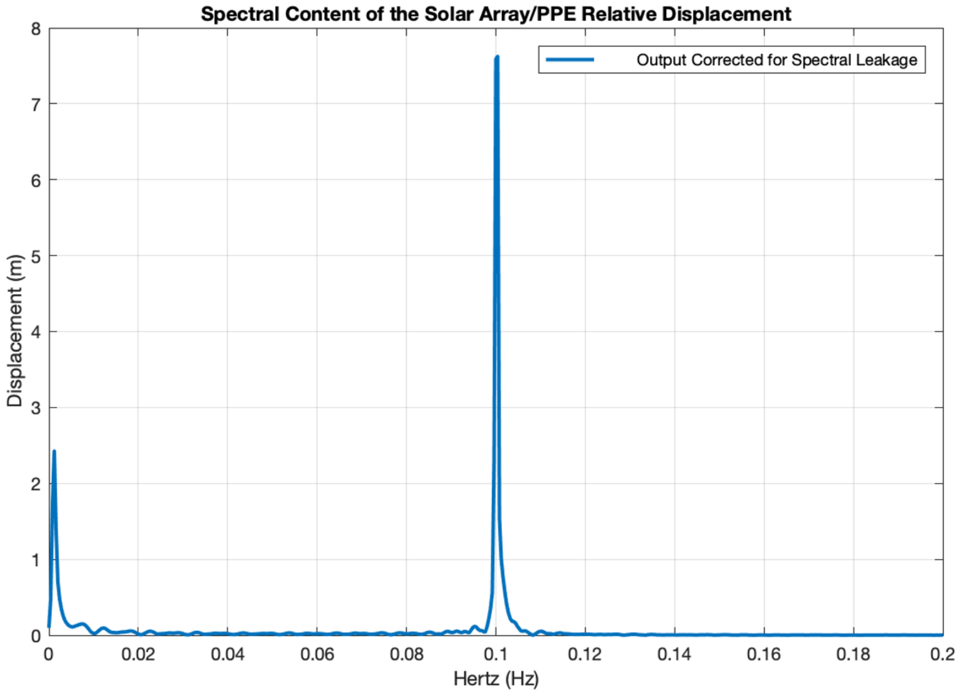

Figure 5-6: Case Study 1 (PID): Spectral Simulation Output

Due to the decreased amplitude of the oscillations, the spectral content at 0.1 Hz is four orders of magnitude less than that of the solar array in the phase plane simulation. With this decrease in activity at 0.1 Hz, it becomes more readily apparent that oscillatory activity exists at other areas of the frequency spectrum. For example, there is a second peak at a frequency slightly higher than 0 Hz. Activity existed at around this region for the phase plane simulation as well (Figure 5-4). Activity at this area of the frequency spectrum is primarily associated with the displacement of the solar array relative to the PPE in the initial elements of the simulation; in the first 500 seconds of the simulation in which the PPE is going through its highest velocity and acceleration changes in its translation profile, it is oscillating at a lower frequency.

The PPE accomplished its primary control objective under a PID controller, albeit a lot slower than it did in the phase plane simulation profile. The PID controller also caused a much higher percent overshoot, and a much longer rise and settling time than the phase plane controller did. Ultimately, this resulted in a smaller relative displacement amplitude, which correlated to less frequency content at the 0.1 Hz value compared to the phase plane controller under the influence of the notch filters. The SEP, shortly after approximately 500 seconds, began a rapid firing sequence between +/- 0.302 N, the established minimums of the SEP thruster output capability. This rapid firing may strain the mechanical infrastructure of the SEP, as it may also do for the rapid firing of the RCS in the phase plane simulations.

5.1.3 LQR

The LQR method is the first optimal control method considered in the list of candidate control methodologies. The method implements a cost function that considers the relative user-specified weights between the state vector (Q) and the input vector (R) [45]. A higher relative weighting on the state cost Q makes tolerating an error more expensive than implementing control inputs. This leads to more liberal control inputs in the LQR's attempt to accomplish the control objectives. If a higher weighting is placed on the input cost R, it becomes more "expensive" to implement control inputs. This leads to a more conservative application of control inputs as the LQR attempts to generate the control actions needed to complete the control objectives. A more in-depth review of this control methodology is provided in chapter 4.3. The LQR control strategy, although capable of multi-objective control, will be constrained to single objective control. This is to help in slowly progressing the capabilities of the control strategies presented in this thesis, and to more effectively compare and contrast the capabilities of the LQR control methodology to the phase plane and the PID controllers. Exactly like the PID controller, the state-space output matrix is: $C = \begin{bmatrix} 1 & 0 & 0 & 0 \end{bmatrix}$.

It is important to note that the LQR methodology is unable to directly penalize the displacement of the solar array relative to the PPE, given the configuration of the LQR control methodology used in this thesis. However, the LQR control methodology is easily extendable to accommodate multi-objective control. It is, in this configuration, able to make tolerating errors for specific states more expensive than implementing control inputs (which is the emphasis of the LQR controller as presented in this thesis). This provides an increase in capability compared to the PID and phase plane controllers, specifically relating to the second control objective (limiting dynamic outputs for the displacement of the solar array relative to the PPE), but does not address it directly.

As it was mentioned, the relative values of Q and R can enable a greater emphasis on the performance of one state or one control objective versus another (as discussed in chapter 4.3). For example, by setting the Q and R matrices as:

$$Q = \begin{bmatrix} 10 & 0 & 0 & 0 \\ 0 & 1 & 0 & 0 \\ 0 & 0 & 1 & 0 \\ 0 & 0 & 0 & 1 \end{bmatrix}$$

$$R = 1$$

the cost function is being set up so that tolerating an error from the PPE's designated trajectory is more expensive than a control input, leading to the expenditure of additional controller inputs to complete the translation maneuver, ideally, more expeditiously. Using these values for Q and R result in the simulation outputs portrayed in Figure 5-7 regarding the PPE's 1.5-meter translation maneuver:

The LQR control methodology, with this specific Q and R setup, is able to accomplish the primary control objective approximately 500 seconds into the simulation,

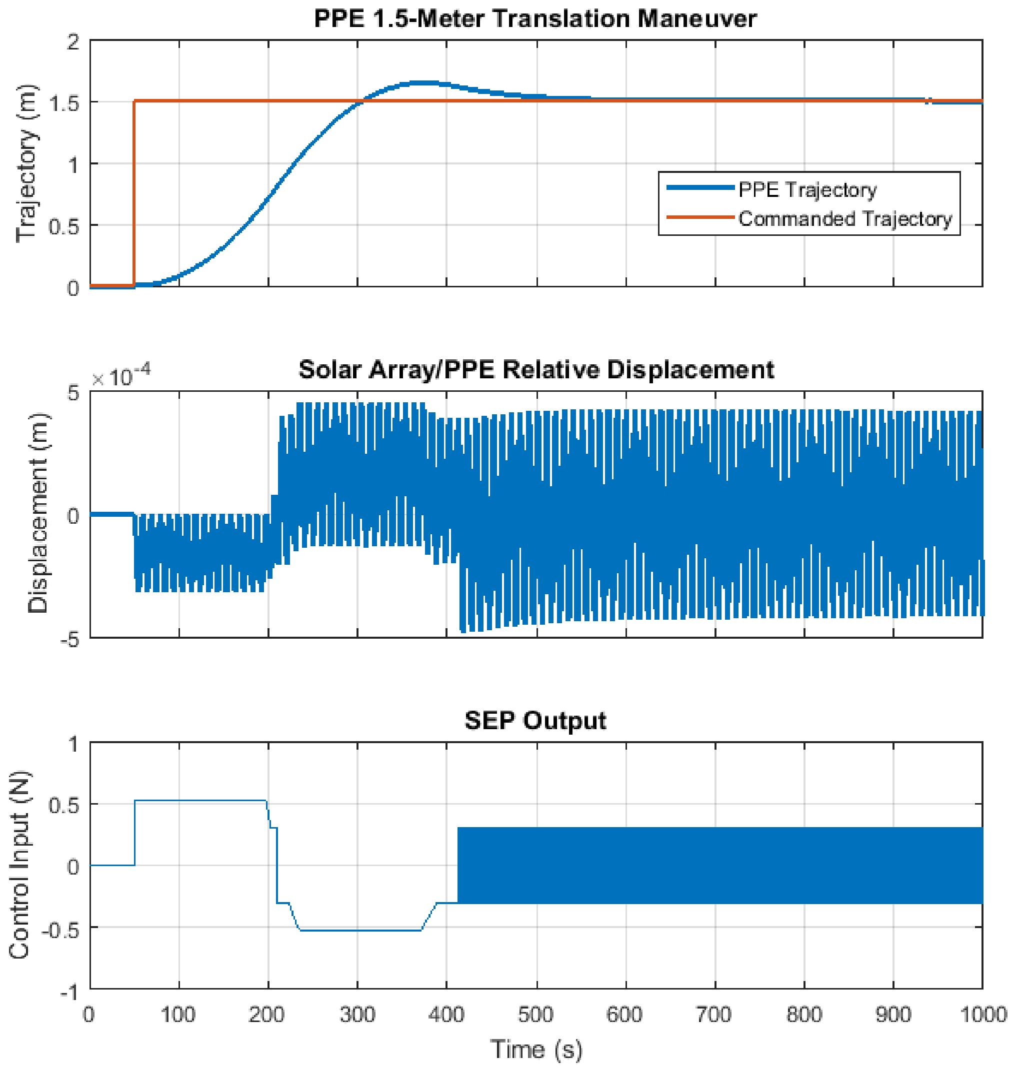

Figure 5-7: Case Study 1 (LQR): Control Objective and Control Input Simulation Output for Scenario #1

which is more timely than the PID controller by approximately 1000 seconds. Additionally, the relative displacement is on the order of 10^{-4} m, similar to the PID.

Although the secondary control objective is not explicitly programmed into the LQR framework, additional weighting can be placed on the third state, which is the position of the solar arrays. In the LQR logic, the solar array position is also individually commanded to a value of 1.5 meters, despite the thrusters only being located on the PPE module. By increasing the weight on the Q matrix for the third state, the error between the commanded 1.5-meter trajectory and the actual solar array position will be more heavily penalized, which effectively penalizes the relative displacement of the solar array/PPE. The following Q and R matrices are used to evaluate the LQR's ability to minimize this relative displacement:

$$Q = \begin{bmatrix} 100 & 0 & 0 & 0 \\ 0 & 1 & 0 & 0 \\ 0 & 0 & 10 & 0 \\ 0 & 0 & 0 & 1 \end{bmatrix}$$

$$R = 1$$

the cost function will penalize errors for the PPE and the solar array in a fashion consistent with the primary and secondary control objectives that were established in the introduction of Chapter 5. The simulation output for this setup (Scenario #2) is provided in Figure 5-8.

Scenario #2 effectively reduces the solar array/PPE relative displacement in amplitude from $t = 250$ seconds and onwards, compared to the results from Scenario #1. Additionally, at around $t = 600$ seconds, the relative displacement is further reduced in amplitude as the PPE arrives at a steady-state condition at 1.5 meters ahead of its origin. However, the PPE does not settle in a shorter amount of time, compared to the results in Scenario #1. There is a substantial increase in the overshoot that the PPE experiences in Scenario #2 compared to Scenario #1, despite the 1.5-meter threshold being crossed in a shorter amount of time.

The primary reason is a similar reason to the PID controller, in that the LQR control method generates a continuous control input signal. Similarly to the PID controller, a limiting function had to be placed within the control feedback loop: any control input signal that was less than 0.301 N but greater than 0 N was limited to 0.301 N. Similarly, any control input signal that was greater than 0.520 N was reduced to this force value. By forcing a control methodology that computes an optimal continuous signal to produce a sub-optimal semi-continuous input signal has a noticeable impact on performance, and provides a sub-optimal solution. To illustrate

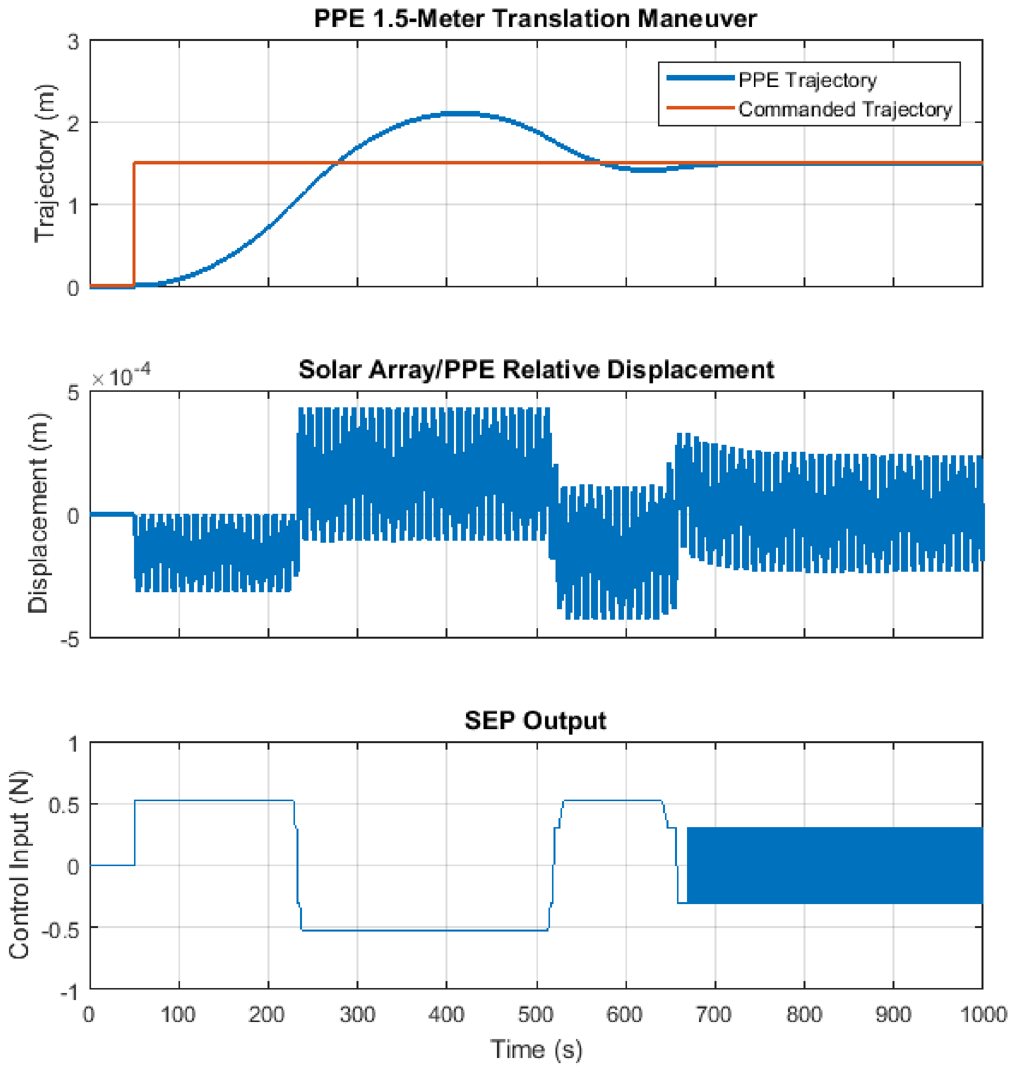

Figure 5-8: Case Study 1 (LQR): Control Objective and Control Input Simulation Output for Scenario #2

this point, Figure 5-9 shows the simulation output for Scenario #2 without the semi-continuous limiting function.

Despite the performance pitfalls of the semi-continuous limiting function, the LQR's ability to more effectively manage the relative displacement is noted in Scenario #2's output figure (Figure 5-8). Relative to Figure 5-7, the amplitude of displacement is not only smaller than its Scenario #1 counterpart after the $t = 250$ second mark, but is further reduced at around $t = 600$ seconds. Comparing the two spectral

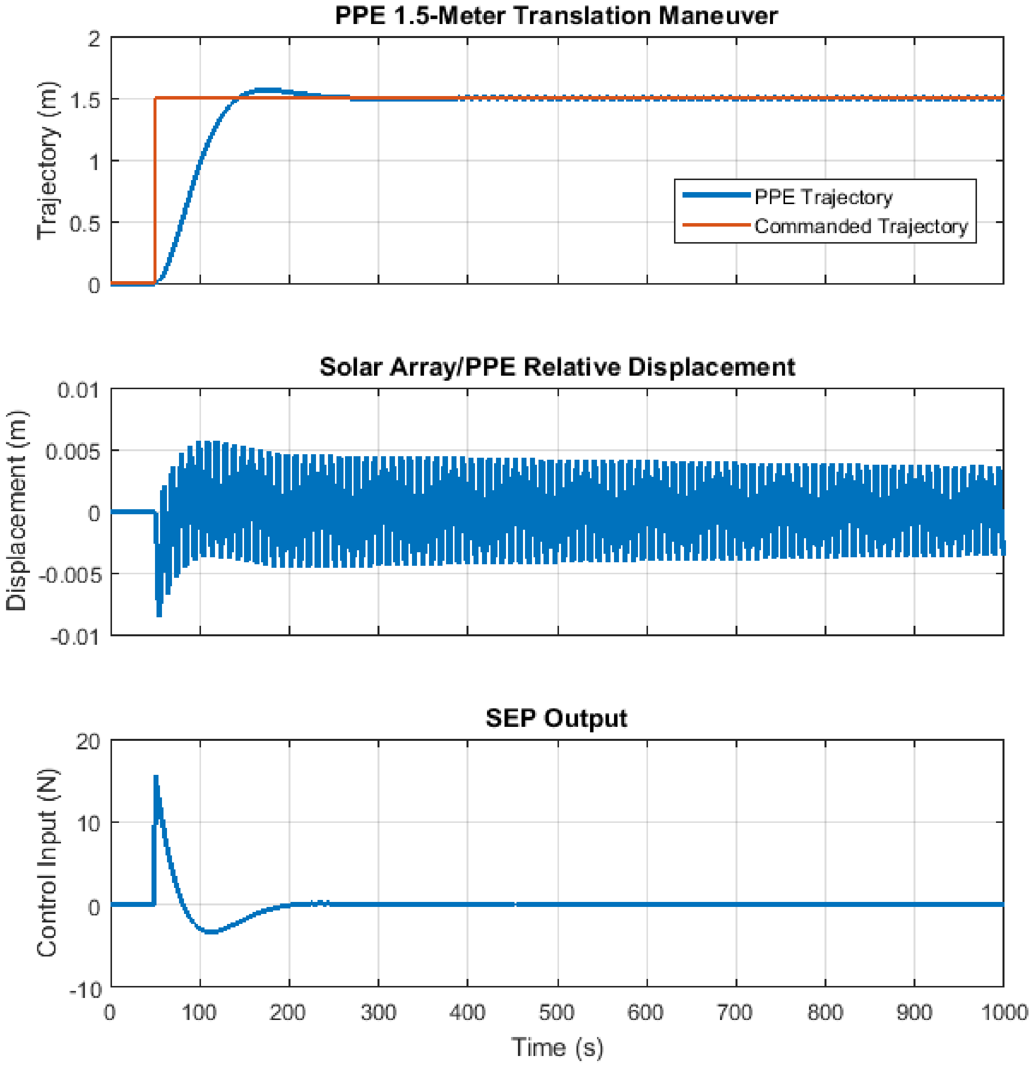

Figure 5-9: Case Study 1 (LQR): Control Objective and Control Input Simulation Output for Scenario #2 Without the Semi-Continuous Limiting Function

content outputs for the solar array/PPE relative displacements of Scenario #1 and Scenario #2 show that the new Q and R matrix assignments led to a decrease in spectral content at 0.1 Hz (Figure 5-10).

The spectral content of Scenario #2 at 0.1 Hz is the smallest that it has been for any simulation under the influence of any other control methodology at this point in the comparative analysis process. However, Scenario #2 still saw a slight increase in settling time, and a noticeable increase in the percent overshoot of the PPE as

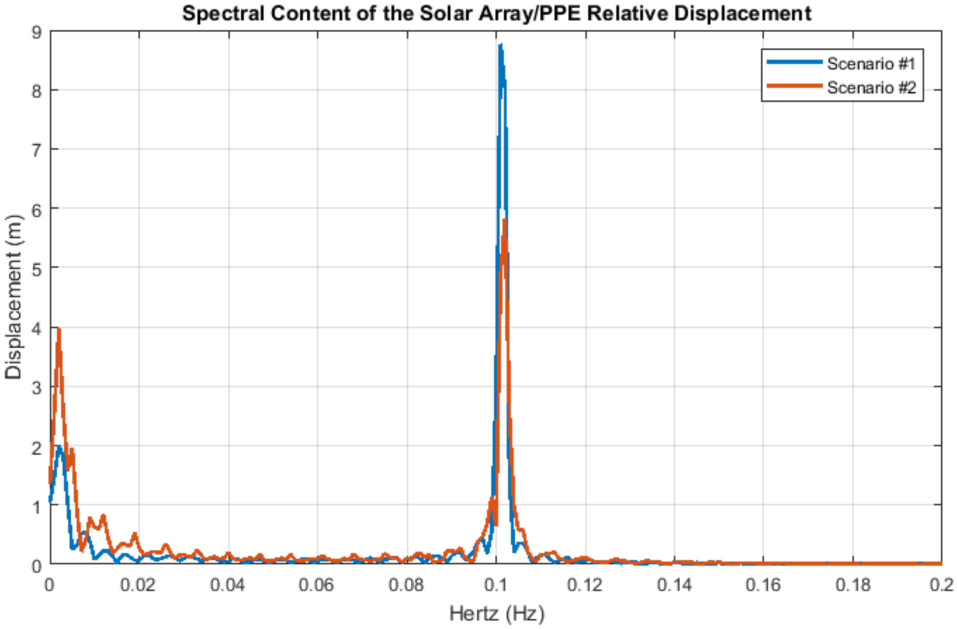

Figure 5-10: Case Study 1 (LQR): Spectral Simulation Output Comparison between Scenario #1 and #2

it attempted to settle at the 1.5-meter commanded trajectory. The phase plane controller still, at this point, has the fastest settling time (Figure 5-1), but does have a spectral content peak four orders of magnitude higher than those in the PID and LQR simulation outputs. However, the largest performance degradation is the semi-continuous limiting function, which penalizes both the PID and LQR controllers significantly. It is interesting to note that, when comparing Figures 5-8 and 5-9, the amplitude of the relative displacement output is smaller for Scenario #2 with the semi-continuous limiting function, as compared to the amplitude for Scenario #2 without the limiting function. Although the controller's ability to accomplish the primary control objective is inhibited by the forcing function, it seems as if maintaining this function reduces the spectral content at 0.1 Hz (Figure 5-11).

In terms of joint performance, the LQR controller is potentially the most advantageous CSI mitigation strategy up to this point in the thesis, primarily because of its ability to settle the PPE in a relatively small amount of time at its target and in its ability to combine a mitigated spectral content at the frequency in question for the relative displacement secondary control objective. Despite effectively accomplishing

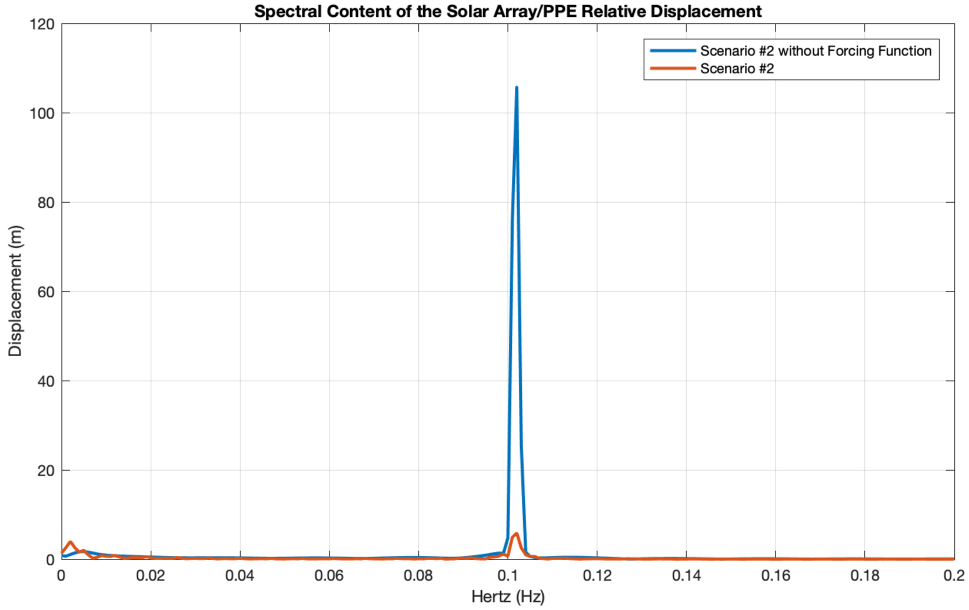

Figure 5-11: Case Study 1 (LQR): Spectral Simulation Output Comparison between Scenario #1 and #2

the primary and secondary control objectives, the LQR methodology is limited in its ability to optimize specifically towards the completion of a control objective that is not denoted by the performance of one state, such as the primary control objective moving the PPE forward in space by 1.5 meters (as it is used in this thesis). However, the LQR methodology is extendable to accommodate multi-objective control, and is an area for future work. It can be assumed that the LQR controller could perform better with a multi-objective controller setting. The next control methodology, FWLQR, offers the increased advantage of targeting the spectral content of an output, and allows the user to provide weighting variables to tune the penalization of the spectral content much like the user can for any state in the LQR controller methodology.

5.1.4 FWLQR

The FWLQR, which is introduced in Section 4.4, supplements the capabilities provided by the LQR by adding the ability to penalize specific frequencies from a specific control output. This output can be specified as a linear combination of states and inputs, just like in LQR (although LQR was only applied in this thesis with respect to a single control objective). To specify the targeted frequencies, a band pass filter is designed with a center frequency equal to the frequency that the user would like to penalize spectral content at. In the case of this thesis, the targeted frequency is 0.1 Hz, as illustrated by the band-pass filter displayed in Figure 5-12.

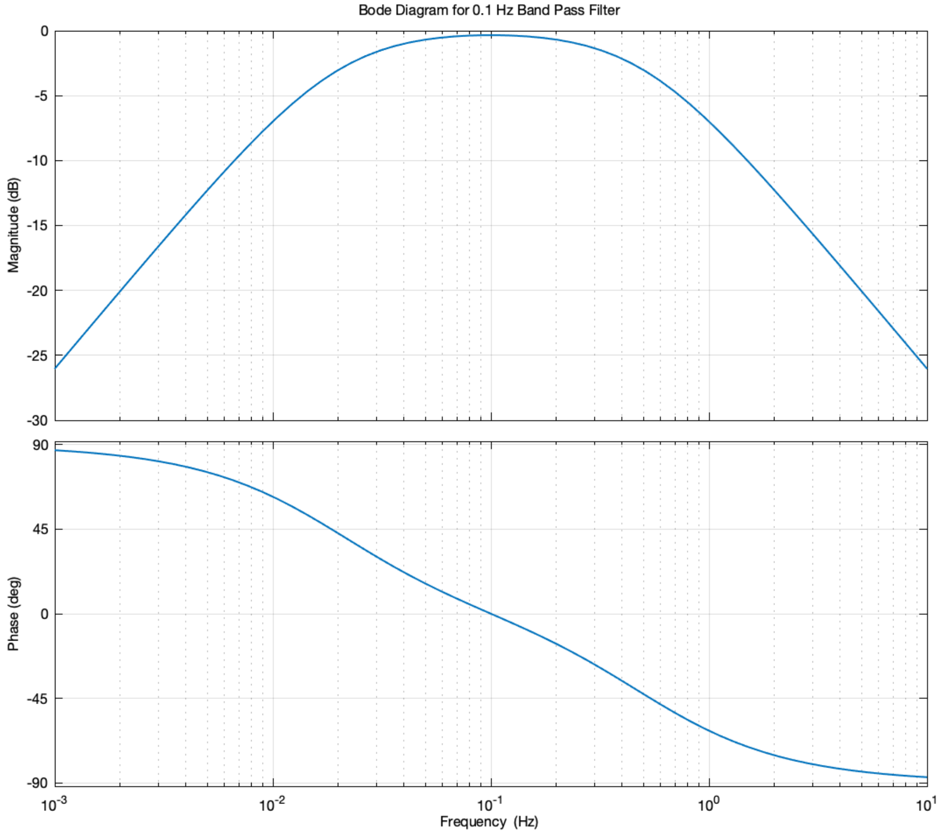

Figure 5-12: Case Study 1 (FWLQR): Band Pass Filter Centered at 0.1 Hz

The user, through a modified Q matrix ($\tilde{Q}$), is then able to make tolerating an error in the control objective's spectral content more expensive than the control inputs needed to accomplish that control objective ($\tilde{R}$). Additionally, the $\tilde{Q}$ matrix also allows relative weighting on another control objective to exceed that of the spectral content weighting.

The Q matrix is modified to reflect the relative weightings of the control objectives, and not the relative weightings of the states. This new Q_{Output} term encompasses the control objective of $C = \begin{bmatrix} 1 & 0 & 0 & 0 \end{bmatrix}$, and the spectral content of the solar array/PPE relative displacement.

The first scenario will include the following Q_{Output} and R matrix weightings:

$$Q_{Output} = \begin{bmatrix} 10 & 0 \\ 0 & 1 \end{bmatrix}$$
$$R = 1$$

Using these values for Q and R result in the following simulation outputs regarding the PPE's 1.5-meter translation maneuver (Figure 5-13).

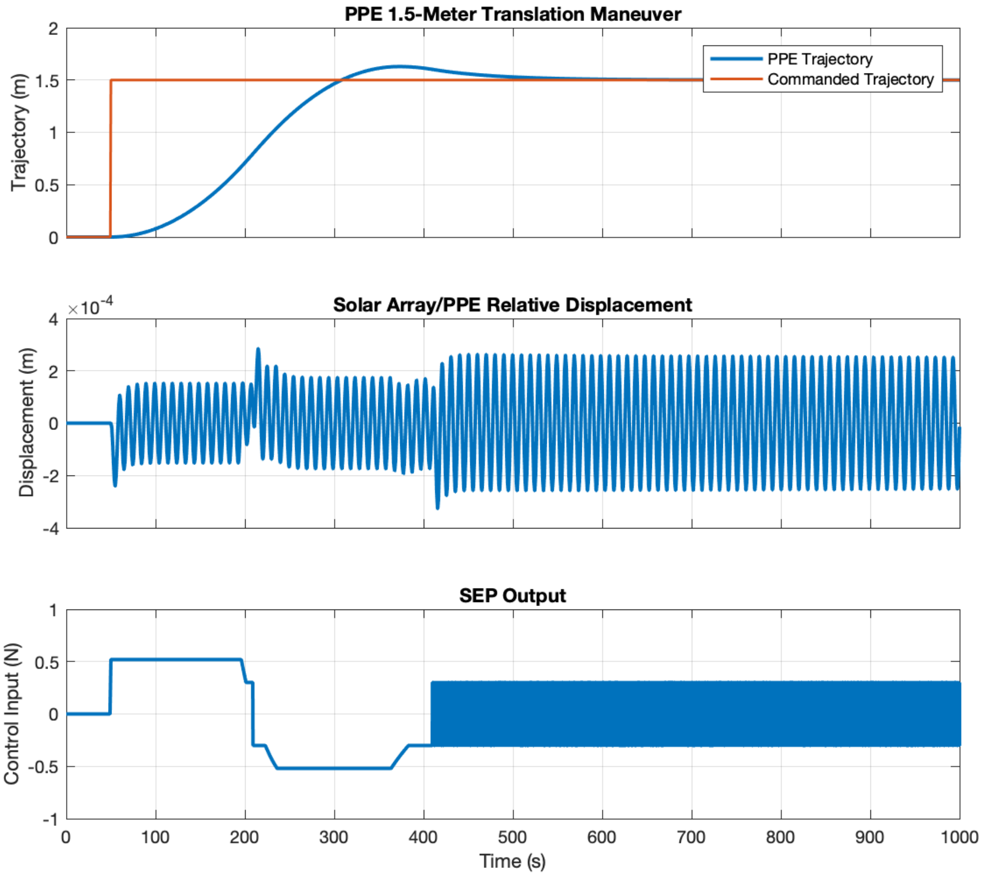

Figure 5-13: Case Study 1 (FWLQR): Control Objective and Control Input Simulation Output for Scenario #1

The performance of the FWLQR's Scenario #1 is comparable to the performance of the LQR's Scenario #1 (Figure 5-7). The settling time for both scenarios is around $t = 500$ seconds, and both scenarios have similar percent overshoots, and do not have relative displacements that exceed amplitudes on the order of 10^{-4} m. There are some slight differences, most notably including the increased relative displacement of the LQR's Scenario #1 by approximately 10^{-4} m, but for the most part the two scenarios are compatible.

A heavy penalization on the spectral content of the displacement of the solar array relative to the PPE is represented by the following FWLQR Scenario #2 Q_{Output} and R weighting matrix setup:

$$Q_{Output} = \begin{bmatrix} 1 & 0 \\ 0 & 10000 \end{bmatrix}$$
$$R = 1$$

The simulation output is provided in Figure 5-14.

Scenario #2 shows a sharp reduction in the spectral content of the relative displacement control objective. By $t = 950$ seconds, the relative displacement is oscillating between +/- 5×10^{-6} meters, and continues to be reduced. Additionally, no percent overshoot is experienced by the PPE as it accomplishes the primary control objective. The settling time is only extended by 200 seconds as compared to FWLQR's Scenario #2.

The spectral content of FWLQR's relative displacement outputs for Scenarios #1 and #2 is as follows (Figure 5-15).

The spectral content at 0.1 Hz is very similar for the FWLQR Scenario #1 as compared to LQR's Scenarios #1 and #2. The FWLQR's Scenario #2 0.1 Hz spectral content output is very significantly reduced, as expected by the high penalization on spectral content at the 0.1 Hz frequency. Referring back to Figure 5-14, the amplitude of the relative displacement output is continuously reduced throughout the 1000 second simulation. Additionally, this significant penalization did not come with a significant detriment to the settling time of the PPE in regards to its translation objective of 1.5 meters.

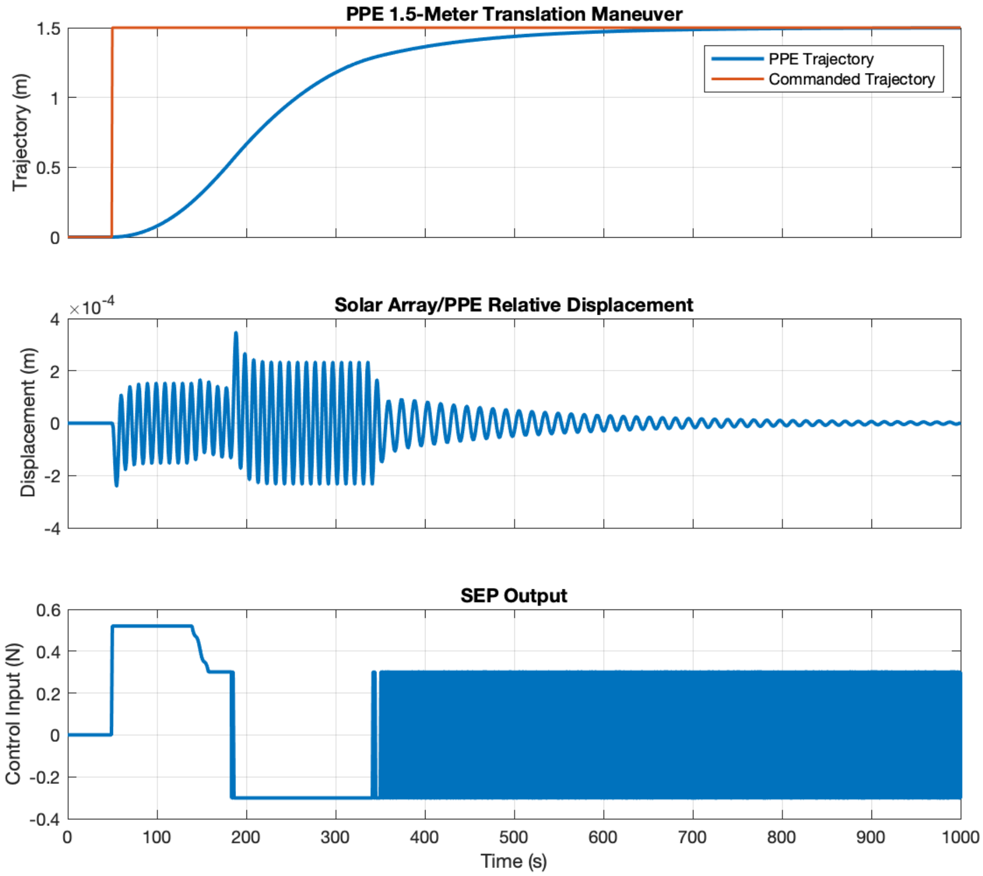

Figure 5-14: Case Study 1 (FWLQR): Control Objective and Control Input Simulation Output for Scenario #2

The control input profile of the FWLQR control methodology is similar to those seen in the other controllers. Very rapid firings ensue after the PPE completes the majority of its 1.5-meter translation. This firing process may strain the PPE's structural capabilities, in regards to the constant on/off switching that is required to complete the profile. The impact of the semi-continuous limiting function is also negative, in the sense that if the forcing function is removed, the relative displacement reduces to a smaller amplitude by the end of a 1000 second simulation, and the spectral content across the entire simulation time frame is reduced slightly as well.

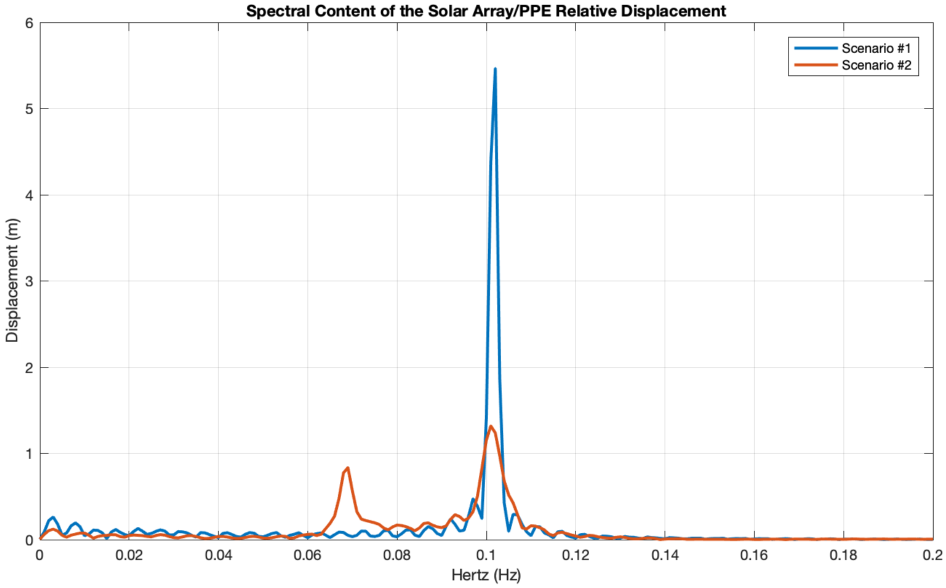

Figure 5-15: Case Study 1 (FWLQR): Spectral Content Relative Displacement Output Comparison for Scenarios #1 and #2

5.1.5 MPC

MPC is the final CSI mitigation strategy to be tested in this case study. Unlike the previous control methodologies, MPC is capable of considering both the semi-continuous SEP system and the binary RCS system as it attempts to complete the primary and secondary control objectives. Additionally, the ability to consider semi-continuous control input variables is inherent in the MPC control methodology logic, which will nullify performance inhibitions associated with forcing a continuous control input signal external to the control law to be semi-continuous (as was the case with the PID, LQR, and FWLQR control methodologies).

In addition to being able to consider multiple input actuator types, the MPC methodology has the ability to penalize spectral activity at user-specified frequencies, much like the capability introduced in the FWLQR CSI mitigation strategy. MPC also has the ability to constrain certain output objective ranges.

Simulation #1 consists of the MPC controller using the SEP and the RCS systems to accomplish both its primary and secondary control objectives. The Q_{Output} matrix takes on a slightly different meaning for MPC then it did for the FWLQR control strategy. MPC will consider a multi-objective output matrix C, where:

$$C = \begin{bmatrix} 1 & 0 & 0 & 0 \\ -1 & 0 & 1 & 0 \end{bmatrix}.$$

The output matrix, as written for MPC, considers the physical outputs of the PPE position and the relative displacement of the solar array/PPE stack (and not the spectral content, as Q_{Output} denoted in the FWLQR section (Section 4.4)). The Q_{Output} and R weightings of the controller for Simulation #1 are as follows:

$$Q_{Output} = \begin{bmatrix} 125 & 0 \\ 0 & 1 \end{bmatrix}$$
$$R_{RCS} = 1$$
$$R_{SEP} = 0.1.$$

The Q_{Output} matrix was formed with a 125 scalar cost weighting on the PPE's position and a 1 scalar cost weighting on the solar array/PPE relative displacement because it effectively balanced the PPE settling at the 1.5-meter displacement objective and the avoidance of excessive control input firings. The R_{SEP} scalar weighting cost of 0.1 was selected to allow the MPC controller to use the SEP system more liberally in an attempt to fine-tune the PPE at its 1.5-meter displacement objective. This is desired for vibration mitigation, as the SEP has a thruster output range that is three orders of magnitude less than the RCS jets. The outputs by Simulation #1 are provided in Figure 5-16.

Under the MPC mitigation strategy, the PPE accomplishes its primary objective in approximately 35 seconds, which runs second only to the phase plane control CSI mitigation strategy simulation output (Figure 5-1), which was able to meet the primary control objective in less than 10 seconds. The primary concern with the phase plane control method, however, were the significant oscillations of the solar array, which exceed 1 meter in amplitude. The MPC methodology decreases these oscillations by an order of magnitude, and therefore has already outperformed the other Case Study 1 control methodologies with respect to the primary and secondary control objectives.

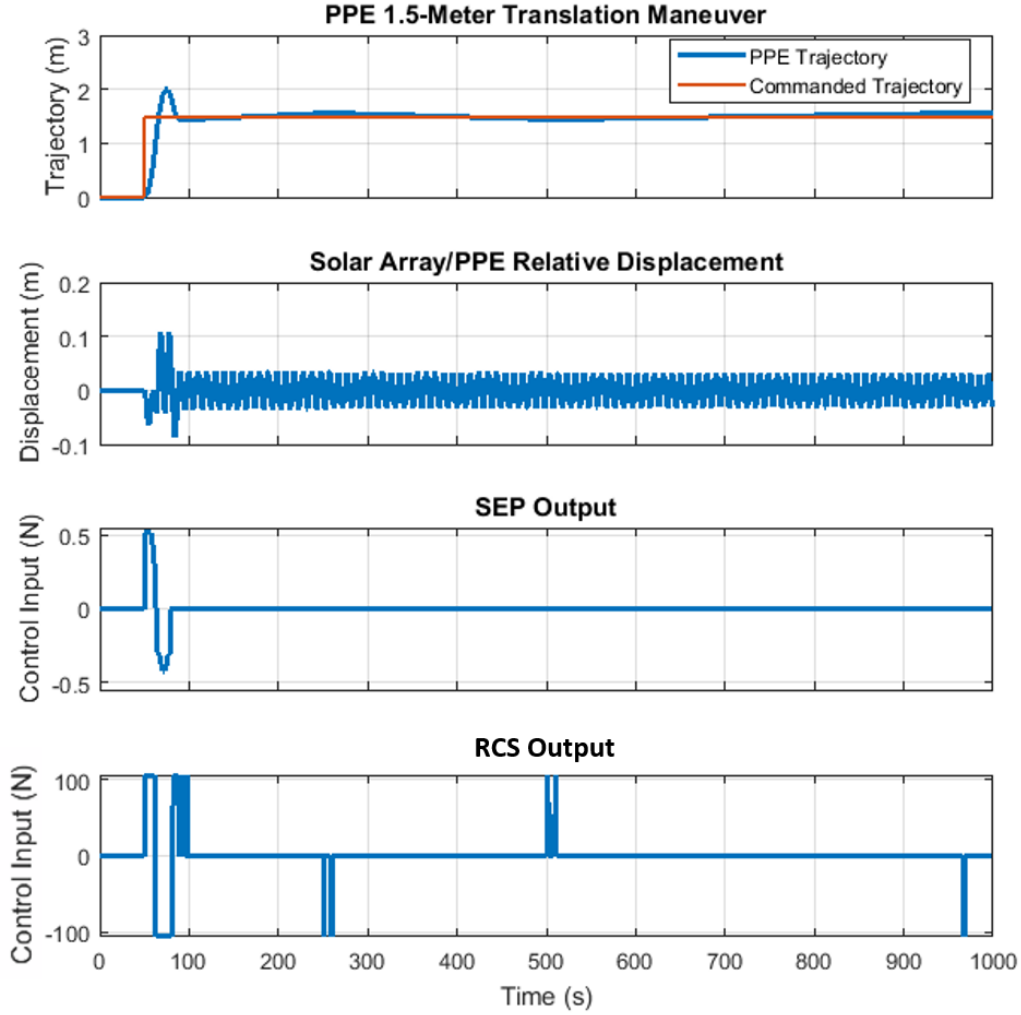

Figure 5-16: Case Study 1 (MPC): Control Objective and Control Input Simulation Output for Scenario #1

An additional form of added value provided by the MPC control methodology was its ability to minimize the amount of SEP and RCS control inputs needed in the simulation. In Simulation #1, no control input firings are made beyond $t = 200$ seconds. Each control method prior to MPC included very rapid "on-off" firings that not only would expend a greater amount of fuel, but could also strain the mechanical infrastructure of an actual propulsive system onboard the PPE. With fewer thruster firings and clusters of intense thruster "on-off" switching, the PPE is able to accomplish both the primary and secondary control objectives. It is interesting to note that even with a scalar cost weighting of 1 for the Q_{Output} corresponding to the relative displacement, that the secondary control objective only had an amplitude of 0.02 meters.

One drawback to a strong PPE settling time, an impressive conservation of control input energy, and a relatively small solar array/PPE relative displacement is a 0.5 meter initial overshoot of the 1.5 meter trajectory target. Unfortunately, this is not fixed by placing an output constraint on the PPE position, because at the time both the SEP and the RCS systems are already actively engaged trying to compensate for the initial overshoot (and are limited by their respective maximum values) Additionally, the prediction horizon (N) is 1. The drawbacks to this will be discussed shortly.

One drawback of a binary RCS actuator system for MPC is the computational burden in the execution of simulations. Although this was not a problem with other CSI mitigation strategies, it became a problem with long prediction horizons. One way in which this is mitigated is the conversion of the binary RCS system to a continuous system that does not resemble a force output, but rather a resultant ΔV from a actuation source. This method can be applied to additional control methods as well, and can lead to better methodology performance. If this method were to have been developed for the PID, LQR, and FWLQR CSI mitigation strategies, the Case Study #1 simulation scenarios would have yielded better results, as these control methods are designed to yield continuous actuation control inputs. However, this method was primarily developed and implemented so as to allow the MPC controller to become less computationally intensive. Chapter 6.3 mentions the application of this method to the PID, LQR, and FWLQR control strategies as a potential area for future work in relation to research presented in this thesis.

Simulation #1 saw a prediction horizon N of 1. This value was increased to 100 for Simulation #2, and the Q_{Output} and R matrices were adjusted to be as follows:

$$Q_{Output} = \begin{bmatrix} 1 & 0 \\ 0 & 100 \end{bmatrix}$$

$$R_{RCS} = 1$$

$$R_{SEP} = 0.01.$$

Figure 5-17 shows the suite of Simulation #2 outputs (Figure 5-17).

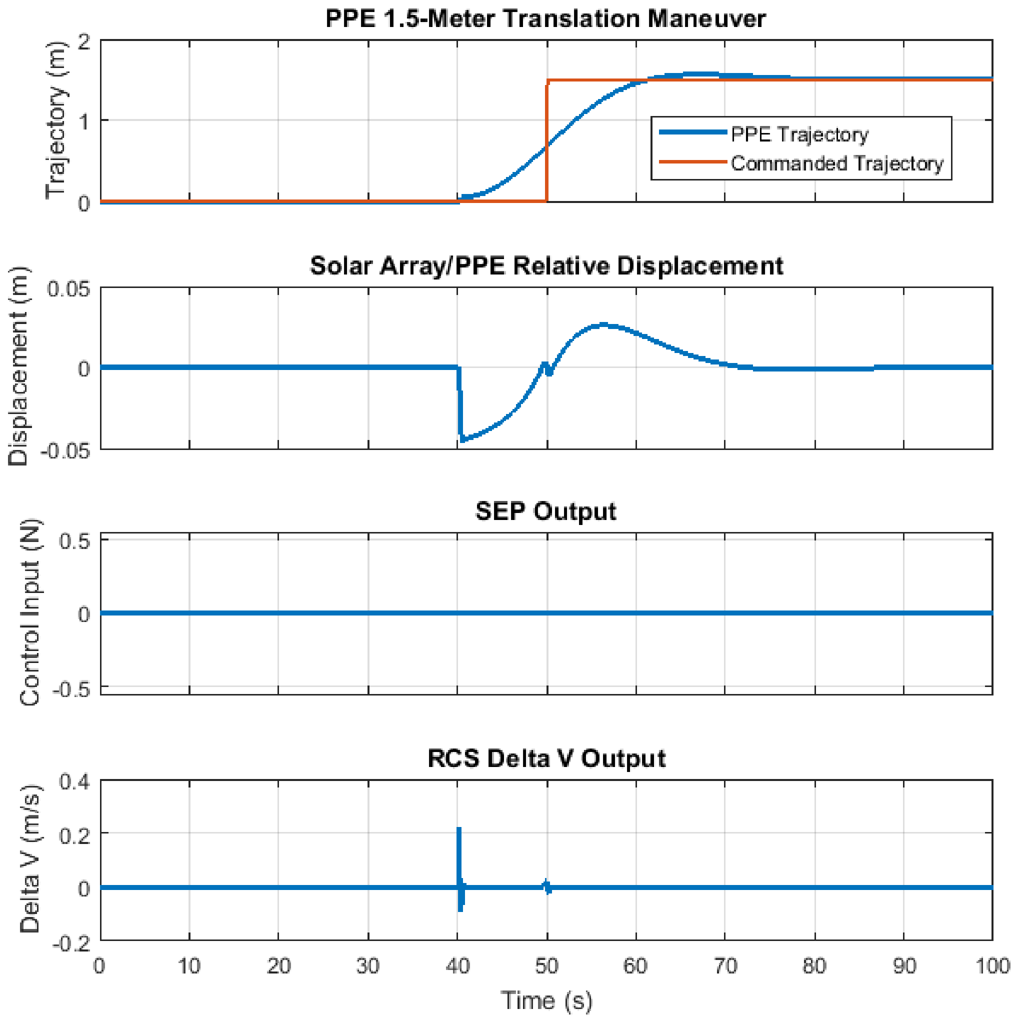

Figure 5-17: Case Study 1 (MPC): Control Objective and Control Input Simulation Output for Scenario #2

The overshoot of the PPE is dramatically reduced, and the relative displacement remains at the same order of magnitude to Scenario #1. Scenario #2 also demonstrates the predictive capabilities of MPC. Slightly before the step input, the controller engages and sends the PPE on its translation trajectory, demonstrating an effective prediction of the step change to come. Additionally, the RCS ΔV output produces just enough ΔV to have the PPE settle at its 1.5-meter displacement target, and, over the $t = 1000$ second simulation, reduces the relative displacement of the solar array/PPE stack to approximately 0 meters. Through the MPC CSI mitigation strategy, a precise amount of ΔV was computed to settle the PPE at its target in a relatively fast 40 seconds, and has an unparalleled reduction in solar array/PPE relative displacement when compared to other CSI mitigation strategies evaluated so far in this thesis.

The effectiveness of the predictive capabilities of MPC is also demonstrated by the simulation incurring no SEP inputs throughout the entire simulation interval. Despite the very small 0.01 weighting value being placed on the input cost matrix R, the MPC control methodology does not generate any SEP control actions. The combination of a continuous variable input with a predictive ΔV capability did not require even minor SEP control input actions.

In reference to Figure 5-17, it must also be stated that the sampling period had to be increased from its standard 0.01 seconds to 0.1 seconds. This is the only simulation in which the sampling period deviated from 0.01 seconds thus far. A sampling period of 0.01 seconds, combined with the desire to have a predictive capability of 10 seconds equated to a prediction horizon of 1000. A simulation on this order would take an extensive period of time (approximately an hour).

The MPC methodology still has the added ability of penalizing spectral content at designated frequencies, in addition to placing output constraints on a control objective. Scenario #2's performance does not require either of these elements. Scenario #3 will return to a setup similar to that of Scenario #1 (with a decrease in the value of the R_{SEP} value by one order of magnitude), with the prediction horizon N being returned to 1 to accommodate binary RCS control input action and the sampling period being returned to 0.01 seconds.

$$Q_{Output} = \begin{bmatrix} 125 & 0 \\ 0 & 1 \end{bmatrix}$$
$$R_{RCS} = 1$$
$$R_{SEP} = 0.01.$$

Without frequency weighting or output constraints, the output for Scenario #3 is as follows (Figure 5-18).

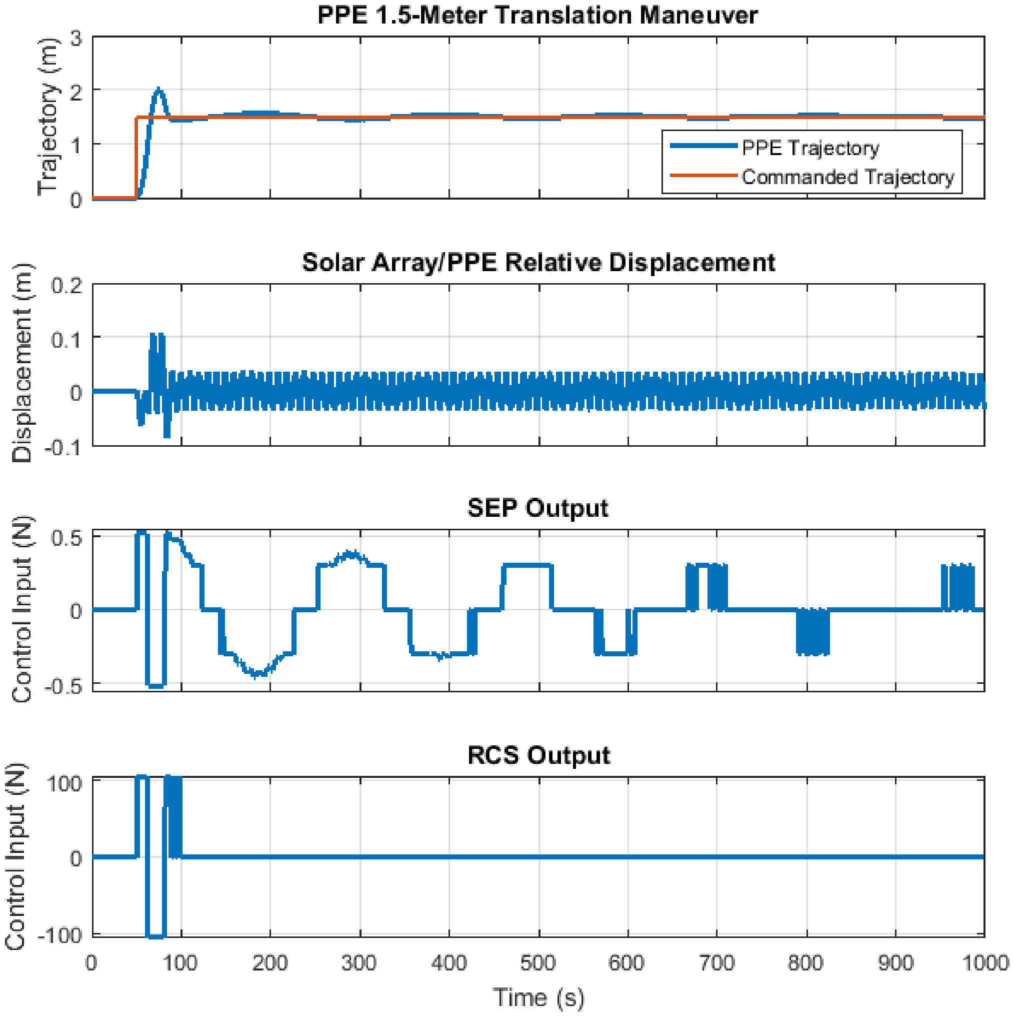

Figure 5-18: Case Study 1 (MPC): Control Objective and Control Input Simulation Output for Scenario #3

The reasoning behind choosing an R_{SEP} value of 0.01 is to better enable the SEP to make minor adjustments to the PPE's trajectory and the displacement of the solar array relative to the PPE.

Frequency weighting is then turned on, and the output weighting cost value placed on minimizing the spectral content at 0.1 Hz is set at 1000, thus indicating to the cost function that tolerating spectral content at the 0.1 Hz frequency is more expensive than using adequate control inputs to effectively accomplish the primary and secondary control objectives.

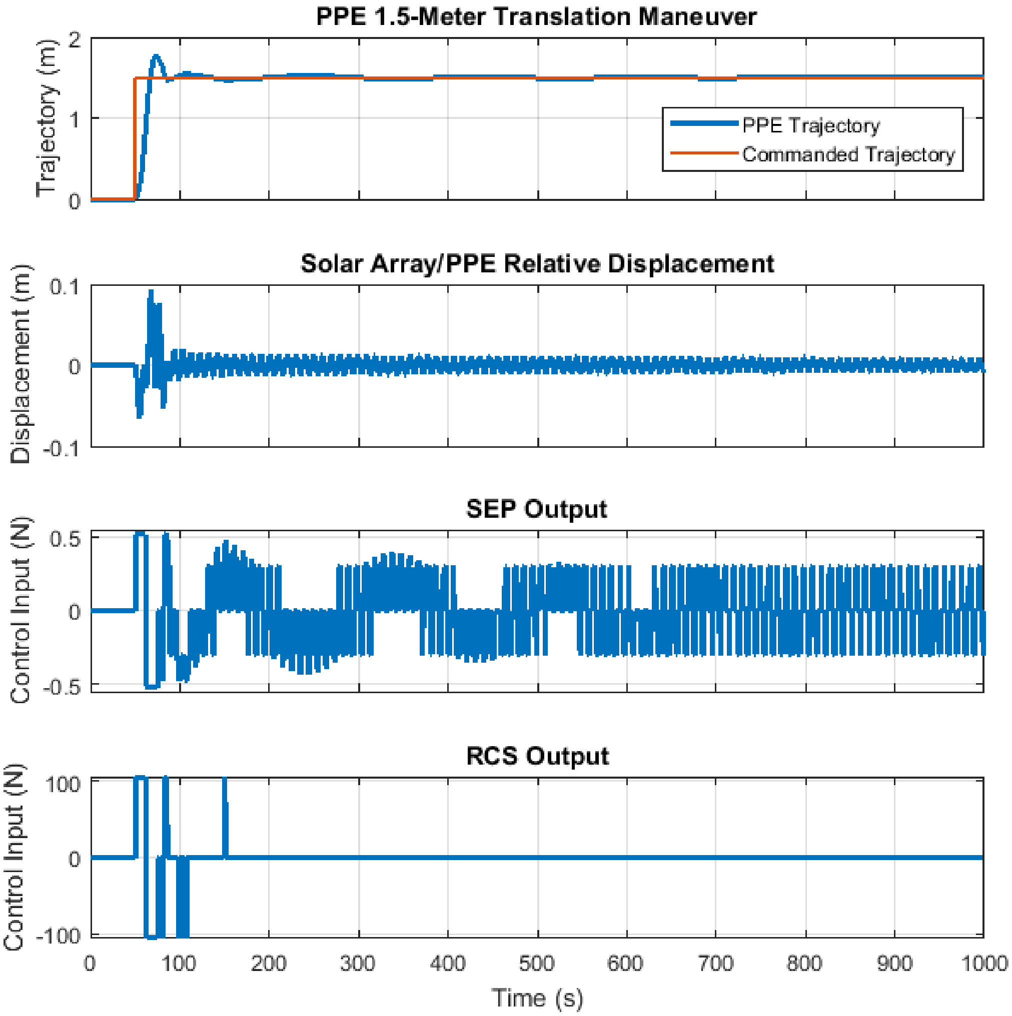

Figure 5-19: Case Study 1 (MPC): Control Objective and Control Input Simulation Output for Scenario #3 with Frequency Weighting "On"

The application of frequency weighting greatly reduces the level of amplitude for oscillations occurring after $t = 125$ seconds, thus reducing the spectral activity at the 0.1 Hz frequency.

An additional value of the MPC CSI mitigation methodology is to use output constraints to further minimize the relative displacement output. To best show the value of this CSI mitigation facet, a new scenario was crafted to show the value of constraining the output values, and how this can serve as another (or an additional) option when it comes to reducing the amplitude of relative displacement oscillations. For this simulation, the sampling period was once again reduced to 0.1 seconds compared to Scenario #3's 0.01 seconds. Scenario #4 is comprised of the following scalar cost weighting matrices:

$$Q_{Output} = \begin{bmatrix} 1 & 0 \\ 0 & 0 \end{bmatrix}$$

$$R_{RCS} = 1$$

$$N = 10$$

The primary control objective is accomplished with a minimal overshoot and in a matter of seconds. However, the relative displacement of the solar array/PPE stack has an initial amplitude of 1.5 meters. Another effective strategy of reducing the amplitude and spectral content of the relative displacement control objective capable through the MPC CSI mitigation methodology is through the application of output constraints. An output constraint is placed on the relative displacement control objective at +/- 0.01 meters, and is associated with a weighted $R_{OutputConstraint}$ cost of 100, thus emphasizing the prioritization that the cost function would place on using an appropriate amount of input energy to minimize the spectral content at the 0.1 Hz frequency (the sample size remains at 0.1 seconds) (Figure 5-21).

The amplitude of the relative displacement control objective is reduced by two orders of magnitude when compared to Scenario #4 (without output constraints), as shown by Figure 5-20. In the initial 30 seconds of the simulation, the output constraints penalize the displacement strongly, and reduce what would have been an initial amplitude of 1.4 meters (see Figure 5-20) to a displacement less than 0.05 meters. The fourth subplot in Figure 5-21 indicates the distance at which the solar array/PPE relative displacement deviates from the output constraint of 0.01 meters, and proceeds to penalize this value greatly until the relative displacement is oscillating just under 0.01 meters.

MPC has a variety of tools that enable it to effectively accomplish the primary and secondary control objectives: frequency weighting, the explicit accommodation

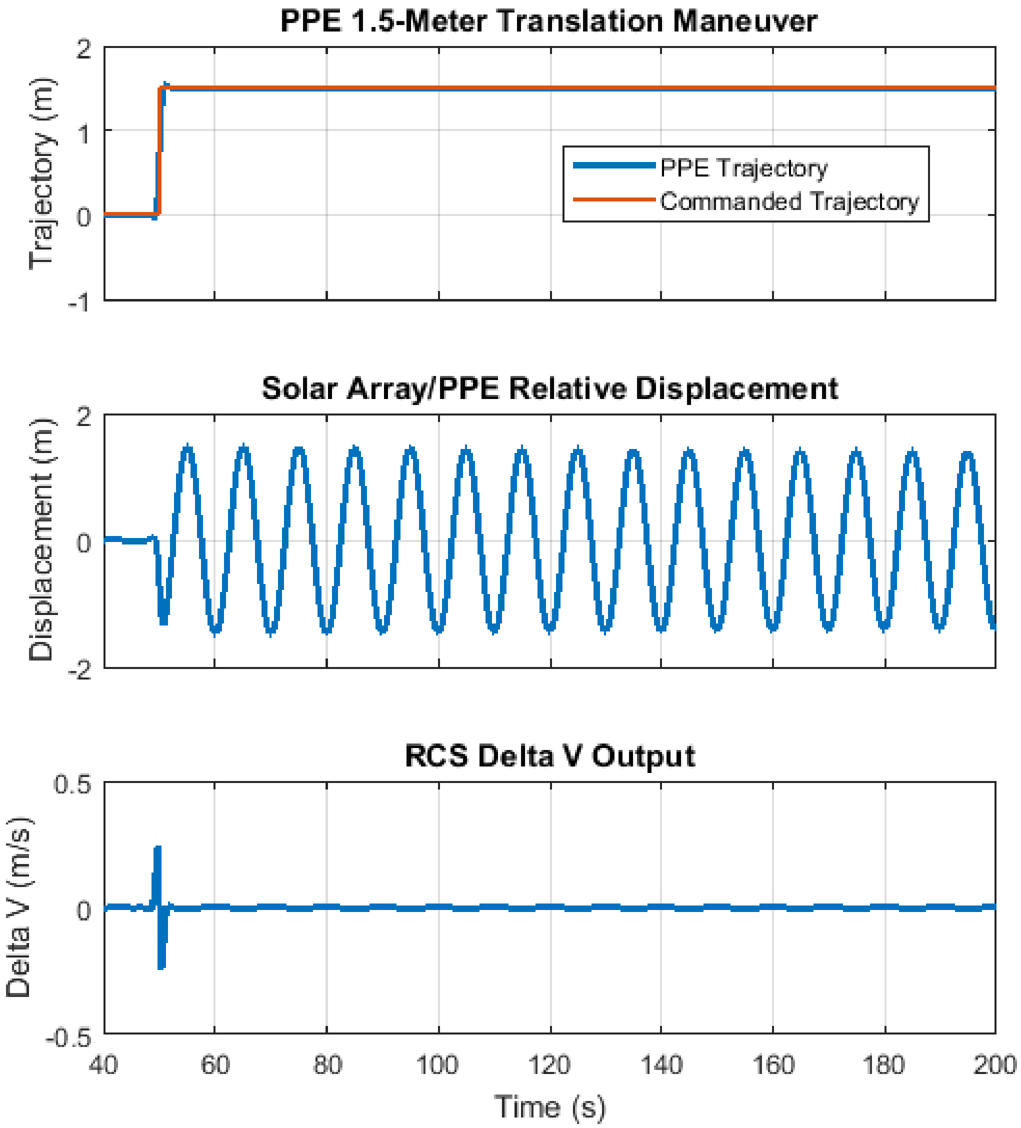

Figure 5-20: Case Study 1 (MPC): Control Objective and Control Input Simulation Output for Scenario #4

of input constraints, and the establishment of output constraints. Figure 5-17 demonstrates the best performance of any simulation output in Case Study #1. Figure 5-17 shows a settling time of approximately 40 seconds after the issuance of the 1.5-meter translation command, and a relative displacement that converges to approximately 0 meters. In conclusion, the MPC strategy has the ability to incorporate a variety of tools that enable both the effective translation of a space station module, with

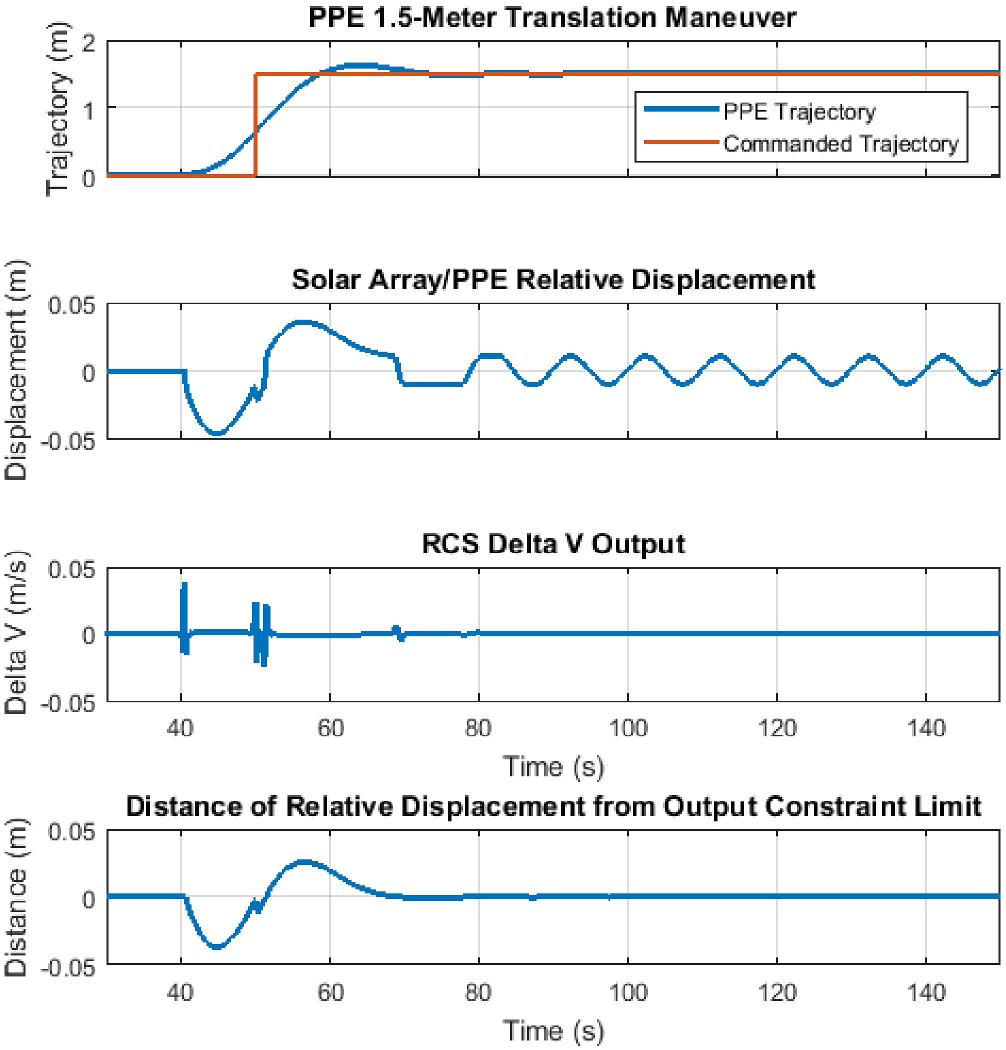

Figure 5-21: Case Study 1 (MPC): Control Objective and Control Input Simulation Output for Scenario #4 with Output Constraints

the added benefit of managing the spectral content of the solar array/PPE relative displacement superbly.

One of the most significant drawbacks of MPC is the computational effort required to accomplish the primary and secondary control objectives. Out of all the CSI mitigation strategies, MPC takes the most time to complete various control objectives. Scenario #2, for example, took almost 22 minutes to complete. The primary drivers behind increased simulation duration are the prediction horizon, small sampling periods, and the considering of the binary RCS thrust actuators. The primary reason behind this is the massive thrust that the "on-off" RCS jets produce, 106 N, which far exceeds the thrust ranges of the SEP system and the ΔV continuously-variable control input magnitudes seen in this Case Study. Reducing the magnitude of this thrust would reduce the amount of time required to complete simulations.

5.2 Case Study 2: Attitude Control

Simulations regarding attitude control consider different structural dynamics compared to the translational LTI model, as expressed in Chapter 3. Vibrations and oscillations between varying structural elements of the Gateway will ensue from both translational and rotational maneuvers, and because the Gateway will be expected to conduct three-axis attitude control [53] in addition to translational maneuvering, each CSI mitigation strategy should be considered in a set of simulations covering rotational dynamics.

For attitude control, the PPE will have the capability of using its SEP system (semi-continuous), its RCS thrusters (binary) and its CMG/RW (continuous) non-propulsive systems to complete attitude change maneuvers. Each CSI methodology will be evaluated against the following primary and secondary control objectives.

1. **Primary Objective**: Enable the PPE's completion of a 180 degree rotation about one axis.

2. **Secondary Objective**: Minimize the amplitude and the spectral content of the angular displacement of the solar array relative to the PPE.

5.2.1 Phase Plane Controller

The phase plane control theory was introduced and elaborated upon in Chapter 4.1, and Chapter 5.1.1 included the phase plane controller's performance for the translational LTI model. The rotational LTI model, much like the translational LTI model, will use the RCS "on-off" jets to complete the 180 degree attitude change maneuver.

Figure 5-22 provides the simulation output of this maneuver with the notch filters on the feedback channel centered at 0.1 Hz.

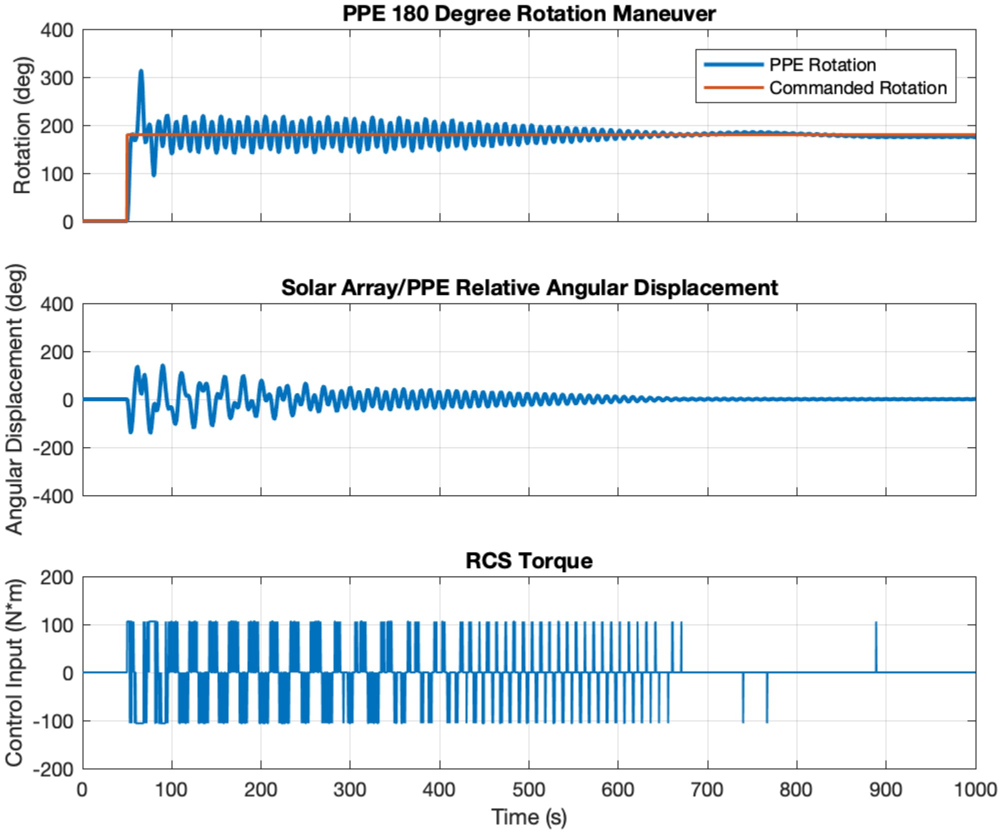

Figure 5-22: Case Study 2 (Phase Plane): Control Objective and Control Input Simulation Output for Scenario #1

The simulation outputs of the rotational LTI model defined in Chapter 3.1.2 look fundamentally different than those of the linear LTI model defined in Chapter 3.1.1 (and represented in Figure 5-1). The PPE module reaches its targeted rotation within 5 seconds, but proceeds to oscillate around the 180 degree target at a fairly consistent frequency until about 350 seconds into the simulation. At this point, the PPE's angular displacement about its target reduces until reaching an adequately reduced state at approximately $t = 700$ seconds.

Comparatively, the oscillations for the rotational phase plane simulations are not as smooth as they are for the translational model outputs in Figure 5-1. In the first 100 seconds of the simulation, the rotational simulation result experiences two significant spikes, both above and below the targeted rotation. The first spike extends to an angular displacement greater than 300 degrees, and an ensuing spike returns the PPE to a 100 degree angular displacement from its origin at approximately 50 seconds into the simulation. In addition to this, the relative angular displacement of the solar array/PPE stack are much less modal than they were for the translational LTI model. Much of this has to do with the relatively massive mass moment of inertia of the solar array. In the linear LTI model, the mass of the solar array is 3.13% of that of the PPE. For the rotational model, the mass moment of inertia of the solar array is over 4.6 times that of the PPE. This is primarily because of the wide rectangular plate that was chosen to represent the solar array, and the cylinder that was chosen to represent the PPE. The attitude control case study provides a unique perspective on CSI mitigation strategies, as the challenge of applying control inputs to the object of least inertia to control an object of more inertia tethered by a spring and a damper will test each control methodology in a new way. In terms of the translational model, the control inputs were being applied to a much more massive object. For rotational models, actuation inputs will be sourced from the significantly less inertial PPE.

Despite the more "erratic" behavior compared to that of the translational model, the application of the same notch filters used for the rotational model causes the noticeable reduction in the relative angular displacement control objective. Additionally, as mentioned in the previous paragraph, the notch filter also reduces the oscillation of the PPE itself as it converges closer to its primary control objective. However, similar to the translational model's simulation results, the relative angular displacement incurs rather large initial displacements (to values greater than +/- 100 degrees from the desired 0 degree mark).

The RCS jets incur rapid "on-off" firings in the first half of the simulation, but reduce to sporadic singular firings towards the end of the 1000-second timeframe. This is another noticeable positive difference compared to the translational model's simulation outputs, which experienced continual and dense firings throughout the entire simulation timeframe.

Figure 5-23 provides an additional perspective as to the performance of the phase plane control system for the rotational LTI state space model by illustrating the phase plane portrait for Scenario #1.

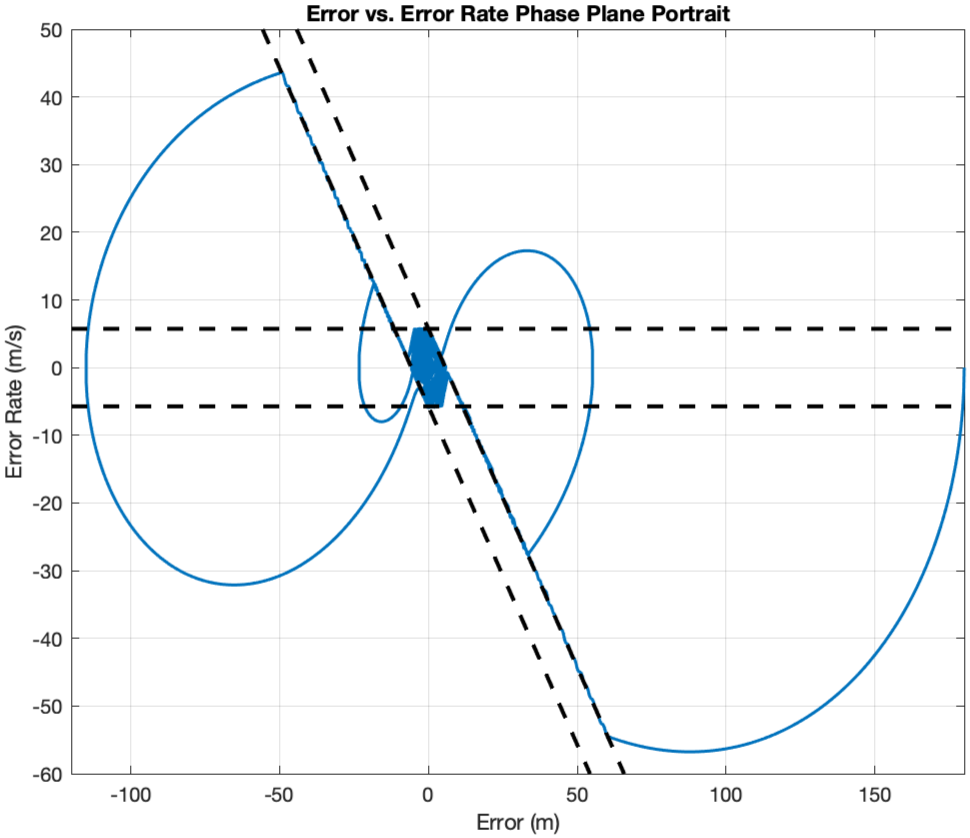

Figure 5-23: Case Study 2 (Phase Plane): Two-Dimensional Portrait for Scenario #1

What is immediately noticeable in the phase plane portrait are the longer duration RCS burns that flare out from beyond the center drift zone, which is where the PPE eventually settles. These flares correspond to the sharp peaks in the first 100 seconds of the simulation. Due to the particularly massive mass moment of inertia for the solar array relative to that of the PPE, both the control objective output plots of the primary and secondary control objectives are not as smooth when compared to their translational counterparts. This can be visualized by viewing the spectral content of the simulation, which will be presented in Figure 5-25. Prior to presenting the spectral content of the stable system, the notch filters at 0.1 Hz will be removed to demonstrate the instabilities caused, forming the parameters for Scenario #2:

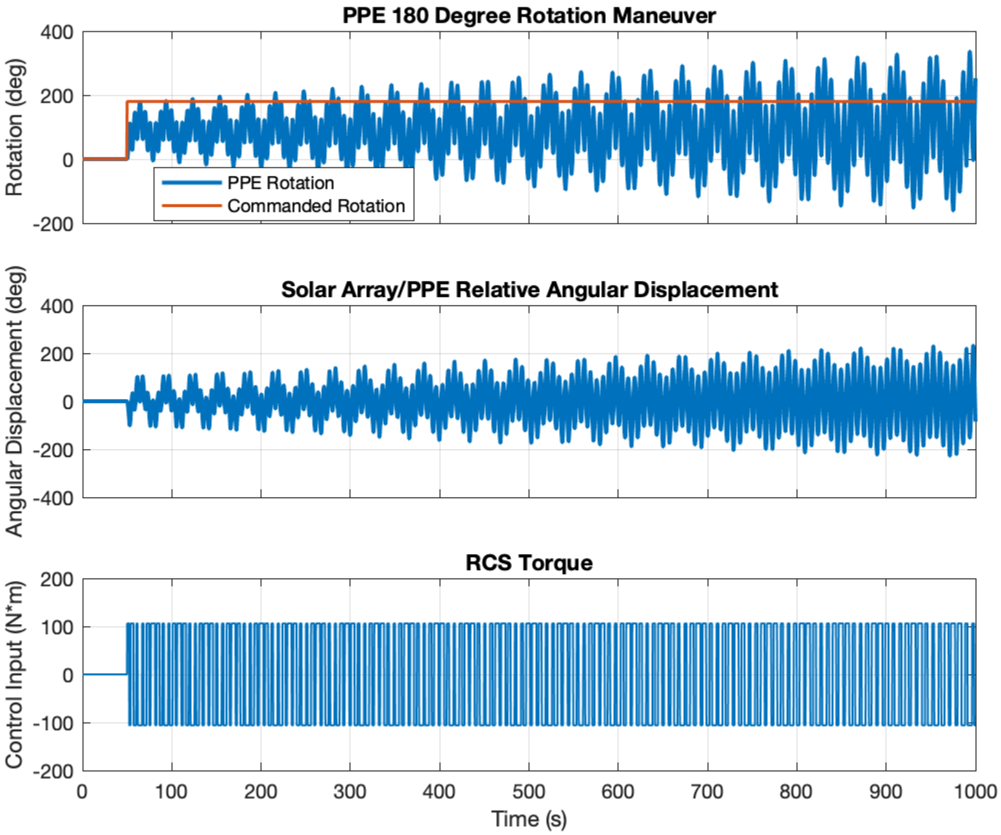

Figure 5-24: Case Study 2 (Phase Plane): Control Objective and Control Input Simulation Output for Scenario #2

Similar to the removal of notch filters on the linear LTI model, the rotational system goes unstable for Case Study 2's Scenario #2. Figure 5-25 compares the spectral content of the stable Scenario #1 with that of the unstable Scenario #2:

The unstable system is characterized by two prominent peaks of spectral activity at around 0.03 Hz and at a frequency near 0.14 Hz. The application of the notch filter reduced the spectral activity at these frequencies, and shifted them slightly to surrounding frequencies. Similar to the spectral content comparison of the translational model (Figure 5-4), the application of the notch filter at 0.1 Hz caused for a slight spread of the spectral energy to surrounding frequencies. Additionally, the most prominent peak of spectral content for the unstable system is at a frequency

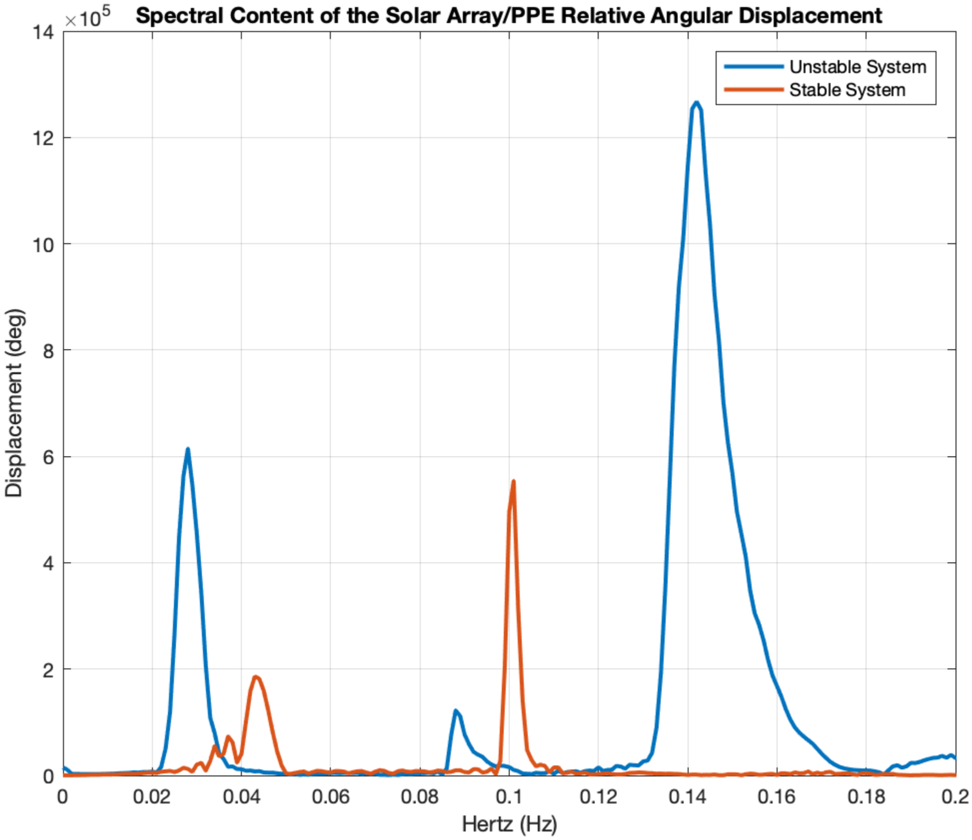

Figure 5-25: Case Study 2 (Phase Plane): Spectral Content Output Comparison between Scenario #1 (Stable) and Scenario #2 (Unstable)

slightly greater than 0.14 Hz. The author assumes that this is primarily because of the rounding of the spring constant coefficient κ calculated for the rotational model, and because of the multi-modal oscillations of the unstable system.

5.2.2 PID Controller

The PID controller was introduced from a theoretical perspective in Chapter 4.2, with Chapter 5.1.2 providing the simulation results for the PID's application to the translational LTI simulation model. For the rotational model, the PID can provide control actuation inputs for the continuous CMG/RW systems. The following individual control gains were selected (without any external automated tuning system) to allow the PPE to accomplish both the primary and secondary control objectives:

$k_P = 5$, $k_I = 0.0001$, and $k_D = 1000$.

The resultant PID output plots are referenced as Figure 5-26.

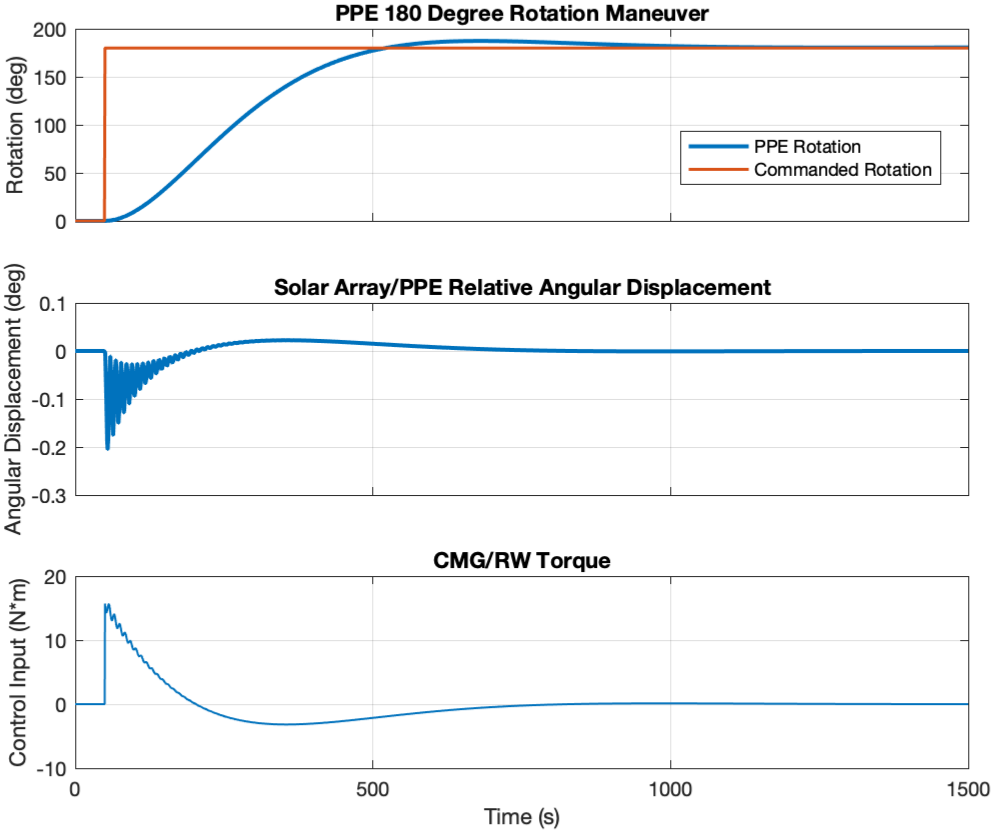

Figure 5-26: Case Study 2 (PID): Control Objective and Control Input Simulation Output

The PID controller provides a continuous set of input torques that minimize the overshoot of the PPE to its 180 degree target. Additionally, relative to the phase plane simulation results applied to the rotational LTI model, the relative solar array/PPE angular displacement peaks at an absolute amplitude of approximately 0.2 degrees in the initial time elements of the simulation. The angular relative displacement then dissipates to a value approximating 0 degrees by the end of the 1500 second simulation. The spectral content of the secondary control objective is presented in Figure 5-27.

Relative to the relative angular displacement between the PPE and the solar array

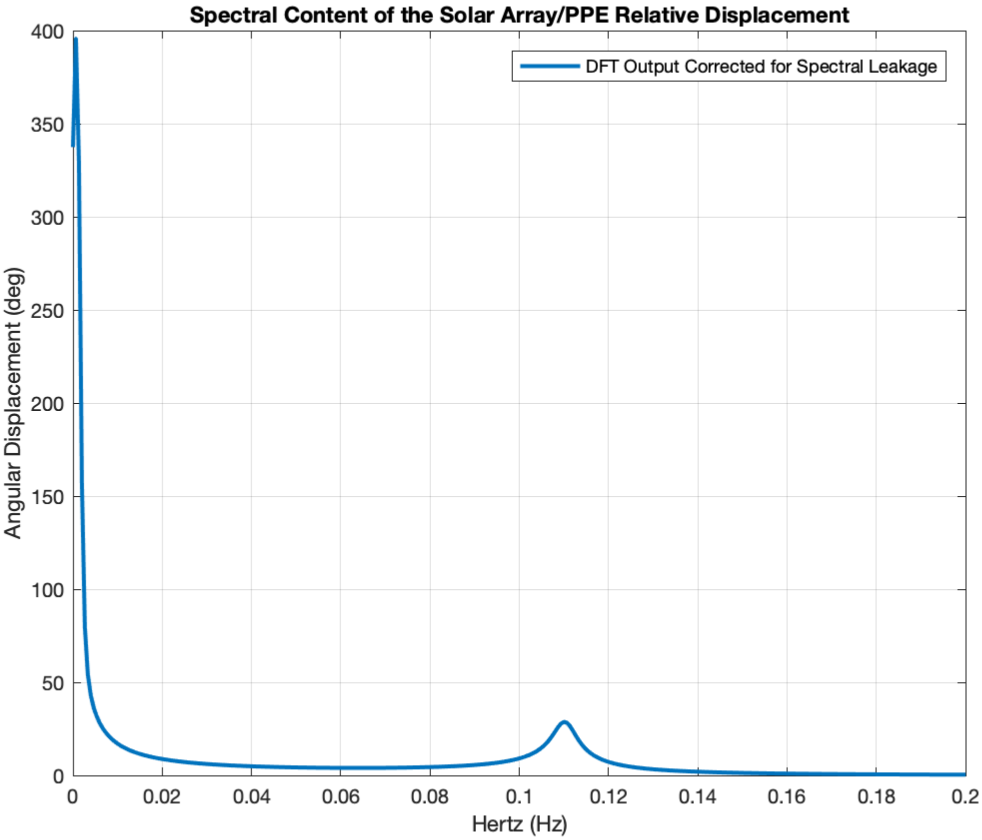

Figure 5-27: Case Study 2 (PID): Spectral Content Output

for the phase plane simulation results in Case Study 2, there is a significant decrease in spectral content activity (by 5 orders of magnitude) for the PID simulation outputs. The frequency activity very close to 0 Hz is caused by the oscillatory action of a smaller frequency as the relative angular displacement converges to 0 degrees. This is seen in Figure 5-26 at around 250 seconds, where the 0.14 Hz frequency activity is largely attenuated, and the relative displacement then slowly (over the next 250-300 seconds or so) converges to 0 degrees.

5.2.3 LQR

The LQR was introduced from a theoretical perspective in Chapter 4.3, with Chapter 5.1.3 providing the simulation results for the LQR's application to the translational LTI simulation model. Similar to the PID controller, the LQR is able to provide control actuation inputs for the continuous CMG/RW systems. No semi-continuous limiting function is required to convert a naturally continuous control action to a semi-continuous control effort. Figure 5-28 provides the control objective and control input simulation output for an LQR controller with the following Q and R setup.

$$Q = \begin{bmatrix} 1000 & 0 & 0 & 0 \\ 0 & 1 & 0 & 0 \\ 0 & 0 & 10 & 0 \\ 0 & 0 & 0 & 1 \end{bmatrix}$$
$$R = 1$$

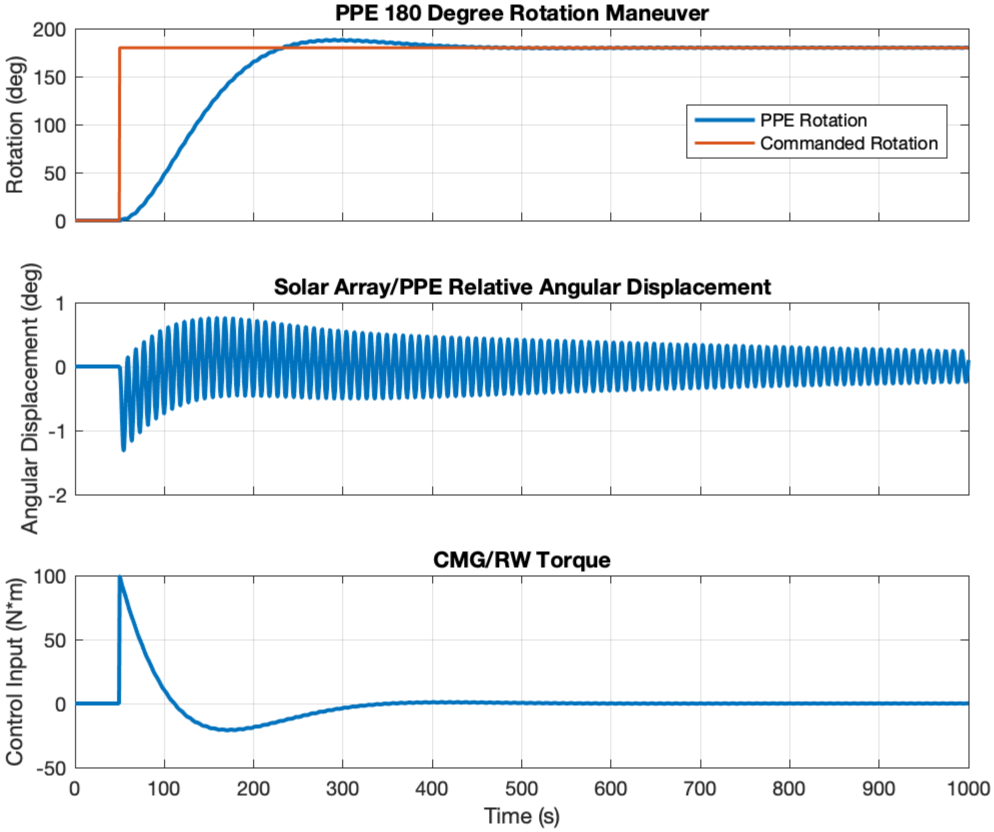

Figure 5-28: Case Study 2 (LQR): Control Objective and Control Input Simulation Outputs

The relative angular displacement is one order of magnitude larger than that presented in the PID relative angular displacement. This is because the settling time of the PPE in the LQR simulation is at approximately 450 seconds into the simulation, as opposed to the PID's settling time value that is slightly less than 1100 seconds. The LQR controller was tuned to provide a significantly reduced settling time, in exchange for slightly more relative angular displacement activity, which correlates to an increase in spectral content at around 0.1 Hz:

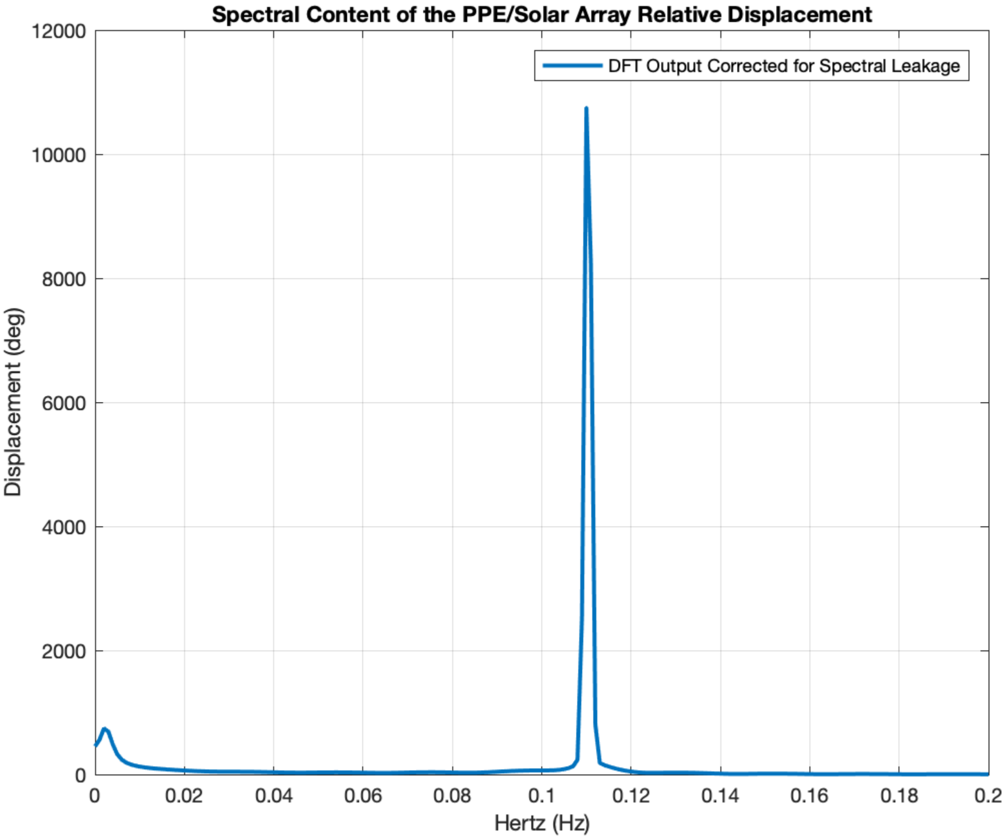

Figure 5-29: Case Study 2 (LQR): Spectral Content Output

At the frequency spike at approximately 0.15 Hz, the order of magnitude is approximately three times greater as compared to that of the PID spectral content output (Figure 5-27). An additional point of interest that can be made is that, compared to the PID controller, the LQR expends more energy, in regards to the torque CMG/RW control input. The LQR control input peaks at approximately 100 Nm, which is an order of magnitude greater than the approximate 15 Nm induced torque (Figure 5-26) of the PID controller. The primary tradeoff between the PID and the LQR controllers for the rotational LTI model is the settling time. A decreased settling time for the LQR is accompanied by more spectral content at the natural frequency and a larger CMG/RW control input.

5.2.4 FWLQR

The FWLQR was introduced from a theoretical perspective in Chapter 4.3, with Chapter 5.1.4 providing the simulation results for the FWLQR's application to the translational LTI simulation model. Similar to both the PID and LQR controllers, FWLQR controllers provide continuous control actuation inputs, which work well with the continuous CMG/RW non-propulsive systems. No semi-continuous limiting function is required for this reason. Figure 5-30 provides the control objective and control input simulation results for the FWLQR controller with the following Q_{Output} and R setup.

$$Q_{Output} = \begin{bmatrix} 1000 & 0 \\ 0 & 0 \end{bmatrix}$$
$$R = 1$$

It is important to mention that the definition of Q_{Output} for the FWLQR control methodology is defined in the same way as Q_{Output} for the FWLQR control methodology in Case Study #1's simulation results.

Scenario #1 does not consider any weighting on the spectral content of the relative displacement control objective. In terms of the primary control objective and the control input, Figure 5-30 looks very similar to the LQR output plot (Figure 5-28). The control input peaks at 100 Nm, and the primary control objective settles at approximately 450 seconds. Compared to the LQR simulation results, the angular relative displacement plot shows a decrease in amplitude by one order of magnitude, and oscillations significantly less than 0.1 Hz. Without any frequency weighting, the relative displacement of the solar array/PPE stack is already very small, with a peak deviation from the 0 degree target of -1 degree. Engaging the frequency weighting option creates the simulation results presented in Figure 5-31.

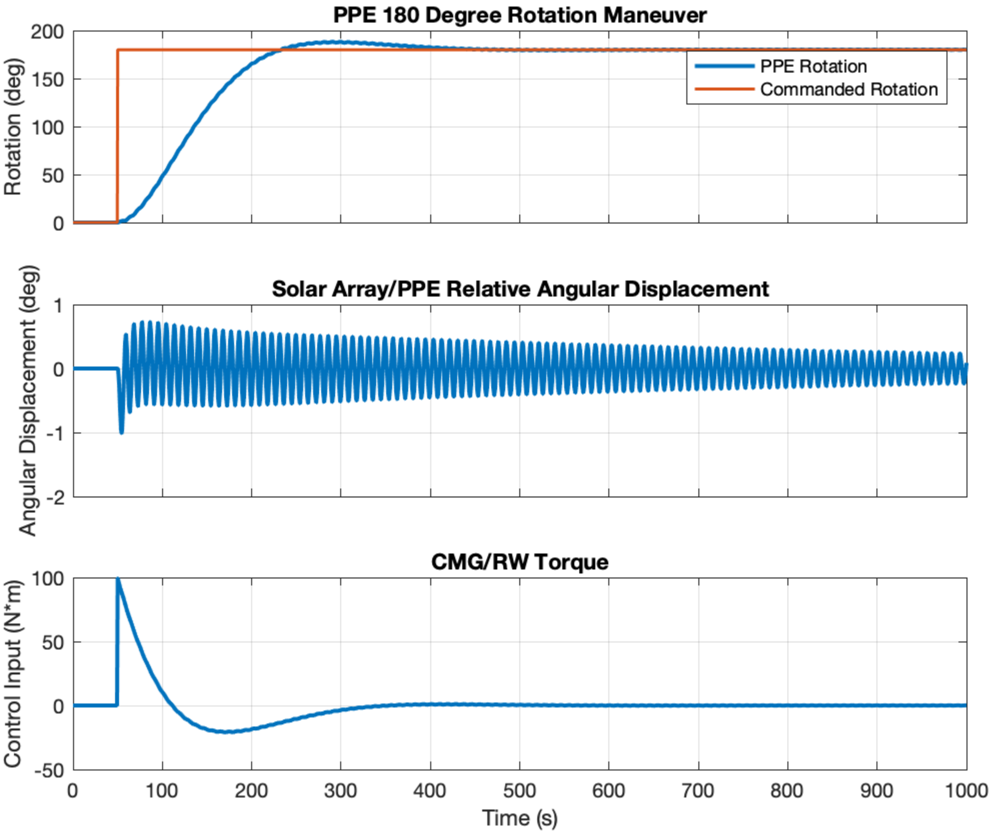

Figure 5-30: Case Study 2 (FWLQR): Control Objective and Control Input Simulation Outputs for Scenario #1

$$Q_{Output} = \begin{bmatrix} 1000 & 0 \\ 0 & 10000 \end{bmatrix}$$
$$R = 1$$

In Figure 5-31, there isn't a noticeable difference in the overshoot or settling time of the PPE as it completes its 180 degree rotation. Additionally there is not a significant change in the control input provided by the CMG/RW system. There is, however, a noticeable decrease in the relative angular displacement amplitudes. Although there is an initial peak at approximately 1 degree from the origin (similar to the results from Scenario #1), there is a noticeable decrease in the amplitude compared to the Scenario #1 results. To provide more evidence to this fact is the spectral content plot (Figure 5-32) comparing Scenarios #1 and #2.

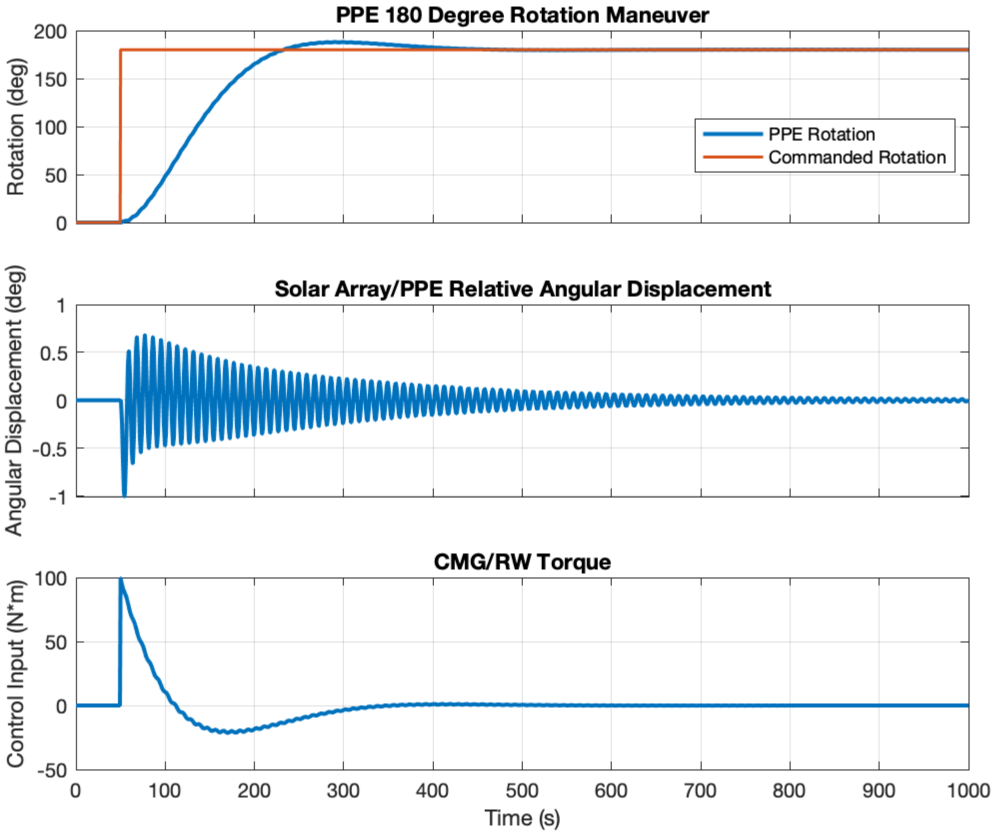

Figure 5-31: Case Study 2 (FWLQR): Control Objective and Control Input Simulation Outputs for Scenario #2

The FWLQR controller provides the capability to reduce the amount of spectral content at 0.15 Hz.

5.2.5 MPC

The MPC control strategy was introduced from a theoretical perspective in Chapter 4.4, with Chapter 5.1.5 providing the simulation results for the FWLQR's application to the translational LTI simulation model. As cited in these chapters, MPC hosts an array of capabilities that can be used to accomplish both the primary and secondary control objectives. In Case Study #1, MPC's frequency weighting and output constraining capabilities were demonstrated successfully, and the best results were illustrated in Figure 5-17. Figure 5-17's scenario included the consideration of a continuous input, and accomplished the primary control objective with a minimal

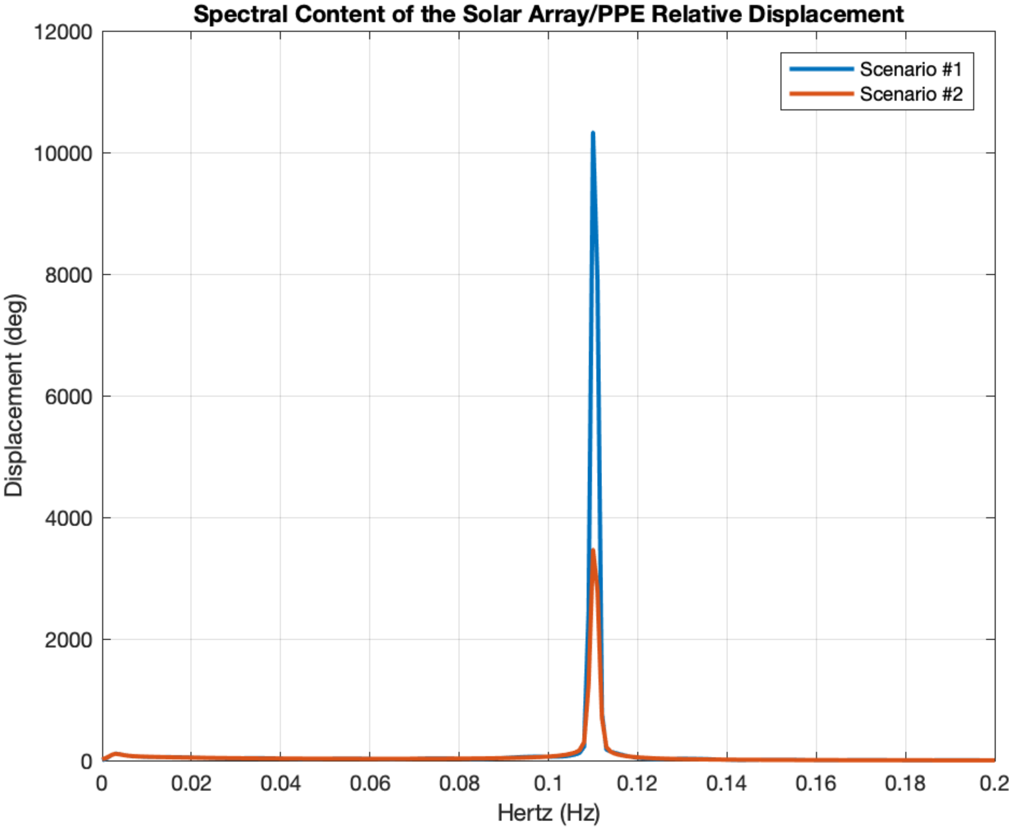

Figure 5-32: Case Study 2 (FWLQR): Spectral Content Comparison for Scenario #1 and #2

overshoot and with a 40 second settling time. Additionally, the displacement of the solar array relative to the PPE did not exceed +/- 0.05 meters, and dissipated to approximately 0 meters. Part of what enabled this was the consideration of a continuous actuator input, the ΔV input option.

For the rotational model, a continuous actuator input is available in the form of the CMG/RW system. It has already been demonstrated that the continuously-variable ΔV input option yields favorable results. However, an input torque is not the same as the ΔV input option, and an additional simulation will be completed with the CMG/RW system as the only active input actuation source available on the PPE. The following model was considered with a prediction horizon of 100 steps and a sample period of 0.1 seconds, considers the CMG/RW system, and provides a completely non-propulsive solution to attitude control. Simulation outputs are provided in Figure 5-33. Frequency-weighting and output constraint capabilities are not considered in regards to this scenario. The definition of the output matrix C for the multi-objective MPC strategy is as follows:

$$C = \begin{bmatrix} 1 & 0 & 0 & 0 \\ -1 & 0 & 1 & 0 \end{bmatrix}.$$

The output matrix, as written for MPC, considers the physical outputs of the PPE position and the relative displacement of the solar array/PPE stack (and not the spectral content, as Q_{Output} denoted in the FWLQR sections of this thesis. The Q_{Output} and R weightings of the controller for the rotational model's MPC simulation are as follows:

$$Q_{Output} = \begin{bmatrix} 10000 & 0 \\ 0 & 1 \end{bmatrix}$$
$$R_{CMG/RW} = 0.1$$

The objective of this scenario is to see how the PPE would respond to a focus on accomplishing the primary control objective. MPC has already showcased its ability to accomplish the secondary control objective with its suite of features. How quickly can the PPE accomplish its primary control objective, and what would the relative displacement look like?

The primary control objective sees a minimal percent overshoot, and has a settling time of approximately 160 seconds. The relative angular displacement stays minimal, although it is larger than secondary control objective outputs presented for other CSI mitigation strategies in Case Study #2. It is assumed that a relative angular displacement of $-4°$ to $2.5°$ will not strain the physical solar array/PPE connection to excess. Even with a significant emphasis on the primary control objective, the relative displacement still only showcases a small angular displacement, and mitigates this displacement to effectively 0 shortly after t = 400 seconds. The CMG/RW system, even with a relatively smaller input cost setting, operates within the first 200 seconds, but then tapers to a control input torque of 0 Nm. The simulation's output

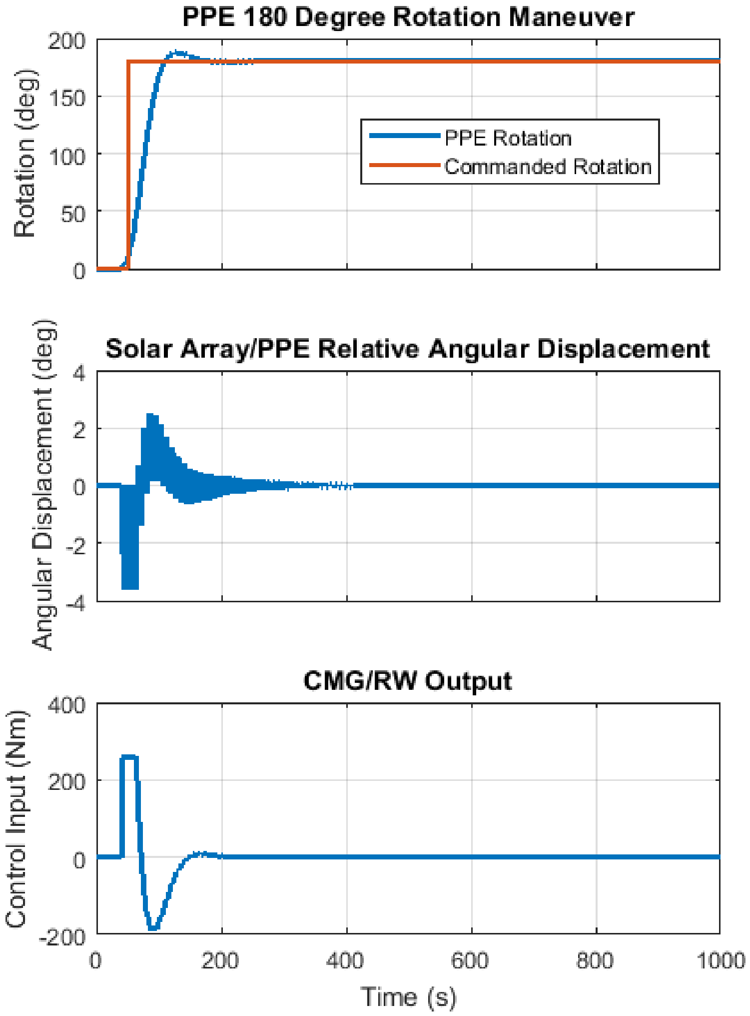

Figure 5-33: Case Study 2 (MPC): Control Objective and Control Input Simulation Outputs

shows the effectiveness of MPC in planning non-propulsive attitude change maneuvers. The cost weighting matrix setup is heavily influenced towards accomplishing the primary control objective and more freely expending CMG/RW input torques at the expense of directing focus on accomplishing the secondary control objective. This setup is made to accomplish the primary control objective expediently using a non-propulsive attitude control system, and shows that in a heavy setting to accomplish this objective, the secondary control objective stays within manageable limits.

Chapter 6

Conclusion

6.1 Contribution

The Gateway is a space station that is going to be placed into a NRHO sometime in the 2020s. The Gateway, which promises to be comprised of multiple modules and additional structural elements (e.g., a robotic arm, visiting vehicles, external payloads, etc.), is unique when compared to more recent classes of crewed spacecraft. The station will be large; it will be a flexible space structure comprised of many elements that will have a variety of structural modes. Although it will not be as large as the ISS, it will have to contend with many of the same CSI structural dynamic considerations that large spacecraft (such as the Space Shuttle when docked to the Mir or the ISS) will have to consider when planning translational or attitude control maneuvers.

The heritage regarding the Space Shuttle served as a launching point for the discussion of developing a CSI mitigation strategy for the Gateway. The Space Shuttle's interactions with payloads, the Russian space station Mir, and the ISS are unique when considering the past several decades of space flight, and demanded a comprehensive CSI mitigation strategy. The Space Shuttle, which relied on a phase plane controller to conduct on-orbit attitude control, was supplemented with a notch filter on its feedback channel to address issues of CSI mitigation. The notch filter-based approach successfully addressed the need for a more robust CSI mitigation strategy onboard the Shuttle, but it was a solution that was constrained by the existing control architecture of the Shuttle. When unconstrained by the Shuttle's architecture, additional CSI mitigation strategies can be considered for their ability to potentially outperform the phase plane-based approach.

Few other spacecraft, whether crewed or uncrewed, have had to consider as many structural elements as the Space Shuttle had to during its docked operations with Mir and the ISS. With the Shuttle's final flight having been almost 9 years ago since the publication of this thesis, and the notch filter concept having been developed for the Shuttle almost 32 years ago, an evaluation of whether or not the notch-filter based CSI mitigation strategy should be applied to the Gateway is validated. The Gateway will be comparable to the Shuttle/Mir or the Shuttle/ISS stack in the sense that it will be comprised of multiple structural elements, and by extension, will have multiple dominant modes of vibration. The CSI mitigation strategy that the Gateway adopts will need to be adaptable, flexible, and capable of handling the challenges inherent to large, flexible space structures.

The PPE will be the first module of the Gateway stack launched, and it will carry with it 300 kW solar arrays. The flexible configuration studied in this thesis is that of the PPE with one of the solar arrays extended. A translational and rotational model were developed to model this configuration. A primary control objective was formulated that caused the PPE to translate forward by 1.5 meters (Case Study #1) or to rotate the spacecraft by 180 degrees (Case Study #2). The secondary control objective was established to manage the resultant oscillations stemming from the control inputs used to maneuver the spacecraft to its targeted translation or rotation objective. Each CSI mitigation strategy was tested in an attempt to accomplish these same control objectives. These simulations were completed in an attempt to find a potential alternative to the assumed state-of-the-art Space Shuttle CSI mitigation method.

6.2 Recommendations

MPC, for its performance as well as its inherent capabilities as a control method, appears to be the best option for CSI mitigation onboard the Gateway. For the translational model, Figure 5-17 provides the simulation output that most effectively accomplished both the primary and secondary control objectives out of any of the other CSI mitigation strategies. The prediction horizon enabled a predictive control input 10 seconds prior to the 1.5-meter translation command. Additionally, the continuous control inputs were optimized in such a fashion that the relative displacement between the solar array and the PPE peaked at approximately 0.03 meters, and then settled at a value close to 0 meters only 80 seconds into the start of the simulation (and 30 seconds after the 1.5-meter reference command). In terms of accomplishing the primary and secondary control inputs, while also conserving control inputs, Figure 5-17 (Scenario #2 of MPC's performance in Case Study #1) provided the best simulation output out of any of the other control methodologies.

In the rotational maneuver, Case Study #2, MPC also exhibited an impressive ability to use a non-propulsive continuous-variable input source to quickly bring the PPE to its 180 degree rotation objective with a heavy Q_{Output} cost weighting value on the primary control objective (Figure 5-33). The angular relative displacement of the solar array/PPE stack for this specific case remained low, and dissipated to 0 degrees shortly after 400 seconds into the simulation.

MPC appears to be the optimum candidate for performing CSI mitigation techniques on the Gateway in the context presented in this thesis, but there are several considerations that go beyond the results of the simulations depicted that can greatly influence this decision. There are tradeoffs inherent to each of the CSI mitigation strategies presented in this thesis. For the LQR, FWLQR, and MPC control methodologies, the concept of a cost function is based upon tradeoffs. The designer must sometimes decide what is valued more: a faster settling time, or a larger relative displacement between the solar array/PPE stack? Is conservation of propellant a concern? Is a large overshoot a topic of concern, or is it acceptable for the specific maneuver at hand? The phase plane controller simulation output presented in Figure 5-1 has the fastest settling time out of all of the control methodologies presented in Case Study #1. However, the resultant relative oscillations exceed 1 meter, which will most likely strain the base of the solar arrays to the point of breaking off from the PPE. There are a variety of tradeoffs inherent in the options of each CSI mitigation strategy. MPC, for example, has the longest computational time out of any of the control methods evaluated in this thesis. If time to compute maneuvers is a concern, then MPC may not be the best option, or the strategy should be more finely tuned to provide more timely results. Decisions must be constantly made as to what performance metrics are valued in one maneuver's case versus those of another. An adaptable control methodology that can lead to solutions with respect to whatever additional constraints may exist is an imperative element of any control strategy that the Gateway, or any other spacecraft, should adopt. Likewise, many areas of future work are introduced in this thesis to attain a more definable answer to the question of which CSI mitigation strategy would be most suited in supporting the Gateway.

6.3 Future Work

6.3.1 Advanced Model Development

There are many ways in which the simulation models used in this thesis can be better developed to more accurately test the CSI mitigation strategies used. In Chapter 3, the PPE and solar array configuration models were developed with respect to precedent suggesting the capability of simple, spring-mass-damper LTI state-space models. The translational and rotational models used to portray the PPE and one solar array were developed with respect to this precedent. The goal was to provide a simple platform to evaluate the CSI mitigation capabilities of each controller with one primary frequency of interest. In many of the simulations presented, spectral activity was limited to areas close to 0 Hz and 0.1 Hz. These simplified frequency peaks allowed for a more easily verifiable CSI mitigation strategy.

By applying more structural elements with varying frequency peaks (i.e., modules, visiting vehicles, external payloads, communications infrastructure, etc.), CSI mitigation strategies can be tested on more complex models. Additionally, as explained in Chapter 3, there is a difference between designing a CSI mitigation for control law design, and control law verification. When an adequate model for control law design has been completed, the resultant controller profiles are applied to more complex models for verification purposes.

6.3.2 Computational Load Analyses

Another significant element of deciding whether or not to use one control method over another is through a better understanding of the computational load that each CSI mitigation strategy may demand on flight software. It was mentioned that MPC runs tend to take longer than any of the other CSI mitigation strategy simulation runs considered in this thesis. A question aside from the run times in the control law design stage is the ability for modern processors to handle MPC control action design. Studies done on the suitability of MPC CSI mitigation methods for flight hardware are imperative to accomplish prior to their acceptance as integral to the Gateway's flight control system.

6.3.3 ΔV Continuous Variable Input

One of the reasons why MPC outperformed the other CSI mitigation methodologies for Case Study #1 was because of its ability to produce continuous ΔV inputs. Figure 5-17, which was cited as being the best performing simulation in this thesis, was because of the ability of MPC to consider a continuous input in which an output in meters per second was produced, as opposed to a control input force in Newtons. It was mentioned that this capability could be extended to the PID, LQR, and FWLQR control methodologies in Case Study #1 specifically, which experienced degradations in performance because of the inability of these control strategies to produce a input variable type that was anything but continuous. Expanding the ΔV capability demonstrated with MPC to accommodate the other CSI mitigation methodologies would expand the validity of the analyses completed within this thesis.

Bibliography

[1] National Aeronautics and Space Administration. International Space Station Poster. EW-2007-02-150-HQ. URL: `https://www.nasa.gov/pdf/179225main_ISS_Poster_Back.pdf`.

[2] National Aeronautics and Space Administration. Space Shuttle Mission Archives: STS-6. URL: `https://www.nasa.gov/mission_pages/shuttle/shuttlemissions/archives/sts-6.html`.

[3] National Aeronautics and Space Administration. NASA Space Flight Human-System Standard - Volume 2: Human Factors, Habitability, and Environmental Health. In *NASA Technical Standard: NASA-STD-3001*, Washington, DC 20546-0001, February 2015. Volume 2, Revision A. URL: `https://standards.nasa.gov/standard/nasa/nasa-std-3001-vol-2`.

[4] National Aeronautics and Space Administration. About the Space Station Solar Arrays, August 2017. Page Editor: Mark Garcia; NASA Official: Brian Dunbar. URL: `https://www.nasa.gov/mission_pages/station/structure/elements/solar_arrays-about.html`.

[5] National Aeronautics and Space Administration. Deep Space Gateway (DSG) Concept Power and Propulsion Element (PPE) Request for Information. Request For Information Solicitation Number: NNH17ZCQ006L, NASA/Goddard Space Flight Center, NASA Headquarters Acquisition Branch; Code 210.H; Greenbelt, Maryland 20771; United States, July 2017. Primary Point of Contact: Dr. Michele Gates; Director, Power Propulsion Element. URL: `{https://www.fbo.gov/index?s=opportunity&mode=form&tab=core&id=33368e53181a28d9fb7d9e8582aff8c7}`.

[6] National Aeronautics and Space Administration. NASA Procedural Requirements for Limiting Orbital Debris and Evaluating the Meteoroid and Orbital Debris Environments. *NODIS Library*, February 2017. Responsible Office: Office of Safety and Mission Assurance. URL: `https://nodis3.gsfc.nasa.gov/displayDir.cfm?t=NPR&c=8715&s=6B`.

[7] National Aeronautics and Space Administration. Power Propulsion Element For Deep Space Gateway Concept: Request for Information & Synopsis Virtual Industry Forum, July 2017. Key NASA Representative: Michele Gates, Director,

Power & Propulsion Element. URL: {`https://www.nasa.gov/sites/default/files/atoms/files/20170724-ppe-rfi-industry-forum-v5.pdf`}.

[8] National Aeronautics and Space Administration. Roll-Out Solar Array. Space Station Research Explorer on NASA.gov, January 2017. URL: `https://www.nasa.gov/mission_pages/station/research/experiments/explorer/Investigation.html?#id=1876`.

[9] National Aeronautics and Space Administration. FY 2019 Budget Request. 2018. URL: {`https://www.nasa.gov/sites/default/files/atoms/files/fy19_nasa_budget_estimates.pdf`}.

[10] National Aeronautics and Space Administration. International Space Station. •, November 2018. Page Editor: Mark Garcia; NASA Official: Brian Dunbar. URL: `https://www.nasa.gov/mission_pages/station/structure/elements/zarya-cargo-module`.

[11] National Aeronautics and Space Administration. Spaceflight Demonstration of a Power & Propulsion Element (PPE) Broad Agency Announcement (BAA). September 2018. NASA Glenn Research Center. URL: {`https://www.fbo.gov/index?s=opportunity&mode=form&id=c2e0e3c1c55f04e2052b2923f83b280e&tab=core&_cview=1`}.

[12] National Aeronautics and Space Administration. International Space Station Facts and Figures, March 2019. Page Editor: Mark Garcia; NASA Official: Brian Dunbar. URL: `https://www.nasa.gov/feature/facts-and-figures`.

[13] National Aeronautics and Space Administration. Space Station Assembly, March 2019. Editor: Mark Garcia; NASA Official: Brian Dunbar. URL: `https://www.nasa.gov/mission_pages/station/structure/elements/space-station-assembly`.

[14] National Aeronautics and Space Administration Jet Propulsion Laboratory-Caltech. Solar Power Technologies for Future Planetary Science Missions. Web, December 2017. Publication No.: JPL D-10136. URL: `https://solarsystem.nasa.gov/resources/548/solar-power-technologies-for-future-planetary-science-missions/`.

[15] National Aeronautics and Space Administration (NASA). Spaceflight Demonstration of a Power and Propulsion Element (PPE). Federal Business Opportunities Website, November 2017. Solicitation. URL: {`https://www.fbo.gov/index?s=opportunity&mode=form&id=4781210cbae339981c6725ca248a34aa&tab=core&_cview=1`}.

[16] National Aeronautics and Space Administration (NASA). Spaceflight Demonstration of a Power & Propulsion Element: Attachment A – Statement of Work. Federal Business Opportunities Website, June

2018. URL: {`https://www.fbo.gov/index?s=opportunity&mode=form&id=4781210cbae339981c6725ca248a34aa&tab=core&_cview=1`}.

[17] S. B. Amirault. Mass Moment of Inertia. Web, 2019. S.B.A. Invent: Mechanical Engineering References and Example Problems. URL: `https://sbainvent.com/dynamics/mass-moment-of-inertia/`.

[18] Brent D. Appleby. Reducing Shuttle-Payload Dynamic Interaction with Notch Filters. Masters thesis, Massachusetts Institute of Technology, 77 Massachusetts Avenue; Cambridge, MA 02139, February 1987. Property of the Charles Stark Draper Laboratory, Inc.

[19] ArianeGroup. 200N Bipropellant Thruster. *Orbital Propulsion Centre*, 2018. URL: `http://www.space-propulsion.com/spacecraft-propulsion/bipropellant-thrusters/200n-bipropellant-thrusters.html`.

[20] Corina Barbalata, Matthew W. Dunnigan, and Yvan Petillot. Coupled and Decoupled Force and Motion Controllers for an Underwater Vehicle-Manipulator System. *Journal of Marine Science and Engineering*, August 2018. Published by: Multidisciplinary Digital Publishing Institute. URL: `https://www.mdpi.com/2077-1312/6/3/96/pdf`.

[21] Stuart Bennett. The Past of PID Controllers. In *International Federation of Automatic Control*, volume 33, pages 1–11, Mappin Street, Sheffield, SI 3JD, UK, April 2000. Department of Automatic Control & Systems Engineering, The University of Sheffield. URL: `https://www.sciencedirect.com/science/article/pii/S1474667017382149`.

[22] P. A. Blelloch and N. R. Beagley. Tools for analysis of control-structure interaction, Aug 1990. 10.1049/cae.1990.0026. URL: `https://ieeexplore.ieee.org/document/60406`.

[23] The Boeing Company. Inertial Upper Stage Rocket - Historical Snapshot. URL: {`https://www.boeing.com/history/products/inertial-upper-stage-rocket.page`}.

[24] U.S. Congress. National Aeronautics and Space Administration. Web, February 2019. URL: `https://planetary.s3.amazonaws.com/assets/pdfs/advocacy/2019/FY19-Consolidated-Appropriations-Act-Committee-Report---NASA-Section.pdf`.

[25] Diane Davis, Sagar Bhatt, Kathleen Howell, Jiann-Woei Jang, Ryan Whitley, Fred Clark, Davide Guzzetti, Emily Zimovan, and Gregg Barton. Orbit Maintenance and Navigation of Human Spacecraft at Cislunar Near Rectilinear Halo Orbits. In *27th AAS/AIAA Space Flight Mechanics Meeting*, Lunar and Planetary Science and Exploration; Space Transporation and Safety,

pages 1–20, San Antonio, TX; United States, February 2017. NASA Johnson Space Center; Houston, TX, United States, American Astronautical Society; American Institute of Aeronautics and Astronautics. Document ID: 20170001347; Report/Patent Number: JSC-CN-38626; Contract/Grant/Task Number: NNJ13HA01C; NNX13AK60A. URL: `https://ntrs.nasa.gov/archive/nasa/casi.ntrs.nasa.gov/20170001347.pdf`.

[26] Casey Dreier. NASA just got its best budget in a decade: Patience pays off for the space agency after months of delay, February 2019. URL: `{http://www.planetary.org/blogs/casey-dreier/2019/0215-fy2019-nasa-gets-its-best-budget-in-decades.html}`.

[27] Engineer's Edge. Mass Moment of Inertia Equations. Web, May 2019. URL: `https://www.engineersedge.com/mechanics_machines/mass_moment_of_inertia_equations_13091.htm`.

[28] Jane Edwards. NASA Taps SSL to Conduct Deep Space Gateway Propulsion Study; Richard White Comments. *ExecutiveBiz*, November 2017. URL: `https://blog.executivebiz.com/`.

[29] Kathleen C. Howell Emily M. Zimovan and Diane. C. Davis. Near Rectilinear Halo Orbits and Their Application in Cis-Lunar Space, 2017. IAA-AAS-DyCoSS3-125. URL: `https://engineering.purdue.edu/people/kathleen.howell.1/Publications/Conferences/2017_IAA_ZimHowDav.pdf`.

[30] Lawrence C. Evans. An Introduction to Mathematical Optimal Control Theory: Version 0.2. Department of Mathematics; University of California, Berkeley, 1983. Compilation of Lecture Notes.

[31] William Gerstenmeier and Jason Crusan. Cislunar and Gateway Overview. *National Aeronautics and Space Administration*, pages 1–13, •. URL: `https://www.nasa.gov/sites/default/files/atoms/files/cislunar-update-gerstenmaier-crusan-v5a.pdf`.

[32] Susan Gomez, Valery Platonov, Elizabeth Medina, Alexander Borisenko, and Alexey Bogachev. Unexpected Control Structure Interaction on International Space Station. In *International Astronautical Congress*, JSC-CN-39881, Adelaide, Australia, September 2017. NASA Johnson Space Center; Houston, TX, United States. Document ID: 20170006953; Meeting Sponsor: International Astronautical Federation; Paris, France. URL: `https://ntrs.nasa.gov/archive/nasa/casi.ntrs.nasa.gov/20170006953.pdf`.

[33] Ravi Gondhalekar, Colin N Jones, Thomas Besselmann, Jean-Hubert Hours, and Mehmet Mercangöz. Constrained spectrum control using MPC. pages 1219–1226, Orlando, FL, USA, December 2011.

[34] Tianyuan Guan. Special cases of the three body problem. URL: `https://inside.mines.edu/~tohno/teaching/PH505_2011/Paper_TianyuanGuan.pdf`.

[35] Narendra K Gupta. Frequency-shaped cost functionals – Extension of linear-quadratic-Gaussian design methods.

[36] John M. Hedgepeth. Efficient Structures for Geosyncrhonous-Spacecraft Solar Arrays. In *Lewis Research Center Space Photovoltaic Res. and Technol.*, Energy Production and Conversion, pages 363–377, Carpinteria, CA, United States, January 1980. Astro Research Corporation, Lewis Research Center. Document ID: 19810009051; Contract/Grant/Task Number: NAS7-100. URL: `https://ntrs.nasa.gov/archive/nasa/casi.ntrs.nasa.gov/19810009051.pdf`.

[37] Kelly Heidman. NASA Selects Studies for Gateway Power and Propulsion Element. November 2017. Release 17-024. URL: `{https://www.nasa.gov/press-release/nasa-selects-studies-for-gateway-power-and-propulsion-element}`.

[38] Jean-Hubert Hours, Melanie N Zeilinger, Ravi Gondhalekar, and Colin N Jones. Spectrogram-MPC: Enforcing hard constraints on systems' output spectra. pages 2010–2017, Montréal, Canada, June 2012.

[39] Jean-Hubert Hours, Melanie N Zeilinger, Ravi Gondhalekar, and Colin N Jones. Constrained Spectrum Control. 60(7):1969–1974, July 2015.

[40] The White House. Presidential Memorandum on Reinvigorating America's Human Space Exploration Program. *Infrastructure & Technology*, December 2017. Presidential Memoranda. URL: `https://www.whitehouse.gov/`.

[41] Jonathan P. How and Emilio Frazzoli. Topic #12: State-Space Systems. Web, 2010. Lecture Notes. URL: `https://ocw.mit.edu/courses/aeronautics-and-astronautics/16-30-feedback-control-systems-fall-2010/lecture-notes/MIT16_30F10_lec12.pdf`.

[42] John Guidi AES/HEOMD. Deep Space Gateway Study Overview. In *Global Exploration Roadmap Virtual Workshop*. National Aeronautics and Space Administration, November 2017. URL: `{https://sservi.nasa.gov/wp-content/uploads/ger-downloads/day1/Guidi-DSG-GER3-Workshop-20171130.pdf}`.

[43] Jeffrey L. Kauffman and George A. Lesieutre. Damping Models for Shear Beams with Applications to Spacecraft Wiring Harnesses.

[44] William S. Levine, Leonard Lublin, and Michael Athans. *Control System Advanced Methods: Linear Quadratic Regulator Control.* The Electrical Engineering Handbook Series. CRC Press: Taylor & Francis Group, LLC, 6000 Broken Sound Parkway NW, Suite 300; Boca Raton, FL 33487-2742, 2nd edition, 2011.

[45] Brandon Luders. 16.30/31, Fall 2010 - Recitation #7. Web, October 2010. URL: `https://ocw.mit.edu/courses/aeronautics-and-astronautics/16-30-feedback-control-systems-fall-2010/recitations/MIT16_30F10_rec07.pdf`.

[46] Michael Martin. 6 April 2018 and 21 May 2019: Interview with Michael Martin over Pulse Train Optimization Process for Shuttle.

[47] Michael Martin. Direct Deadband Collapse for Handover to ISS Control. Unpublished Charles Stark Draper Laboratory, Inc. Report, September 2009.

[48] Michael Martin. Variable Delays in the On-Orbit DAP for Loads Reductions. Technical report, The Charles Stark Draper Laboratory, Inc., 17629 El Camino Real, Suite 470 Houston, Tx 77058, May 2012. Unpublished Memorandum.

[49] MathWorks. Choose Sample Time and Horizons. Web. URL: `https://www.mathworks.com/help/mpc/ug/choosing-sample-time-and-horizons.html`.

[50] MathWorks. dlqr. Web, 2019. URL: `https://www.mathworks.com/help/control/ref/dlqr.html`.

[51] Melissa McGuire, Vicki Crable, Kurt Hack, and David Irmies. Power & Propulsion Element (PPE) Spacecraft Reference Trajectory Document. Technical Report PPE-DOC-0079, Rev B, John H. Glenn Research Center; National Aeronautics and Space Administration, Power and Propulsion Element (PPE); John H. Glenn Research Center; Cage Code No.: 1QFP5; 21000 Brookpark Road, Cleveland, Ohio 44135, May 2018.

[52] Navid Mohsenizadeh. Simulation Methodologies for Satellite Solar Array Dynamics. Master of science in mechanical engineering, Texas A & M University, August 2010. URL: `https://oaktrust.library.tamu.edu/bitstream/handle/1969.1/153192/Mohsenizadeh.pdf?sequence=1&isAllowed=y`.

[53] title = National Aeronautics and Space Administration. Technical report.

[54] R Nave. Simple Harmonic Motion Frequency. URL: `http://hyperphysics.phy-astr.gsu.edu/hbase/shm2.html`.

[55] L-3 Space & Navigation. CMG - Control Moment Gyro. *Double-Gimbal CMG*, September 2013. URL: `https://www2.l3t.com/spacenav/pdf/datasheets/CMG.pdf`.

[56] Karen Northon. NASA Acting Administrator Statement on Fiscal Year 2019 Budget Proposal. *National Aeronautics and Space Administration*, February 2018. URL: `{https://www.nasa.gov/press-release/nasa-acting-administrator-statement-on-fiscal-year-2019-budget-proposal}`.

[57] Mitsushige Oda, Akihiko Honda, Satoshi Suzuki, and Yusuke Hagiwara. Vibration of Satellite Solar Array Paddle Caused by Thermal Shock When a Satellite Goes Through the Eclipse. In Francisco Beltran-Carbajal, editor, *Advances in Vibration Engineering and Structural Dynamics*, chapter 13. IntechOpen, Rijeka, 2012. 10.5772/52626. URL: `https://doi.org/10.5772/52626`.

[58] CHC/Contracting Officer. Notice on Broad Agency Announcement (BAA) 80GRC018R0005 for the Spaceflight Demonstration of a Power & Propulsion Element (PPE). *National Aeronautics & Space Administration*, February 2019. John H. Glenn Research Center; Lewis Field; Cleveland, OH 44135-3191. URL: `{https://www.fbo.gov/index?s=opportunity&mode=form&id=4781210cbae339981c6725ca248a34aa&tab=core&_cview=1}`.

[59] Richard Pappa, Geoff Rose, Matthew K. Chamberlain, Dave Paddock, and Martin Mikulas. Compact Telescoping Surface Array for Mars Solar Power. 01 2018. DOI: 10.2514/6.2018-1944.

[60] Richard Pappa, Geoff Rose, Troy Mann, Jerry Warren, Martin Mikulas, Tom Kerslake, Tom Kraft, and Jeremy Banik, editors. *Solar Array Structures for 300 kW-Class Spacecraft*, number 20140000360, NASA Langley Research Center; Hampton, VA, United States, April 2013. Space Power Workshop, National Aeronautics and Space Administration. Contract/Grant/Task Number: WBS 269655.04.01.01.07. URL: `{https://ntrs.nasa.gov/search.jsp?R=20140000360}`.

[61] Andre Preumont. *Vibration Control of Active Structures, An Introduction*. Solid Mechanics and Its Application. Springer, 3rd edition, January 2011. DOI: 10.1007/978-94-007-2033-6; ISBN: 9789400720329; 9789400720336 (online. URL: `http://scmero.ulb.ac.be/Teaching/Courses/MECA-H-524/MECA-H-524-Lectures.pdf;http://www.bookmetrix.com/detail/book/7a7e41bc-f0c6-4e07-bd0b-725a9a64bb84#citations`.

[62] Derek Rowell. 2.14 Analysis and Design of Feedback Control Systems; State-Space. Web, October 2002. URL: `{http://web.mit.edu/2.14/www/Handouts/StateSpace.pdf}`.

[63] Lester L. Sackett. Space Shuttle On-orbit Flight Control System Development and Analysis at the Draper Laboratory. Unpublished Charles Stark Draper Laboratory, Inc. Report, 2002.

[64] Dr. Yeu-Sheng Paul Shiue. Torsional Vibrations. *ME 318: Dynamics of Machines Lecture Notes*, 2001. URL: `http://facstaff.cbu.edu/~pshiue/Courses/ME318/Notes/Lecture17.pdf`.

[65] Davin Swanson and Neil Dennehy. GN&C Tutorial Lecture: An Introduction to the Fundamentals of Control-Structure Interaction. NASA Engineering and Safety Center (NESC) Academy, March 2017. URL:

`https://nescacademy.nasa.gov/review/downloadfile.php?file=CSItutorial_Webcast_FINAL.pptx&id=780&distr=Public`.

[66] S. R. Vadali T. Singh. Robust Time-Optimal Control: Frequency Domain Approach.

[67] Carlyle Webb. Multilateral Coordination Board Joint Statement. *National Aeronautics and Space Administration*, March 2019. URL: `{https://www.nasa.gov/feature/multilateral-coordination-board-joint-statement}`.

[68] Ryan Whitley and Roland Martinez. Options for Staging Orbits in Cis-Lunar Space. In *37th IEEE Annual Aerospace Conference*, pages 1–9, Big Sky, MT; United States, October 2015. NASA Johnson Space Center; Houston, TX, United States. Report/Patent Number: JSC-CN-34623; Document ID: 20150019648. URL: `https://ntrs.nasa.gov/archive/nasa/casi.ntrs.nasa.gov/20150019648.pdf`.

[69] William Widnall. 16.895/STS.471: Engineering Apollo: The Moon Project as a Complex System: Apollo Software Lecture on 21 March 2019.

[70] Arun K. Banerjee William E. Singhose and Warren P. Seering. Slewing Flexible Spacecraft with Deflection-Limiting Input Shaping.

[71] Jacob Williams, David Lee, Ryan Whitley, Kevin Bokelmann, Diane Davis, and Christopher Berry. Targeting Cislunar Near Rectilinear Halo Orbits For Human Space Exploration. In *27th AAS/AIAA Space Flight Mechanics Meeting*, pages 1–20, San Antonio, TX; United States, February 2017. American Astronomical Society and American Inst. of Aeronautics and Astronautics, National Aeronautics and Space Administration. Report/Patent Number: JSC-CN-38615. URL: `https://ntrs.nasa.gov/search.jsp?R=20170001352`.

[72] Douglas Zimpfer, Phil Hattis, John Ruppert, and Don Gavert. Space Shuttle GN&C Development History and Evolution. In *AIAA SPACE 2011 Conference & Exposition*, AIAA 2011-7244, Long Beach, CA, USA, September 2011.

[73] Douglas J. Zimpfer. STS-71 Shuttle/Mir Mission Report. *NASA-CR-188442 STS-71*, (N96-15204), July 1995. G3/16 0081139. URL: `{https://archive.org/details/nasa_techdoc_19960008038}`.

[74] K. J. Åström and R. M. Murray. Analysis and Design of Feedback Systems. Unpublished Draft: 2004 Preprint, 2004. URL: `https://www.cds.caltech.edu/~murray/courses/cds101/fa04/caltech/am04_ch8-3nov04.pdf;https://www.cds.caltech.edu/~murray/courses/cds101/fa04/reading.html`.

[75] Karl J. Åström and Tore Hägglund. *Control System Fundamentals: PID Control.* The Electrical Engineering Handbook Series. CRC Press: Taylor & Francis Group, LLC, 6000 Broken Sound Parkway NW, Suite 300; Boca Raton, FL 33487-2742, 2nd edition, 2011. ISBN: 978-1-4200-7362-1.